

# The quest for primary Devonian magnetism in the Pyrenees and the implications for the Paleozoic paleogeographical position of Iberia

Master thesis by O.W. Groenhof, Utrecht University

Supervisors:

1. Daniel Pastor Gálan, Utrecht University, paleomagnetic laboratory Fort Hoofddijk
2. Mark Dekkers, Utrecht University, paleomagnetic laboratory Fort Hoofddijk

## abstract

The paleogeography of Iberia during the Devonian is still under debate. Paleomagnetic data suggests an episode of rifting between Iberia and the rest of Gondwana during the Middle Paleozoic whereas results from paleontology, geochronology and geochemistry argue that such a departure is unlikely. To shed more light on this intricate matter extensive paleomagnetic fieldwork has been undertaken in the Pyrenees, sampling 18 Devonian limestones and 1 Permian granite. Stepwise demagnetization and end-member modeling indicate magnetite and pyrrhotite as responsible for the magnetization. The abundance of pyrrhotite and several negative fold tests reflect on the magnetism's secondary character. Of these 19 sites, 7 record the counterclockwise rotation of Iberia during the Cretaceous with a combined direction of  $326.9^\circ/38.1^\circ$ ,  $k=7.7$  and  $a_{95}=5.5^\circ$ . The other sites either have scattered directions or lack consistency; trying to link those to known vertical axis rotations in the Pyrenees have proven unsuccessful. The directions recorded in the granite ( $217.8^\circ/40.5^\circ$ ,  $k=24.7$  and  $a_{95}=11.4^\circ$ ) are somewhat similar to a component found in another study (**Tait & Bachtadse, 2000**) ( $224^\circ/51^\circ$ ,  $k=24.5$  and  $a_{95}=8.5^\circ$ ) that is used to justify the separation of Iberia and the rest of Gondwana during the Devonian. It is likely that both these directions are the result of a remagnetization event with an as of yet unknown timing since it is impossible to record a Devonian direction in rocks from the Permian. Combining these results with the counterarguments provided by other fields of geology and the scenario in which Iberia drifted away from Gondwana during the Paleozoic is no longer supported.

# table of contents

- 1. introduction - 3**
- 2. Phanerozoic history of northeastern Iberia - 5**
- 3. methods - 7**
  - 3.1 sampling strategy - 7
  - 3.2 obtaining magnetic remanence - 9
  - 3.3 thermomagnetic runs - 10
  - 3.4 anisotropy of magnetic susceptibility - 11
  - 3.5 hysteresis loops - 12
  - 3.6 isothermal remanent magnetization and end-member modeling - 12
- 4. results and data interpretations - 13**
  - 4.1 demagnetization - 13
  - 4.2 Curie balance - 23
  - 4.3 anisotropy of magnetic susceptibility - 24
  - 4.4 hysteresis loops - 25
  - 4.5 isothermal remanent magnetization and end-member modeling - 27
- 5. discussion - 32**
  - 5.1 real or 'fabricated' results - 32
  - 5.2 vertical axis rotations - 33
  - 5.3 Cretaceous overprint? - 35
- 6. conclusion - 40**
- 7. references - 40**
- 8. appendices - 45**
  - 8.1 Zijderveld diagrams - 45
  - 8.2 Curie balance plots - 55
  - 8.3 hysteresis loops - 58
  - 8.4 anisotropy of magnetic susceptibility - 64
  - 8.5 IRM - 73
  - 8.6 miscellaneous - 77

# 1. introduction

The paleogeographic position of Iberia and other Armorican terranes (modern-day Brittany) during the Paleozoic and their relation with Gondwana and the Rheic and Paleotethian Oceans is still unresolved. Constraints on the paleogeography and tectonic setting of these Armorican outcrops are critical for furthering our knowledge on the amalgamation of Pangea, the Variscan orogeny and the assemblages of microcontinents in combination with conjugate margins in general. The debate centers around the question whether Iberia, either as part of Armorica or as a separate microcontinent (**figure 1**), drifted away from Gondwana (**Tait, 1999; Stampfli & Borel, 2002; Torsvik & Cocks, 2011**) or remained part of the northern passive Gondwanan margin instead (**Robardet, 2003; Linnemann et al., 2004; Díez-Fernández et al., 2010; Pastor-Galán, 2013**). In the former scenario Iberia is considered part of the Galatian superterrane (Galatia) (**Stampfli et al., 2013**), an amalgamation of terranes that detached and drifted away in stages from Gondwana in the Middle Paleozoic and accreted to Laurasia in Carboniferous times (**Torsvik et al., 2012; Pastor-Galán et al., 2013**). The detachment of Galatia with Gondwana opened up the Paleotethys ocean and the collision with Laurasia is responsible for the closure of the Rheic Ocean and the genesis of the Variscan orogeny (**Stampfli et al., 2013**).

The argument for the separation of Armorica from Gondwana stems from the field of paleomagnetism. Paleomagnetic data from Bohemia in the Late Silurian (**Tait et al., 1994**) and from Armorican France in the Early Devonian (**Tait, 1999**) give paleolatitudes of 23°S and 19°S, respectively, placing the aforementioned localities in contact with the southern border of Avalonia and Baltica. Similar results have been found in the Pyrenees from Late Silurian/Early Devonian sediments (**Tait & Bachtadse., 2000**), indicating paleolatitudes of 30°S for the Pyrenees similar to the rest of Galatia. These data indicate that the corresponding part of the Rheic Ocean must have been closed by Early Devonian times (**Tait, 1999; Robardet, 2002; Torsvik & Cocks, 2011**), and in similar vein, that the Paleotethys ocean must have opened in the Late Silurian. It is worth mentioning that Iberia was included in the definition of Armorica (**Torsvik & Cocks, 2002; 2004**), but revised paleolatitudes and new age constraints have since made it into a separate microcontinent (**Robardet, 2003; Torsvik et al., 2012; Stampfli et al., 2013**). Based on the aforementioned data gathered by **Tait et al.**, and the plate tectonic model of **Stampfli & Borel (2002)** **Torsvik & Cocks** have consistently regarded Armorica and Iberia as an entity separate from Gondwana in their paleogeographical maps from the Paleozoic (**Torsvik & Cocks, 2002; 2004; 2011, Torsvik et al., 2012**), but the extent of departure is not well constrained (**Torsvik & Cocks, 2011**). In the plate tectonic reconstruction by **Stampfli et al. (2011; 2013)** Galatia (and thus Iberia) separated from Gondwana between 400 and 380 Ma (**Stampfli et al., 2011**) based on crustal extension during the Silurian and the associated syn-rift volcanism found in terranes thought to belong to Galatia. (**Schönlaub, 1997; von Raumer & Stampfli, 2008**). Galatia subsequently accreted to Laurasia in the Early Carboniferous (**Stampfli et al., 2011**).

**400 Ma (GAD)  
Early Devonian**

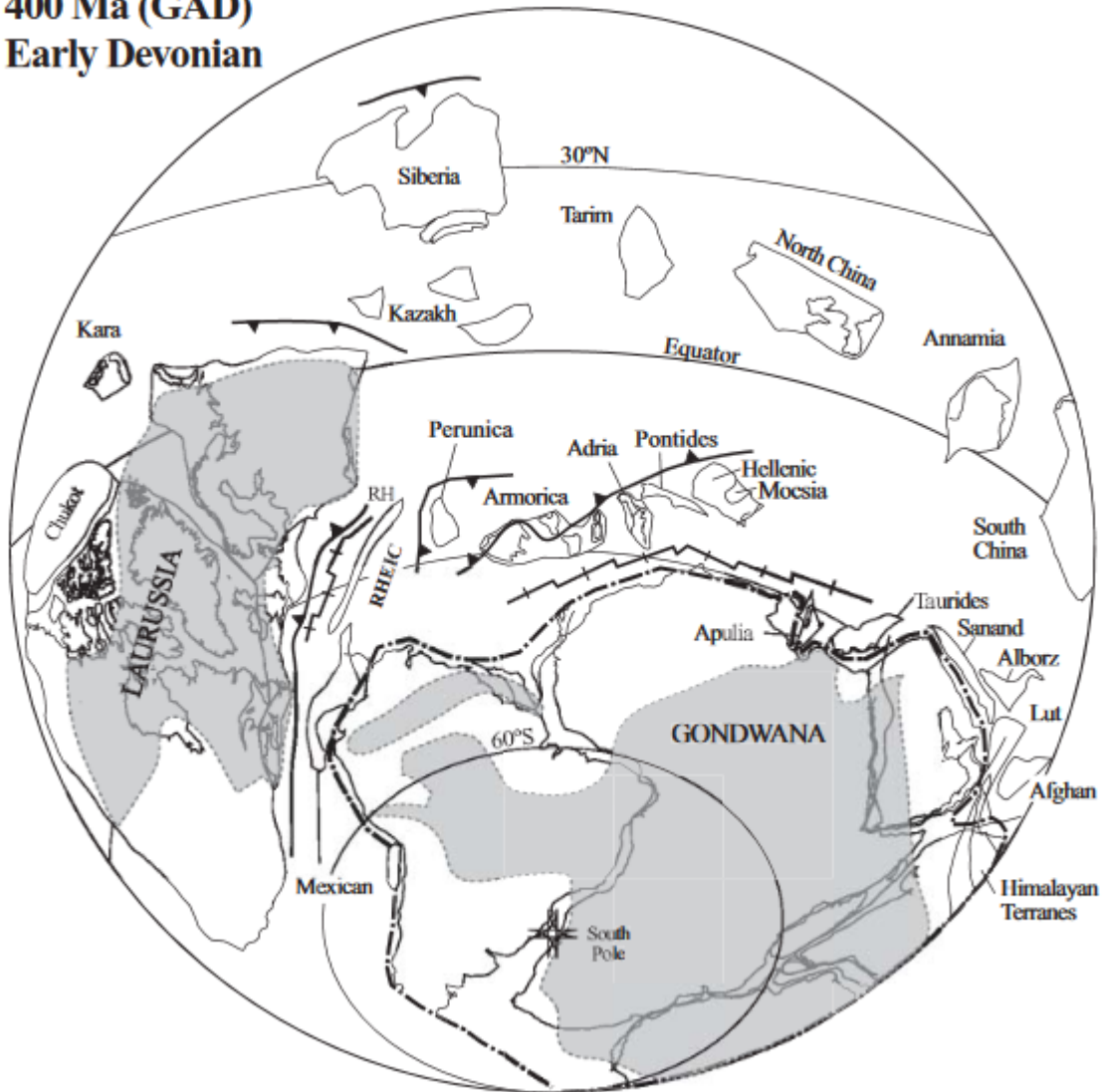


figure 1. View of the Gondwanan landmass and the Galatian terranes in the Early Devonian according to Torsvik & Cocks, 2004. This is in support of the drifting Armorica hypothesis. After Torsvik & Cocks, 2004.

However, some authors consider the paleomagnetic data in support of the detachment of Armorica to be too scarce and not robust enough. **Robardet, 2003** argues that the available paleomagnetic data from the Silurian and Devonian do not allow for the vast conclusion of an Armorican microplate. The age of the sampled rocks is poorly constrained, making the available paleomagnetic directions not only too scarce but also too ambiguous (**Robardet, 2003**). Furthermore, the paleomagnetic directions thought to be Silurian/Devonian in origin (**Tait & Bachtadse, 2000**) actually being a Cretaceous overprint is another possibility (**Robardet, 2003**). Paleoclimatological and paleobiographical data based on fossil occurrences of land plants and both vertebrates and invertebrates in the Early Devonian, on the other hand, indicate that is not possible for an ocean to have separated Armorica and Gondwana during any time in the Early Devonian (**Young, 1987; Robardet et al., 1990; Robardet, 2003**). The flora and fauna of the Armorican terranes is in good accordance with those of Gondwana (**Morzadec et al., 1988**) and bears only superficial similarities to the biosphere of Baltica and Avalonia (**Young, 1990**). These data and the resultant conclusion have been ignored in both the works of **Stampfli et al. (2011; 2013, and Torsvik & Cocks (2011) (Robardet et al., 2003)**. In addition to criticism from the field of paleontology data from geochronology (**Linnemann et al.,**

**2004; Díez-Fernández et al., 2010)** and geochemistry (**Pastor-Galán et al., 2013**) do not support the Armorican microplate hypothesis either. SHRIMP U/Pb geochronology performed on zircons from pre-Variscan rocks from the Bohemian Massif show a clear West-African affinity for this region whereas Sm-Nd isotopic data from sedimentary rocks ranging in age from the Neoproterozoic to the Lower Carboniferous for the same region give no change in the origin of the sediments throughout the aforementioned timeline, indicating Gondwanan affinity throughout the middle Paleozoic (**Linnemann et al., 2004**). Similar results have been obtained for Iberia, with whole rock geochemistry, X-ray diffraction and Sm-Nd isotopes from sedimentary strata from the Cantabrian zone indicating that Iberia was an active margin during the Ediacarian and became a passive margin from the Ordovician onwards until the Variscan orogeny in the Carboniferous. (**Pastor-Galán et al., 2013**)

The aim of this master thesis was to gain better insights into the paleoposition of Iberia during the middle Paleozoic. To this extent paleomagnetic fieldwork drilling Devonian rocks has been undertaken in the Pyrenees, hoping that the newly gathered data will strengthen the paleomagnetic foothold in this debate and add to the Devonian database. Alternatively, the new data might reflect on the paucity of Devonian paleomagnetic data in general, showing that the current paleomagnetic data from the Pyrenees regarding Armorica in the Devonian is too ambiguous and thus flawed and cannot be used to draw paleotectonic and paleogeographical conclusions from. In hindsight it has proven difficult to disentangle the several directions obtained from the Pyrenees. The Variscan and Alpine orogenies, as well as the likely several syn- or post-orogenic remagnetization events that occurred on a local scale during the Mesozoic and Cenozoic demand more extensive research than has been done and as such this thesis will also highlight difficulty of deriving paleomagnetic directions from multiphase orogenic systems.

## 2. Phanerozoic history of northeastern Iberia

The formation of Gondwana came to fruition when several island arcs accreted to its northern margin in the Late Neoproterozoic and Early Cambrian (**Stamfli & Borel, 2002; Murphy et al., 2006; Linnemann et al., 2007; Pereira et al., 2012; Stampfli et al., 2013; Stampfli et al., 2013**), but the extent, age and exact circumstances are still debated (**Stampfli et al., 2013**). This period of accretion is known as the Cadomian event (**Stampfli et al., 2011**) and led to widespread magmatism along Gondwana's northern margin. In Late Cambrian/Early Ordovician the first wave of peri-Gondwanan terranes left Gondwana, leading first to the birth of the western Rheic Ocean with the departure of Avalonia and Carolina and subsequently of the eastern branch with the rifting of Hunia (**Torsvik & Cocks, 2002; Murphy et al., 2006; Stampfli et al., 2011; Pastor-Galán et al., 2013**). These terranes, sans Hunia, can be collectively termed the Avalonia assemblage and comprises the basement of modern-day northwestern Europe and the eastern coast of North America. The name Hunia is reserved for Gondwanian-derived accreted parts to the northern China block (**von Raumer & Stampfli, 2008**). The mechanisms responsible for this episode of rifting are still under debate. Ridge subduction underneath Laurentia and the resultant slab pull might have caused the Cadomian terranes to detach from Gondwana and the eventual opening of the Rheic Ocean (**Murphy et al., 2006**). Alternatively, subduction roll-back might be the reason for rift initiation (**Martínez Catalán et al., 2009; Díez-Fernández et al., 2012**). The abundance of rift-related magmatic rocks in northwest Iberia with ages ranging between 495 and 470 Ma are a testimony to the aforementioned period of rifting (**Bae et al., 2006; Gutiérrez-Alonso et al., 2007; Murphy et**

al., 2008), as well as the build-up of thick sedimentary strata related to passive margins (Pastor-Galán et al., 2013). Avalonia and Hunia accreted to Laurussia and China, respectively, during the Silurian (Stampfli et al., 2011), during which the Rheic Ocean is thought to have reached its largest span (Nance et al., 2010).

Late Silurian saw Galatia leaving Gondwana (Torsvik & Cocks et al., 2002; Stampfli et al., 2013). Iberia is included on the basis of paleomagnetic data (Tait et al., 2000). Debate regarding the second wave of terranes leaving Gondwana is far from settled, however, with some authors doubting Iberia's inclusion (Linnemann et al., 2004; Díez-Fernández et al., 2010 Pastor-Galán et al., 2013), or the existence of Galatia altogether (Robardet, 2003) as it does not fit available paleontological, geochemical and geochronological data. In the former scenario the drift of Galatia opened up the Paleotethys and its eventual collision with Laurentia closed the Rheic Ocean and started the Variscan orogeny (Pastor-Galán et al., 2013). There is still uncertainty regarding the direction of subduction, with most models considering subduction of the Rheic Ocean towards both Gondwana and Laurussia (Stampfli & Borel, 2002), or, alternatively towards both Armorican margins. In the latter scenario Iberia remains part of Gondwana's passive margin during the Paleozoic, with northwards subduction of the Rheic Ocean. Regardless of the actual scenario, the collision of Gondwana with Laurussia began at around 365 Ma (Dallmeyer et al., 1997; Stampfli et al., 2011) and is recorded in ophiolites in suture zones (Arenas et al., 2007).

The orogeny lasted for about 80 million years, with the Rheic and Paleotethian oceans suturing at 300 Ma (Nance et al., 2010). This continued accretion led to extensive crustal thickening with subsequent collapse of the hinterland in several parts of the Variscan belt. This collapse resulted in widespread post-orogenic extension and crustal thinning (Gretter et al., 2015). Due to severe thermal weakening of the lower crust the Late Carboniferous and Early Permian basins were dominated by dextral strike-slip regimes (Rey et al., 2001; Decarlis et al., 2013; Druguet et al., 2014). Activation of normal and transtensional faults in Mid-Permian times signal a shift into a more extensional regime culminating with the opening of the Neotethys in the Late Permian and the breakup of Pangaea in the Triassic (Stampfli & Borel, 2002; Gretter et al., 2015). The Central and South Atlantic opened in the Early Jurassic and the Cretaceous, respectively. Iberia remained part of Laurasia until the Cretaceous (Vissers & Meijer, 2012).

Kinematic models reconstructed for the Late Jurassic/Early Cretaceous show that more than 200 km of left-lateral strike-slip motion must have been accommodated by the Iberian – European plate boundary (IEPB) (Rosenbaum et al., 2002; Jammes et al., 2010), though the exact extent and location is still up for debate (Tugend et al., 2015). A major reconfiguration of plate kinematics caused by sea-floor spreading in the Bay of Biscay (BoB) during the Cretaceous Normal Superchron is similarly responsible for a sinistral strike-slip setting in the Pyrenees. (Rosenbaum et al., 2002). The Aptian saw a shift from left-lateral motion between Iberia and Europe to a more north-south oriented divergence (Tugend et al., 2015). Similarly, the motion of Africa relative to Europe and Iberia initially represents left-lateral strike-slip movement but during the Santonian/Campanian it transforms into a convergent setting (Rosenbaumer et al., 2002; Tugend et al., 2015). Geological evidence, such as the offset in the North Pyrenean Fault, is in good accordance with these plate-motion reconstructions (Soula et al., 1986; de Jong, 1990; Rosenbaum et al., 2002). Paleomagnetic directions for Iberia in the Cretaceous are clear-cut, though inconsistencies regarding the age, available data and possible remagnetizations are present. The data shows a counter-clockwise rotation recorded in

inverted Cretaceous basins during the Aptian of about 35° for Iberia away from Europe as a response to the opening of the BoB as well as the opening of the Atlantic Ocean (**Van der Voo, 1969; Sibuet et al., 2004; Gong et al., 2008; 2009a**).

The collision between the Iberian and Eurasian plates started in the Late Cretaceous and continued until Miocene times (**Sinclair et al., 2005; Rushlow et al., 2013; Izquierdo-Llavall et al., 2015**). This double-vergent orogeny resulted in the formation of the Pyrenees (**Martínez-Peña & Casas-Sainz, 2013**), with most of the shortening accommodated by the reactivation of earlier faults (**Vergés et al., 2002**). The Pyrenees consist of several east-west trending structural entities that each experienced different regional tectonics regarding thrusting and as a result vertical axis rotations (VARs) in the Cenozoic will vary depending on the location (**Izquierdo-Llavall et al., 2015**).

### 3. methods

In this section the acquisition of the samples and the various techniques of analyzing said samples will be described.

#### sampling strategy

A total of 19 sites were sampled, 15 in the Spanish Pyrenees and two in Andorra and France, respectively. A total of 203 cores were drilled in the Spanish and Andorran Pyrenees combined, with three block samples taken from both localities in France. The westernmost site is located just to the east of the village of Panticosa, the easternmost locality is just to the northeast of Andorra's capital (**figure 2a,b**). All but one of the sampled locations are taken from Devonian limestones/marly limestones; the first site samples granite instead. The addition of the intrusion allows the effect of a baked contact to be examined. In a similar vein several individual holes have been drilled into boudins or intruded dykes to study the aforementioned phenomenon. Folds have been observed at several drilling sites and as such provide material for multiple fold tests.

The samples were gathered using a portable gasoline-driven drill with a water-cooled diamond drill-bit. The cylindrical cores have standard dimensions of 10 cm<sup>3</sup> with a diameter of 2.5 cm and can be up to 10 cm in length (**Tauxe, 2005**). The upright position of the core (**figure 3**) is marked by a field arrow pointing towards the outcrop. Dip direction and dip of the drilled cores were subsequently oriented in the field by using a magnetic compass, the accuracy of such measurements amounts to 3°. Bedding and foliation measurements, where possible, were also performed. The reader is referred to the miscellaneous section of the appendix for an overview of the bedding and foliation measurements, as well as the GPS coordinates for the sites.

At the Fort Hoofddijk paleomagnetic laboratory in Utrecht the cores were cut to 2 cm in length, sometimes leading to multiple specimens per core. This procedure was done by placing the specimen between two rotating diamond cup wheels 2 cm apart. Water is added to cool the machine as well as to prevent remagnetization by friction.

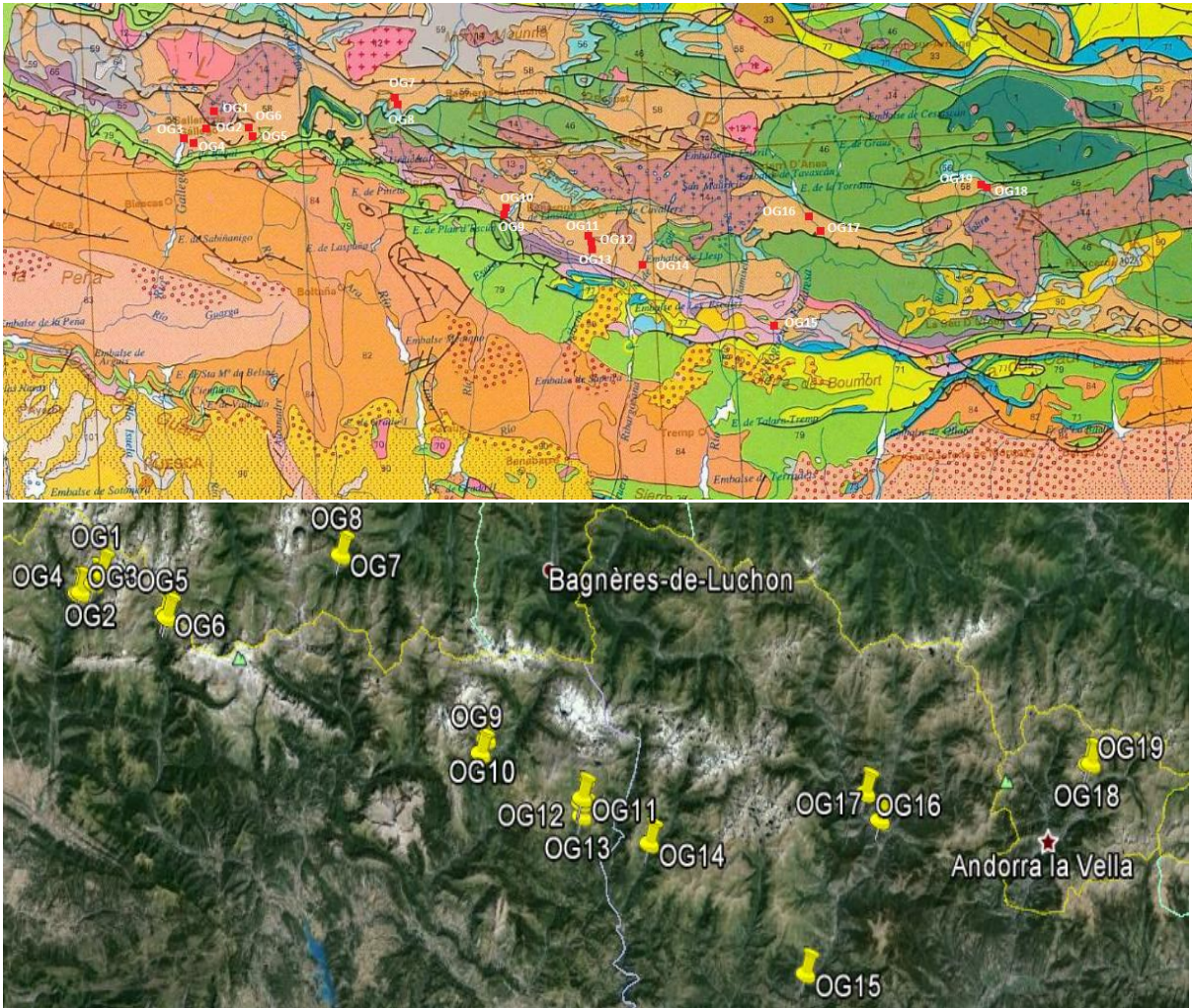


figure 2a: Geological map of the Central Pyrenees showing the sampled locations. Modified map from the Instituto Geológico y Minero de España. Scale 1:1,000,000. The light orange colour represents Devonian limestones. 2b: Google Earth map of the Central Pyrenees showing the sampled locations.

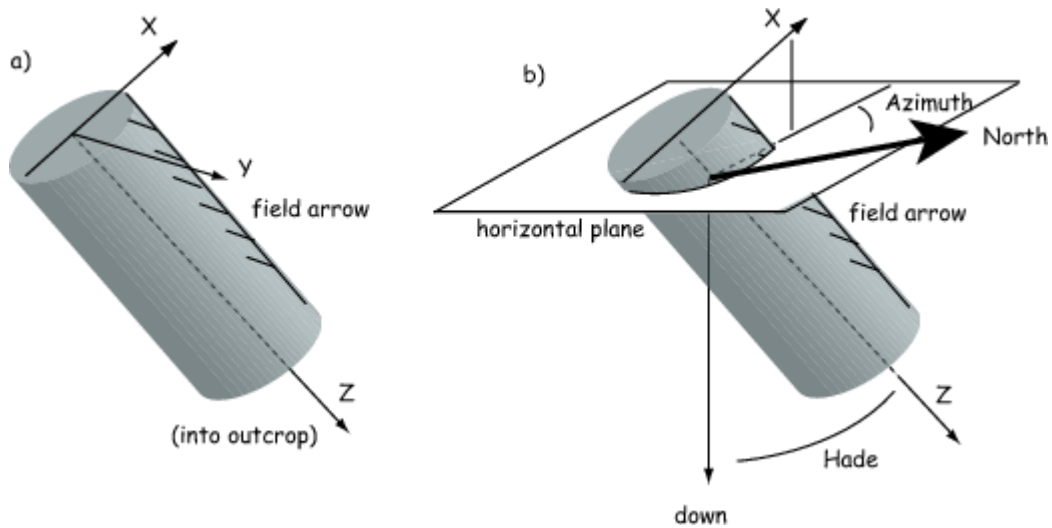


figure 3. Figure showing the orientation of the drilled cores. 3a: The field arrows, aligning with the z-axis, indicate the direction into the outcrop. The x-axis and y-axis are the vertical and horizontal plane, respectively. 3b: Showing the hade and azimuth of a collected core. After *Tauxe, 2005*



### 3.1 obtaining magnetic remanence

Both thermal and alternating field demagnetization involve the measurement of natural remanent magnetization (NRM), the residual magnetism that rocks garnered over the course of millions of years, possibly in the form of multiple components. The objective of paleomagnetism is to unravel this stored information and isolate the different component to try and gain insight into age, paleoposition and chemical make-up of said rocks.

Thermal demagnetization at Fort Hoofddijk is done with a 2G Enterprises cryogenic superconducting quantum interference device (SQUID) magnetometer. The procedure entails heating of the samples in a field-free furnace followed by subsequent cooling to room temperature. For each temperature step the NRM is measured for both the arrow-in and arrow-out position and averaged as to reduce errors. Starting values for the NRM can be as high as  $4.0 \times 10^{-1} \text{ Am}^{-1}$  and as low as  $400 \text{ uAm}^{-1}$ . This conduct is repeated in a step-wise manner till the sample is fully demagnetized or starts behaving irregularly. This behavior includes nonsensical directions or elevated magnetic intensities from 400 °C onwards indicating either the formation of new minerals or mere randomness. The samples in this research either contain pyrrhotite or magnetite as the carriers of the magnetic signal, and both minerals require different temperature steps. The samples containing magnetite have been heated to temperatures of 580 °C following the standard demagnetization temperature steps of 30-55 °C. For the samples containing pyrrhotite temperature steps of 10/15 °C have been incorporated between 275 °C and 330 °C, after which the cores are essentially devoid of a magnetic signal (**table 1**).

	temperature steps thermal demagnetization (°C)																
magnetite	20	100	150	180	210	240	270	300	330	370	420	480	510	540	560	570	580
magnetite	20	100	150	200	250	300	350	400	450	500	520	540	560	580			
pyrrhotite	20	100	150	180	220	250	265	275	285	295	305	315	330				

**table 1:** A table detailing the different temperature steps for the minerals magnetite and pyrrhotite.

The temperature steps for magnetite are up to the demagnetizer's discretion. If the demagnetization of magnetite takes place at elevated temperatures the second temperature path is preferred to speed up the process.

Once the temperature approaches the Curie temperature of the ferromagnetic minerals thought to be present in the sample a sharp decline in magnetic intensity is observed. The unblocking temperature is reached when the relaxation time is in equilibrium with the field. When cooled to room temperature a magnetic field with a magnitude of zero is applied (**Tauxe, 2005**).

Alternating field (AF) treatment is done with a built-in robot equipped with alternating field coils and a 2G Enterprises cryogenic SQUID magnetometer (**Mullender et al., 2005**). The samples are tightly glued into silicone cubes and emplaced in the machine in rows of eight. They are measured a total of 15 times at increasing field intensities (**table 2**) and to ensure demagnetization along all three orthogonal axes the samples are rotated during the process. AF makes use of the fact that different grains in the sample have different coercivities. An oscillating field is applied to the samples inside the robot at increasing magnitudes at each step. If the coercivity of the grains is lower than the externally applied field the magnetic moment is recorded. The variety of coercivities in the specimen results in some of the grains to be stuck in one direction and other grains in the opposite direction, resulting in a remanence of zero (**Tauxe, 2005**). Prior to placement in the robot the samples were pre-heated in the oven up to 150 °C to eliminate stress caused by surface oxidation in magnetite grains at lower

temperatures (**Van Velzen & Zijdeveld, 1995**). The alternating field treatment does not work properly on specimens containing pyrrhotite and so only samples containing magnetite have been demagnetized with AF.

#	1	2	3	4	5	6	7	8	9	10	11	12	13	14	15
field (mT)	0	5	10	15	20	25	30	35	40	50	60	70	80	90	100

**table 2: The steps applied to alternating field demagnetization.**

Both practices involve the portrayal of the resultant characteristic remanent magnetization (ChRM) (**Koymans et al., 2016**). The ChRM will be the most stable component; ideally the vector will show a straight line towards the origin. For both thermal and alternating field demagnetization the results are interpreted with the help of Zijdeveld diagrams (**Zijdeveld, 1967**) using principal component analysis (**Kirschvink, 1980**). The Zijdeveld diagram is a two-dimensional projection which projects the inclination onto the vertical plane through the north-south axis or the east-west axis. The declination is shown on the horizontal plane. For the results of the ChRM to be scientifically valid several criteria are evaluated. The maximum angle of deviation (MAD) must not exceed 15 degrees and a series of at least 5 consecutive data points is necessary for a component to be regarded as such. A grouping of 7 cores or more needs to arise for a component to be statistically significant.

### 3.2 thermomagnetic runs

The Curie balance supplements the data provided by demagnetization regarding the identification of magnetic minerals. There is a house-built horizontal translational Curie balance at Fort Hoofddijk (**Mullender et al., 1993**). The machine works by applying an induced sinusoidally cycled magnetic field over a series of temperature increments and measuring the current needed to keep the beam in its original position. The change in magnetization causes a slight horizontal displacement (several picometers). This displacement is measured with a seismometer and is automatically compensated by an automatic force compensator that uses an electric current to negate the displacement. The current necessary to return the sample to its original position is indicative of the minerals present. Samples are heated up to 720 °C, starting from room temperature with small increments of about 10 °C/minute (**table 3**). Once temperatures present in table 3 are reached the machine cools the samples before embarking on its next temperature step. The applied field has a magnitude of 100 mT up to 300 mT.

#	1	2	3	4	5	6	7	8	9	10	11	12
temp (°C)	20	200	250	300	350	400	450	500	550	600	650	720

**table 3: The temperature at which a cooling interval is applied for the Curie balance.**

Prior to placement in the Curie balance the samples are crushed to a powder and weighted. The ideal weight of the sample is somewhere between 50 and 100 mg. The crushed powder is placed inside a test tube, covered on both sides with thermally conductive quartz wool and subsequently put inside the apparatus.

The resultant graph plots the magnetic moment against the temperature. Comparing the shape of the curves in the graph with other graphs in which the magnetic carrier is known allows the mineral responsible for the magnetism present to be distinguished.

### 3.3 anisotropy of magnetic susceptibility

Performing analysis on the anisotropy of magnetic susceptibility (AMS) can provide clues on the preferred orientation of the magnetic minerals **(Tauxe, 2005)**. The anisotropy of magnetic susceptibility can be described as the relationship between an applied magnetic field and the resultant magnetization vector. If a magnetic field gets applied to a rock sample the intensity of magnetization is likely to differ between directions dependent on the orientation of the magnetic minerals present in the sample. This allows for the examination of the tectonic fabric of the rock. This in turn can lead to knowledge on the kinematic history of the rock and the possible tectono-metamorphic processes that the rock had to endure **(Dubey, 2014)**.

The anisotropy of magnetic susceptibility is measured on an AGICO MFK-1 Kappabridge. The machine has a field range between  $2 \text{ Am}^{-1}$  to  $700 \text{ Am}^{-1}$  and measures the samples in three different orthogonal positions; these positions represent the principal axes of the susceptibility ellipsoid. For this research a field of  $200 \text{ Am}^{-1}$  was used. The samples must be manually switched between positions while keeping the applied magnetic field stable to calculate the susceptibility tensor. The resultant susceptibility ellipsoid is depicted in a Flinn, Ramsay or Jelinek diagram in the program Anisoft 4.2. All these plots use different variables along the x- and y-axes but they all show the oblateness or prolateness of the respective site. This ellipsoid has three principal susceptibility axes, with K1, K2 and K3 being the maximum, intermediate and minimum, respectively. The lineation (L) is defined as  $K1/K2$  and the foliation (F) can be expressed as  $K2/K3$  **(Dubey, 2014)**. The degree of anisotropy can be calculated as  $K1/K3$ . Generally, the lineation is parallel to the extension direction whereas the orientation of K3 is perpendicular to the extension direction **(Sagnotti et al., 1994; Dubey, 2014)**.

The fabric in the samples can influence the magnetic directions garnered in the demagnetization process and render them devoid of meaning. If the magnetic direction is located on the plane between K1 and K2 the reliability of the directional data should be called into question.

### 3.4 hysteresis loops

The purpose of hysteresis loops is to increase understanding of the magnetic domain of the sample as well as gain insight into grain sizes of the samples. Hysteresis loops are measured with a Micromag 2900 series alternating gradient magnetometer (AGM). The samples are crushed and reduced to several micrograms (30-50 mg) in mass before they are attached to a probe and emplaced between two magnets. Two small coils attached to the magnet control the strength of the applied alternating gradient field. Silicone is used to fixate the samples to the probe.

In the machine the samples are exposed to a magnetic field in one direction. When the strength of the applied field causes the magnetic field to flip into the direction of the applied field an irreversible change has occurred and the magnetic field will have an opposite direction when the externally applied field is taken away **(Tauxe, 2005)**. This flip happens when  $B > \mu_0 H_f$ . The procedure is then repeated in the opposite direction causing the magnetization to flip back to its original direction. The vibration caused by the change in field characteristics is tracked by the probe, with the amplitude being proportional to the moment in the respective field direction.

These samples are subjected to fields up to 2 Tesla. Since the loop often ceases to be linear after 1.6 T a pole-shoe correction is applied, assuming that the samples will have reached saturation

after 1.2 T. The results need to be corrected for paramagnetic behavior. This is done by converting the paramagnetic slope into horizontal positions. Values for coercive force ( $B_c$ ), saturation remanence ( $M_r$ ) and saturation magnetization ( $M_s$ ) can be read from the resultant graphs.

The results are depicted in a graph, with the applied field and magnetization (normalized) on the x- and y-axes, respectively. The loop's retrace is never perfect. i.e. there will be irregularities and as such the loop will not retrace its steps perfectly. The irregularities are a result of the existence of different magnetic domains. These magnetic domains can record the magnetization and as such can be used as magnetic memories. These magnetic domains are largely randomly orientated without the addition of an external magnetic field but will align themselves when said field is applied.

### 3.5 isothermal remanent magnetization and end-member modeling

Isothermal remanent magnetization (IRM) entails applying an external magnetic field to the samples while keeping the temperature constant. This process gains insight into how the magnetic minerals acquire their magnetization. The magnetic structure in the magnetic minerals will try to line up with the applied direction as much as possible and acquire the remanence. The IRM-technique and the subsequent end-member modeling is especially useful for distinguishing between primary and secondary magnetization (**Gong et al., 2009b; Dekkers, 2012**), though in regards to this thesis its purpose is primarily to provide supplementary info regarding the directional data garnered from demagnetization.

88 samples were given the IRM-treatment. Prior to placement in the SQUID-magnetometer for acquiring the IRM-acquisition curves the samples are demagnetized using alternating fields up to 300 mT for three different positions (perpendicular axes). This is done to reduce to effects of thermal activation and magnetic interaction (**Heslop et al., 2004**). Similar to AF demagnetization the cores are tightly glued with silicone into cubes and emplaced inside the SQUID-magnetometer in rows of eight. Inside the machine the samples are subjected to 700 mT in steps of variable mT, a total of 60 measurements. The magnetic field is applied along the cylinder axis and after each step the remanent magnetization is measured. The principle behind IRM entails appliance of a magnetic field and subsequent relaxation of the magnetic field. If the coercivity of the magnetic particles is below that of the applied field the magnetic moment of the particles will alter their direction to line up more favorably with the applied field. This shift in magnetic remanence in that direction is measured (**Tauxe, 2005**).

Unraveling the IRM-acquisition curves with end-member modeling is done with an algorithm written by **Weltje, 1997** and the solutions are provided by **Heslop et al., 2004**. This algorithm operates under the assumption of linear mixing of end-members (**Aben et al., 2014**). The IRM can be considered the linear sum of all participating grains and these can be disentangled into individual components (**Robertson and France, 1994; Heslop et al., 2004**). For this statement to hold true the contributing grains should be able to be represented in log-Gaussian curves (**Robertson and France, 1994**). These curves are able to distinguish between magnetic carriers, grain sizes and composition; the peaks in the curve are associated with coercivity components (**Robertson and France, 1994**). For the end-member modeling the data provided by the IRM is treated to be a mixture of undeviating components collectively termed end members. The least squares regression is used to get the closest possible fit between the

measured composition and the 'normative' composition. A model is run in MATLAB for several end-members, from 2 up to 9, to obtain the coefficient of determination,  $r^2$ . The values for  $r^2$  fall between 0 and 1 (**Heslop & Dillon, 2007**); for useful results the  $r^2$ -value should be above 0.5 (**Gong et al., 2009b**). When plotting the coefficient of determination against the number of components the slope of the graph provides information on the best number of components. The steep part of the graph represents true data whereas the shallower, nearly horizontal part of the graph can be considered noise (**Dekkers, 2012**).

Determination of the coercivity spectrum of the individual minerals is done via the IRM-unmix software, **IRM-CLG 1.0**, developed by Pauline Kruiver. This program allows the user to interactively fit the IRM acquisition curves (**Heslop et al., 2002**). That fit allows for a quantitative assessment of the contribution towards the magnetic signal for the individual minerals. The results are displayed in a linear acquisition plot (LAP), a gradient acquisition plot (GAP) and a standardized acquisition plot (SAP) (**Kruiver et al., 2001**). An important parameter,  $B_{1/2}$ , indicates the field at which half of the IRM has reached saturation, and the corresponding value can give indications about the magnetic minerals responsible for the IRM-signal.

## 4. results and data interpretation

14 out of 19 sites pass the statistical threshold of at least a grouping of 7 cores per site for the 45° fixed cut-off. The sites that fail this condition either have a too low of a magnetic intensity to begin with and as such show random remanence directions, or simply because of the scarcity of the data. Several of the latter group do have individual cores with good results and are therefore permitted to be used in the global analysis. Additionally, several sites have multiple components and so somewhat mitigate the lack of useful results from other sites.

### 4.1 demagnetization

#### OG1

8 cores taken from the granitic Panticosa pluton dated to be Late Carboniferous ( $301 \pm 7$  Ma) in age (**Santana et al., 2006**). Thermal demagnetization gives a maximum unblocking temperature in all samples between 540 and 580 °C indicating magnetite as the carrier of the magnetic signal. This component yields a mean direction of 217.8°/40.5°,  $k=24.7$  and  $a_{95}=11.4$ . (**figure 4**). Another component has been seen at temperatures between 150 and 300 °C in 1.6 and 1.7 but scarcity of the data limits further interpretation. This direction does not coincide with the Late Carboniferous/Early Permian pole for Iberia (**Weil et al., 2010**).

#### OG2

This site samples a Devonian limestone in close proximity to the Carboniferous granite from OG1. The samples were taken in three different strike/dip regimes as to allow for the possibility of a fold test. These cores demagnetize between 270 °C and 320 °C and are devoid of a magnetic signal from 330 °C onwards. The rapid loss of magnetic intensity at these temperatures indicates pyrrhotite as the magnetic mineral. The magnetic direction derived from the demagnetization of pyrrhotite found in 8 cores is 354.8°/16.3°,  $k=5.5$  and  $a_{95}=26.1$ . Samples 2.18, 2.21 and 2.22 have been inverted to normal polarity. 5 of these cores yield tilt-corrected values of 328.8°/42.7°,  $k=4.4$  and  $a_{95}=40.9$ . Similar to the untilted variant samples 2.5, 2.18, 2.20

and 2.21 are reversed. In addition to the aforementioned component a modern-day overprint is present in sample 2.11 and 2.1 contains a reversal. Furthermore, several low temperature components have been found in different samples but the lack of quantity and consistency has proven it difficult to get useful results. They have therefore been discarded.

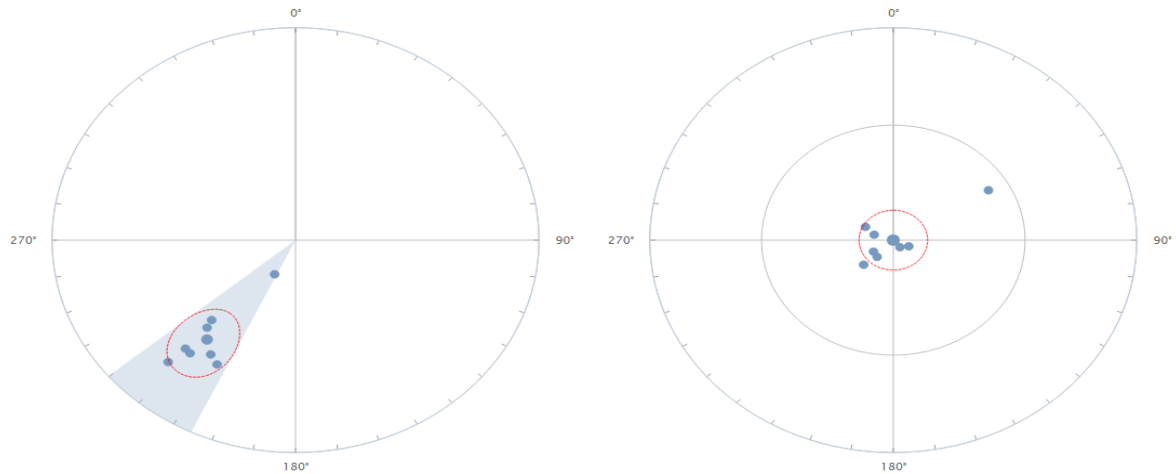


**figure 4: Characteristic remanent magnetization and a VGP plot of the mineral magnetite in the Panticosa granite (OG1).**

### OG3

Devonian limestone sampled near the village of Panticosa. None of the 8 cores drilled yield any useful results apart from two low-temperature components in 3.5 and 3.7. Two polarities have been found in these cores but the directions do not match the reversal found in OG2 (**figure 5c**).

### OG4

This site is located slightly east of OG3 and a total of 24 cores have been drilled here. The location of these cores can be categorized under three strike/dip domains, with cores 1-9, 10-17 and 18-24 having orientations of 269/36, 282/24 and 204/22, respectively. A foliation has been observed in domain A, and has a mean direction of 290/66. Two components have been identified (**figure 5a,b**). One component demagnetizes at low temperatures (0-150 °C) but the inclination (41.6°) rules out a present-day field. 13 points fall within error margins with directions of 358.8°/41.6°,  $k=11.0$  and  $a_{95}=13.1$ . The second component loses its magnetic signal at temperatures between 250 and 400 °C and consists of 10 data points with a direction of 185.9°/-38.2°,  $k=15.2$  and  $a_{95}=12.8$ . A common true mean direction has been calculated for these components based on their directional similarities. Inverting the mid-temperature component to normal polarity gives a classification of C, indicating that these components are statistically the same and combining them gives directions of 182.1°/-40.2°,  $k=12.8$  and  $a_{95}=8.8$ . Tilt correcting these values gives directions of 335.8/22.3°,  $k=10.4$  and  $a_{95}=12.4$  and 181.9°/-14.6°,  $k=9.1$  and  $a_{95}=16.9$  for the low- and mid-temperature components respectively. These components also have a common true mean direction classified as a C and combining these components give directions of 199.1°/58.9°,  $k=16.6$  and  $a_{95}=8.3$ .

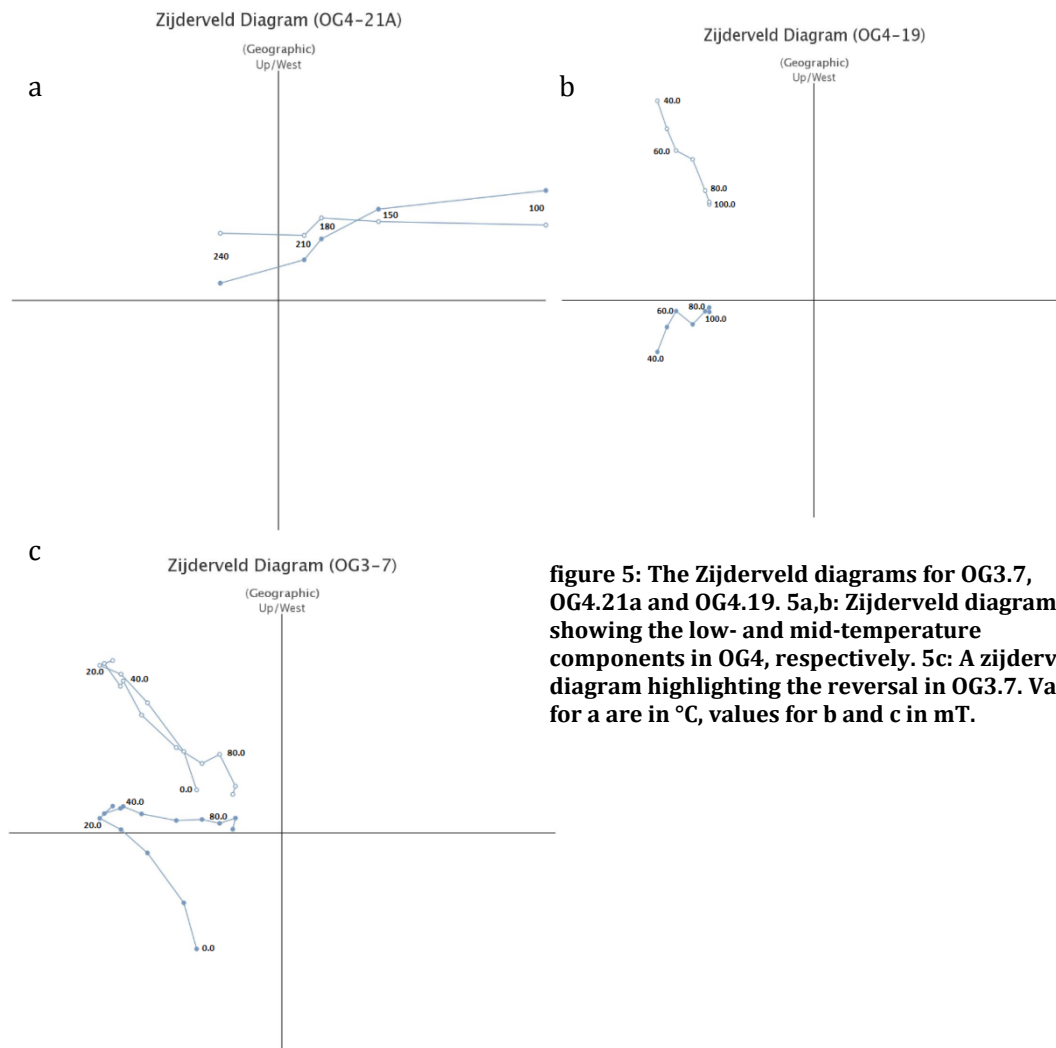


**figure 5: The Zijderveld diagrams for OG3.7, OG4.21a and OG4.19. 5a,b: Zijderveld diagrams showing the low- and mid-temperature components in OG4, respectively. 5c: A zijderveld diagram highlighting the reversal in OG3.7. Values for a are in °C, values for b and c in mT.**

## OG5 & OG6

These sites are taken in proximity of the Rio Ara near Puente de Oncins right near the border with France. Despite OG5's low intensity (regularly below 100  $\mu\text{Am}^{-1}$ ) 8 out of 11 cores give directions of  $27.6^\circ/56.5^\circ$ ,  $k=10.2$  and  $a_{95}=18.2$ . The 10 cores that have been drilled are taken from two strike/dip domains, with 1-6 and 7-10 having directions of  $320/19$  and  $273/19$ , respectively. This leads to tilt-corrected directions of  $26.8^\circ/38.3^\circ$ ,  $k=8.9$  and  $a_{95}=19.6$ . OG6, on the other hand, either suffers from unchangingly high intensities or give directions all over the place.

## OG7 & OG8

Block samples taken in France, along the D173 road near the Spanish Because of their irregular shape all samples have been demagnetized with AF. OG7 clearly shows one component, with 11 cores giving directions of  $314.3^\circ/19.4^\circ$ ,  $k=13.6$  and  $a_{95}=12.9$ . Tilt correcting these values gives  $325.1^\circ/8.9^\circ$ ,  $k=13.5$  and  $a_{95}=12.9$ , with now 11 of the 13 samples having directions within the confidence envelope.

Even though discernable demagnetization in OG8 is present the resultant directions are not compatible. The obtained directions are considerably contrasting and do not pass the statistical threshold of at least a grouping of 7 cores. Most cores demagnetize between 10 and 50 mT and the most likely bearer of the magnetic signal is magnetite.

## OG9

13 cores taken from a pelitic limestone heavily foliated with calcite veins on the road to Benasque. Demagnetization reveals pyrrhotite as the carrier of the magnetic signal. A consistent grouping of 12 cores gives a direction of  $162.3^\circ/53.9^\circ$ ,  $k=55.3$  and  $a_{95}=5.9$ . Correcting for the tilt gives a grouping of 12 cores with a direction of  $15.9^\circ/46.9^\circ$ ,  $k=51.1$  and  $a_{95}=6.4$ .

## OG10

10 cores taken from a limestone near the previous site. In similar vein to site 9 pyrrhotite is the magnetic mineral, giving directions of  $184.0^\circ/21.1^\circ$ ,  $k=15.1$  and  $a_{95}=14.7$  within 8 cores. When correcting for the tilt the directions become  $177.6^\circ/51.0^\circ$ ,  $k=15.1$  and  $a_{95}=14.7$ . In tectonic coordinates OG9 falls within the confidence envelope for OG10.

## OG11

17 cores taken from a limestone near the village of Fonchanina. The magnetic intensity of the cores is low ( $<500 \mu\text{Am}^{-1}$ ) and as a consequence the results are too scarce to be of use (only 5 data points yield a direction, giving  $281.3^\circ/34.6^\circ$ ,  $k=4.3$  and  $a_{95}=42.0$ ).

## OG12

This site, in close proximity to OG11, was specifically sampled because a dyke has intruded into the surrounding limestone rock and thus provides a perfect opportunity for a baked contact test. 26 cores have been taken with 12 and 14 from the dyke and limestone, respectively. Two components are clearly identifiable, one component demagnetizes at low temperatures and the other component constitutes pyrrhotite (**figure 6**). The low-temperature component is found in nine cores exclusively belonging to the intrusion and 7 of them give a unified direction of  $28.7^\circ/45.6^\circ$ ,  $k=10.7$  and  $a_{95}=19.4$ . Pyrrhotite is present in the limestone and gives a direction of  $125.4^\circ/21.9^\circ$ ,  $k=26.0$  and  $a_{95}=9.7$  for 10 cores. Tilt-corrected values are  $111.1^\circ/9.6^\circ$ ,  $k=13.1$  and  $a_{95}=13.1$ , with 11 cores passing the confidence envelope. Since the directions obtained from the dyke and the limestone are dissimilar the sediments do not appear to have been remagnetized by heating from the dyke. However, the presence of pyrrhotite leaves no doubt about the remagnetized character of the rock.



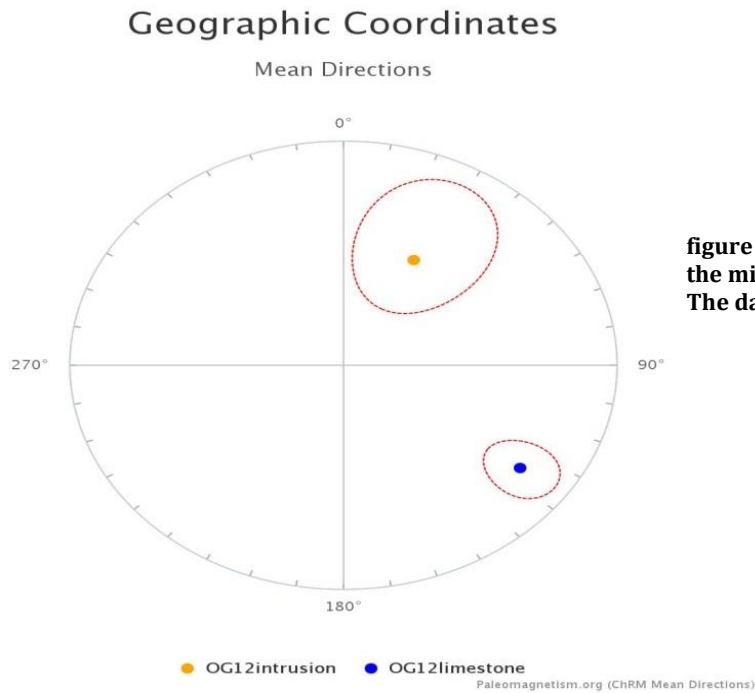


**figure 6: Characteristic remanent magnetization of the mineral pyrrhotite and the intrusion in OG12. The data points represent geographic coordinates.**

### OG13

This site consists of 14 cores and contains a fold and as such is a candidate for a fold test. The first several cores (1-7) have a  $S_0$  of 212/32 and the latter part of the cores has a strike/dip of 31/83. The measured foliation is 289/60. Similar to OG12, two components are present. The first component consists of 13 data points, demagnetizes at low temperatures (up to 250 °C) and gives a direction of 319.8°/58.2°,  $k=14.8$  and  $a_{95}=11.2$ . The second component demagnetizes from 480 °C onwards and has a direction of 257.9°/25.2°,  $k=11.1$  and  $a_{95}=12.0$ . Correcting for the tilt gives a direction of 312.3°/40.5°, with  $k=9.0$  and  $a_{95}=18.2$  and 260.7°/10.5°,  $k=6.4$  and  $a_{95}=23.7$  for the low- and mid-temperature components, respectively. The fold test is negative (**figure 7a**), for both components, indicating magnetization has been acquired post-tectonic activity

### OG14

This site has 13 cores taken near the crossing to the village of Iran at the L-500 highway. The cores demagnetize at low temperatures (up to 330° C), with pyrrhotite being the carrier of the magnetic carrier. The Curie balance reveals the presence of pyrite at temperatures higher than 400° C. 5 out of 8 cores brought about by the demagnetization of pyrrhotite give a direction of 26.3°/-3.0°,  $k=17.0$  and  $a_{95}=19.1$ . Tilt correction gives 150.4°/-17.7°,  $k=11.4$  and  $a_{95}=28.4$ . Three other cores (OG14.3A, OG14.4B and OG14.6B) plot in the lower half of the lower hemisphere projection. Reversing these data points makes all cores pass the statistical threshold for tectonic coordinates, with 7 out of 8 of cores passing the aforementioned statistical threshold for geographic coordinates. Core OG14.3A's direction does not coincide with the directions that the rest of OG14 give and therefore is not included in the results.

The presence of a fold allows a fold test to be undertaken (**figure 7b**). With the relative paucity of the data a fold test is construed with the highest tau between -40 and 116% unfolding. The magnetization in this site therefore coincides with the folding phase. This is in stark contrast to the fold test for OG13. However, as mentioned previously the data is not reliable as that of OG13.

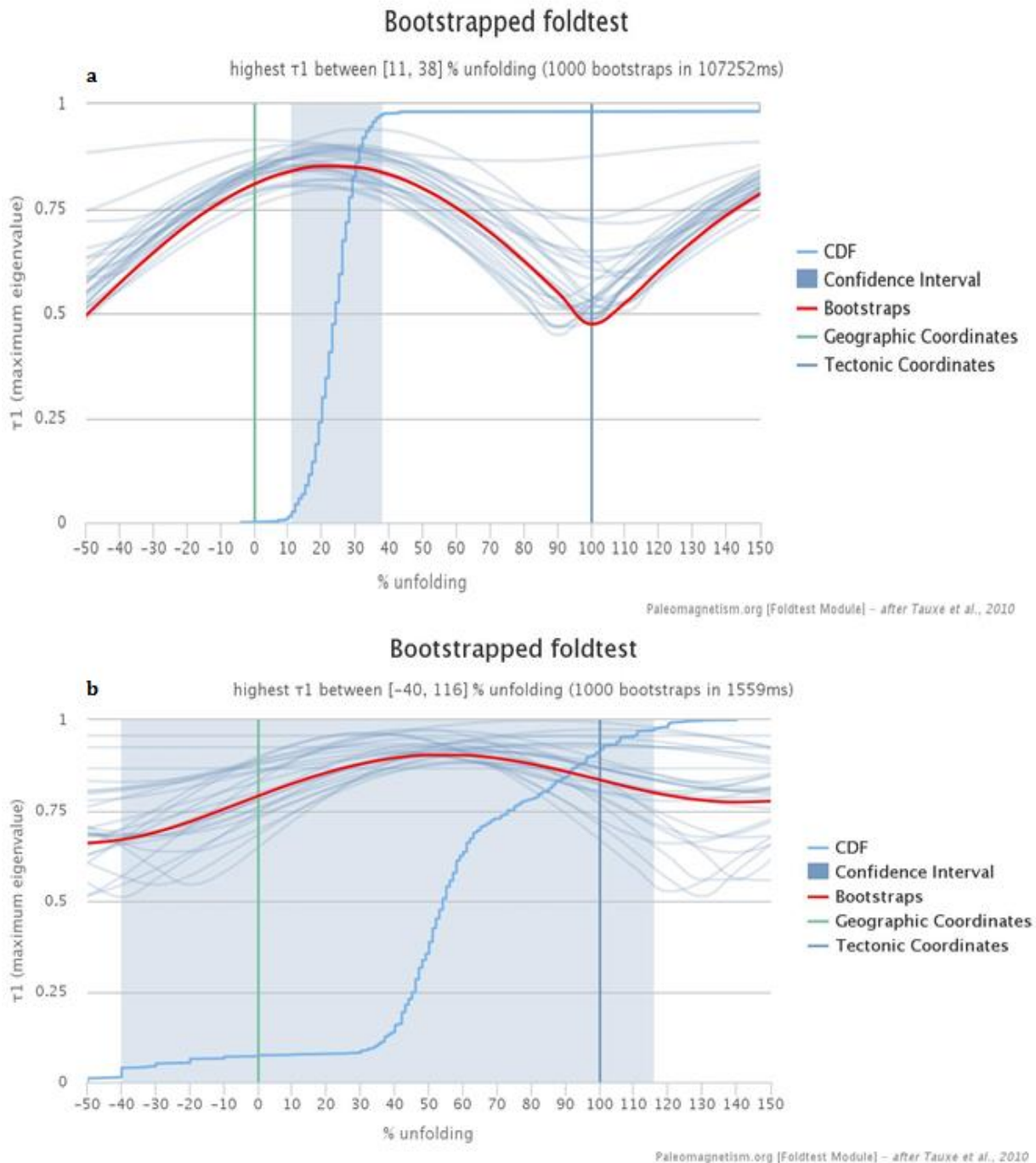


**figure 7a:** Fold test for the first components present in OG13. The highest tau is achieved for 20% untilting, indicating that the magnetization has been primarily acquired post-folding. **7b:** The fold test for OG14, showing the maximum tau between 50% and 60% unfolding. This fold test perhaps shows two components, with one component possibly being pre-folding.

## OG15

11 cores are taken from a Devonian limestone near the road between Llavorsi and La Poble de Segur. Demagnetization reveals two components. The low-temperature component loses its magnetic signal at temperatures approaching 250 °C and the second component steadily demagnetizes between 250 °C and 450 °C. The first component gives a direction of 306.8°/28.5°,  $k=9.6$  and  $a_{95}=14.1$  (bedding correction: 288.0°/10.0°,  $k=19.5$  and  $a_{95}=10.1$ ), and this direction can be construed as to represent a Cretaceous direction. Sample 15.1C has been reversed to better fit the aforementioned direction. The second component has a shallower inclination giving 289.8°/14.6°,  $k=45.8$  and  $a_{95}=5.5$  (bedding correction: 289.5°/-13.6°,  $k=45.8$  and  $a_{95}=5.5$ ).

## OG16 & OG17

These sites are part of the Llavorsi syncline, with OG16 and OG17 being sampled in the overturned and normal limb, respectively, ideal for a fold test. Unfortunately, OG16 is failing to produce any useful results as a consequence of its low magnetic intensity ( $<100 \mu\text{Am}^{-1}$  is a common occurrence) and thus the possibilities for a useful fold test are lost. 6 out of 10 cores give directions of 204.4°/-27.1°,  $k=6.0$  and  $a_{95}=29.8$ . The lack of quantity as well as the large error does not make a reliable site, and as such has not been included in table 4 and figure 4.

For OG17, Cores 17.1 and 17.2 sample an intruded boudin of volcanic origin and so additionally this site provides a baked contact test. The magnetic mineral responsible for the magnetic signal is once again pyrrhotite, this time giving a direction of 165.7°/-42.8°,  $k=30.8$  and  $a_{95}=11.1$ . A bedding of 287/50 gives tilt-corrected directions of 174.6°/2.5°,  $k=30.8$  and  $a_{95}=11.1$ . Adding the results from the boudin gives a combined direction of 168.7°/-40.1,  $k=19.9$  and  $a_{95}=11.8$ , indicating that the magnetization postdates the intrusion, and as such cannot be primary.

## OG18 & OG19

The last two sites were taken in Of these sites, OG18 is of limited value since the data derived from demagnetization is scarce, with only 4 data points giving a direction of 152.8°/-54.4°,  $k=66.0$  and  $a_{95}=11.4$ . OG19 gives better results, with a 17 data points giving a direction of 151.8°/-50.8°,  $k=120.2$  and  $a_{95}=3.3$ . Since OG18 and OG19 were taken close together and show similar results they have been combined to give a value of 332.9°/50.8,  $k=119.6$  and  $a_{95}=3.3$ . Beddings of 269/51 and 260/60 for OG18 and OG19, respectively, give tilt-corrected directions of 340.1°/-5.4,  $k=67.1$  and  $a_{95}=4.4$ .

In addition to the good demagnetization results the presence of an isoclinal fold allows for a fold test. The fold test is negative (**figure 8**), once again indicating that the magnetization was occurred post-folding.

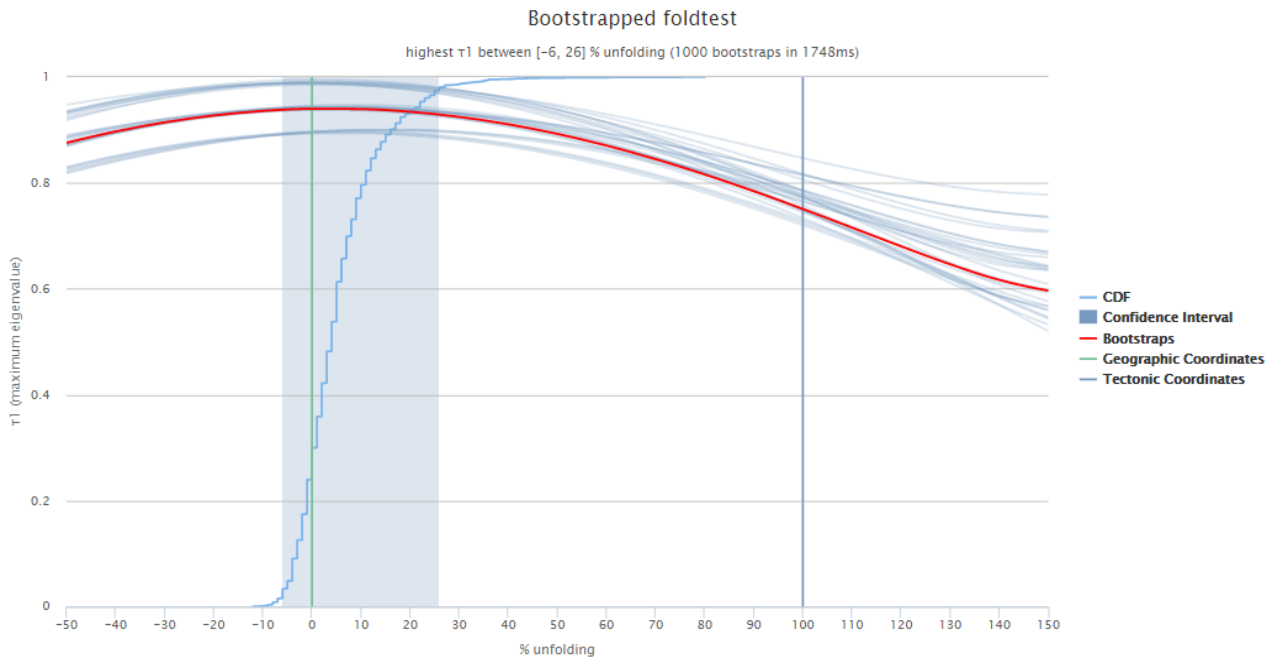


figure 8: Fold test for OG19. The highest  $\tau$ -values are between -6 and 26 % unfolding. These percentages show that the magnetization cannot be of a primary character.

### overview

Of the 19 sites, 5 have been discarded since the paucity of the data does not allow any meaningful statistical interpretation. The minerals responsible for the magnetism in the remaining 14 sites are equally split between pyrrhotite and magnetite. These pyrrhotite components have lost most of their magnetic intensity after 330 °C whereas samples containing magnetite can demagnetize at temperatures up to 580 °C. The inclination of several low-temperature (<250 °C) components such as those found in OG4, OG13 and OG15 rule out a present-day field as the cause for their magnetic intensity. As shown in figure 12 and table 4 individual sites plot in every quadrant though the upper left quadrant is definitely more densely populated.

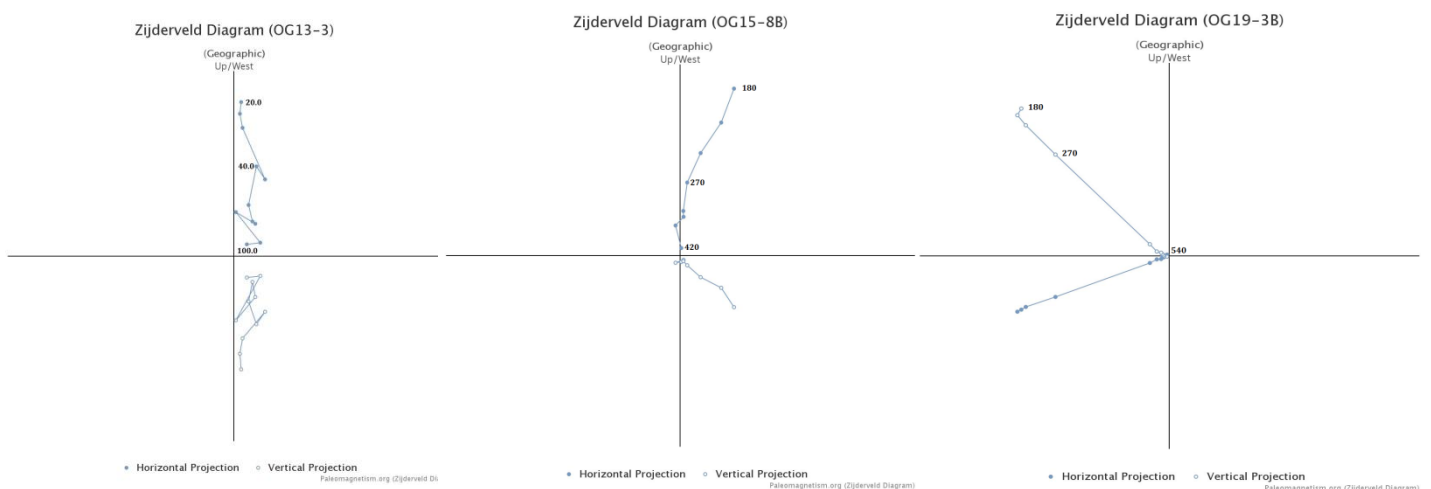


figure 9. Representative Zijdeveld diagrams for the components present in OG13, OG15 and OG19.

site	No bedding correction				bedding correction				notes
	N/N*	dec°/inc°	k	a <sub>95</sub> °	N/N*	dec°/inc°	k	a <sub>95</sub> °	
OG1	8/8	217.8/40.5	24.7	11.4	-	-	-	-	magnetite
OG2	8/8	354.8/16.3	5.5	26.1	5/8	328.8/42.7	4.4	40.9	pyrrhotite
OG3	-	-	-	-	-	-	-	-	too scarce
OG4ltc	13/17	358.8/41.6	11.0	13.1	15/17	355.8/22.3	10.4	12.4	magnetite
OG4mtc	10/10	185.9/-38.2	15.2	12.8	10/10	181.9/-14.6	9.1	16.9	magnetite
OG5	8/11	27.6/56.5	10.2	18.2	8/11	26.8/38.3	8.9	19.6	magnetite
OG6	-	-	-	-	-	-	-	-	too scarce
OG7	11/13	314.5/19.4	13.6	12.9	11/13	325.1/8.9	13.6	12.9	magnetite
OG8	-	-	-	-	-	-	-	-	too scarce
OG9	12/12	162.3/53.9	55.3	5.9	12/12	165.9/41.3	55.3	5.9	pyrrhotite
OG10	8/8	184.0/21.1	15.1	14.7	8/8	177.6/51.0	15.1	14.7	pyrrhotite
OG11	-	-	-	-	-	-	-	-	too scarce
OG12ltc	7/9	28.7/45.6	10.7	19.4	-	-	-	-	magnetite
OG12mtc	10/13	125.4/21.9	26.0	9.7	11/13	111.1/9.6	13.1	13.1	pyrrhotite
OG13ltc	13/16	319.8/58.2	14.8	11.2	9/16	312.3/40.5	9.0	18.2	magnetite
OG13mtc	15/17	257.9/25.2	11.1	12.0	8/17	260.7/10.5	6.4	23.7	magnetite
OG14	7/7	46.6/47.7	8.9	21.4	7/7	27.8/17.7	7.4	23.8	pyrrhotite
OG15ltc	13/13	306.8/28.5	9.6	14.1	12/13	288.0/10.0	19.5	10.1	magnetite
OG15mtc	16/16	289.8/14.6	45.8	5.5	16/16	289.5/-13.6	45.8	5.5	magnetite
OG16	-	-	-	-	-	-	-	-	too scarce
OG17	7/7	345.8/42.8	30.8	11.1	7/7	354.6/-2.5	30.8	11.1	pyrrhotite
OG18&19	17/18	152.9/-50.8	120	3.3	17/18	160.1/5.4	67.1	4.4	pyrrhotite

table 4: This table gives a schematic overview of the results for all the sites. Sites that do not pass the statistical threshold as defined in the methods are labeled 'too scarce'. All the results are of normal polarity.

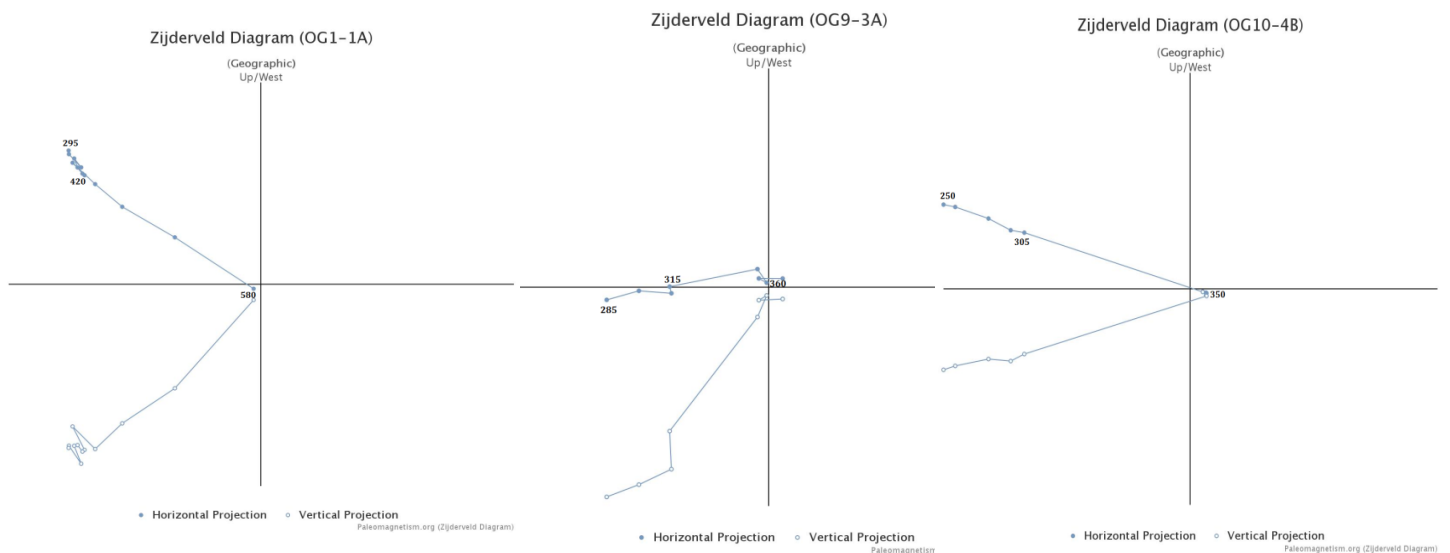


figure 10. Representative Zijderveld diagrams for the components present in OG1, OG9 and OG10.

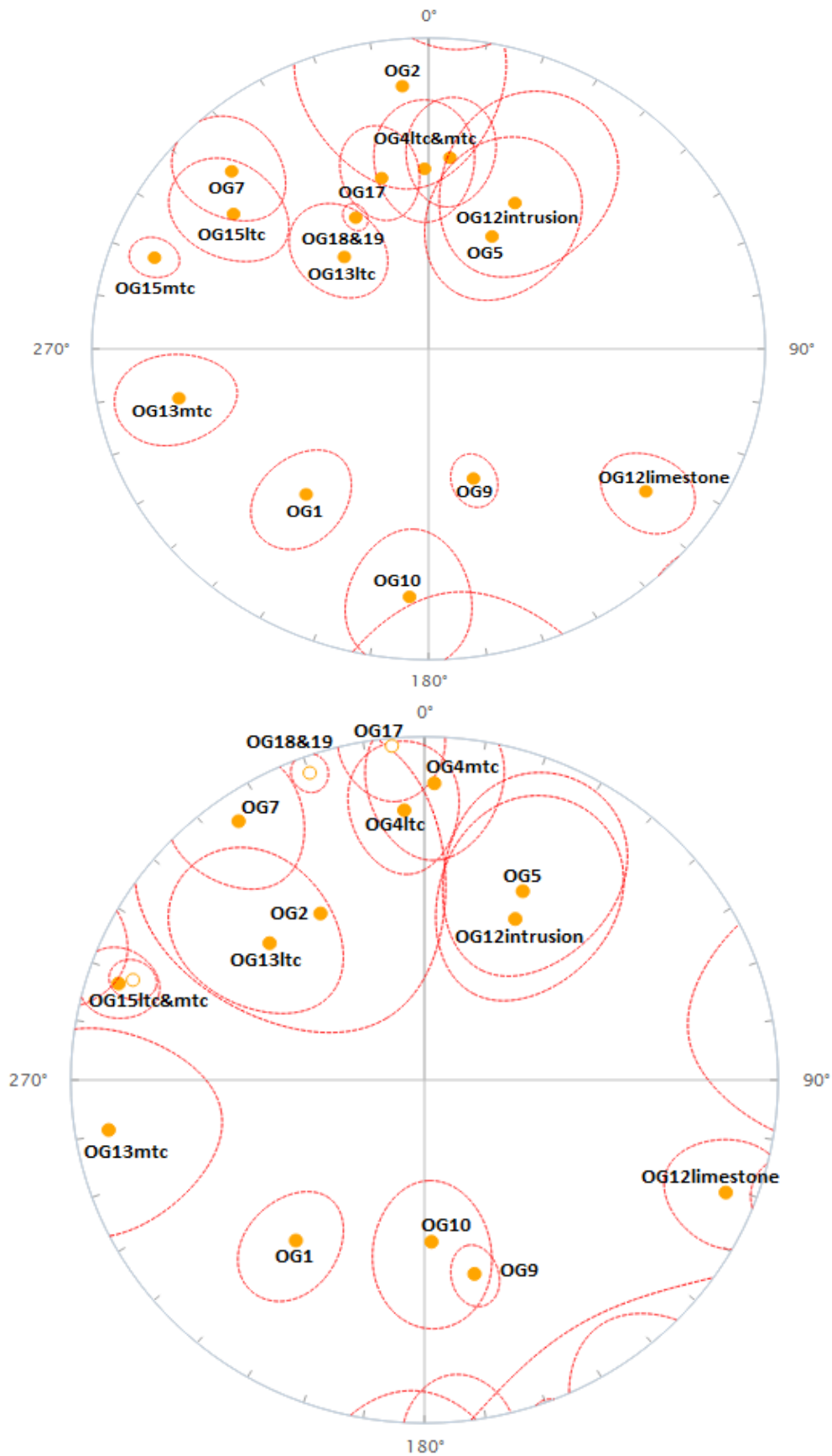


figure 11: Geographic (upper figure) and tectonic (bottom figure) coordinates of the mean directions of the relevant sites. Only the sites that pass the statistical threshold have been included here. OG18&OG19 and the medium-temperature component in OG4 are displayed in reversed polarity.

## 4.2 Curie balance

The Curie balance can help distinguish the minerals in the sample that carry the magnetic signal. One sample per site is sufficient to gain insight into the minerals present except for those sites that sample multiple lithologies. Some of the results can be seen in figure 12. These graphs plot the temperature and the magnetization on the x-and y-axis, respectively. The thin solid line represents the path for temperature increments and the thick solid line the cooling curve. The peaks and subsequent fall of the magnetization observed in these graphs are characteristic for certain minerals.

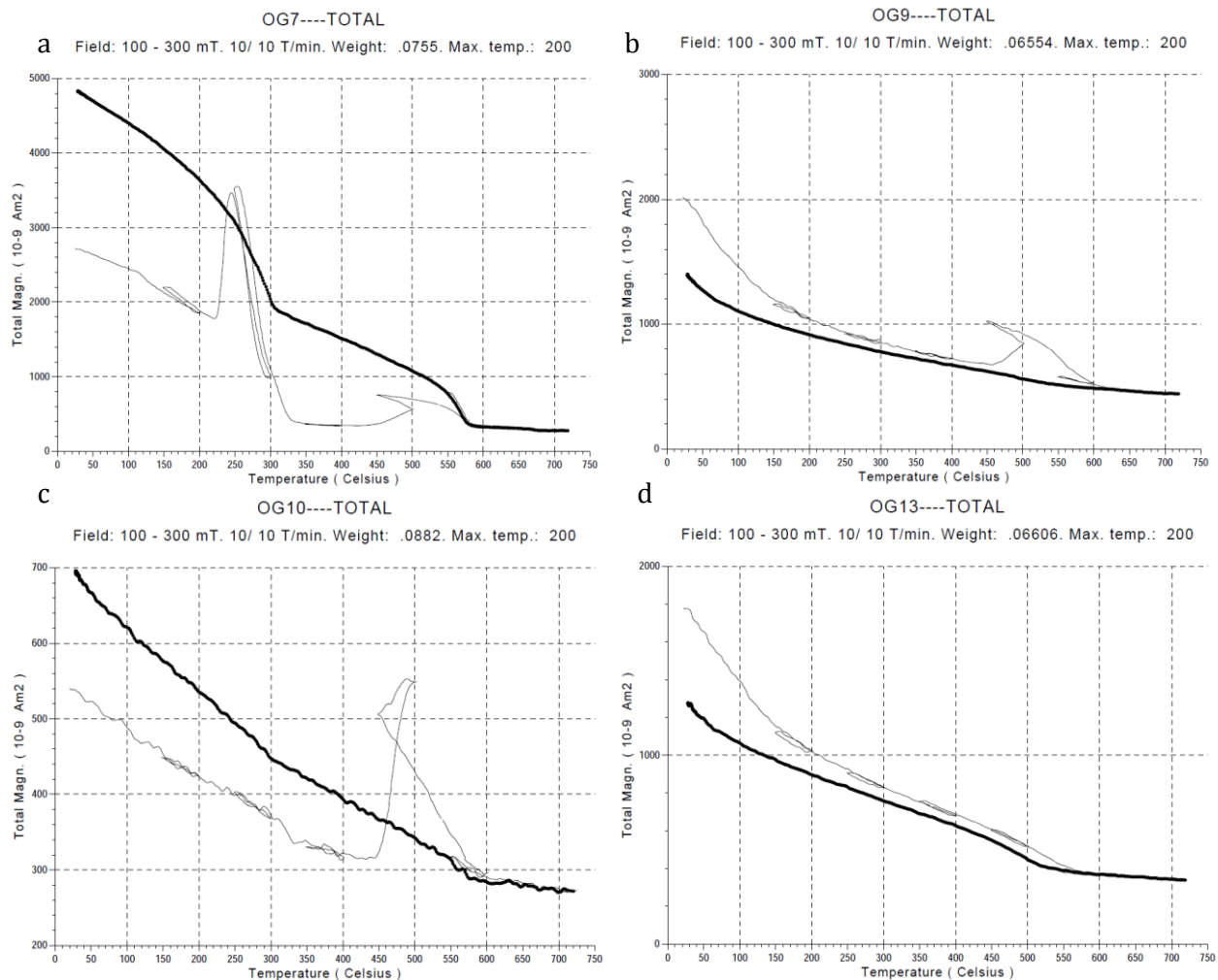


figure 12. Results from the Curie balance for the sites OG7 (12a), OG9 (12b), OG10 (12c) and OG13 (12d). These curves are representative for the rest of the sites.

In figure 12a, a sample from OG7, the sharp loss of magnetization after 250 °C is distinctive for pyrrhotite which has its Curie temperature of 325 °C. A further irregularity at temperatures exceeding 500 °C is indicative of magnetite. Since all samples from OG7 have had the AF treatment, in which pyrrhotite does not demagnetize properly, the presence of pyrrhotite has gone by unnoticed in the demagnetization process and magnetite is solely deemed responsible for the magnetic signal. Another discrepancy can be observed for OG9 (figure 13b). Both thermal and AF demagnetization clearly show pyrrhotite as the bearer of the magnetic signal yet the result from the Curie balance only highlights the presence of magnetite, with a loss of

magnetization after 500 °C. The presence of magnetite does not necessarily result in the aforementioned decline in magnetization after 500 °C. Similar trends for both the heating and cooling curve, as observed in figure 10d and, to a lesser extent, 11b, are also indicative of magnetite. A large peak observed in the heating curve starting at 450 °C (**figure 12c**) is characteristic for pyrite. The supplemental data from the Curie balance is in good accordance with the results from the thermomagnetic runs for the majority of the sites.

### 4.3 anisotropy of magnetic susceptibility

The anisotropy of magnetic susceptibility is a tool to determine any preferred orientation in the minerals. Most sites have mean bulk susceptibility values around the order of  $10^{-4}$  whereas some sites can be as low as  $10^{-6}$ . This indicates contribution of both para- and ferromagnetic minerals (**Hrouda & Jelinek, 1990**). There is a clear clustering of K1, K2 and K3 values for the sites OG1, OG9, OG13, OG15, OG16, OG18 and OG19 (**figure 13**). The other sites show no signs of a general trend and have limited anisotropy (max of 5% for most sites). They will not be further discussed. The sites OG1, OG18 and OG19 have similar susceptibility axes (**figure 13a**), with combined directions of 280.4/22.8, 32.2/41.4 and 169.9/39.9 for the maximum, intermediate

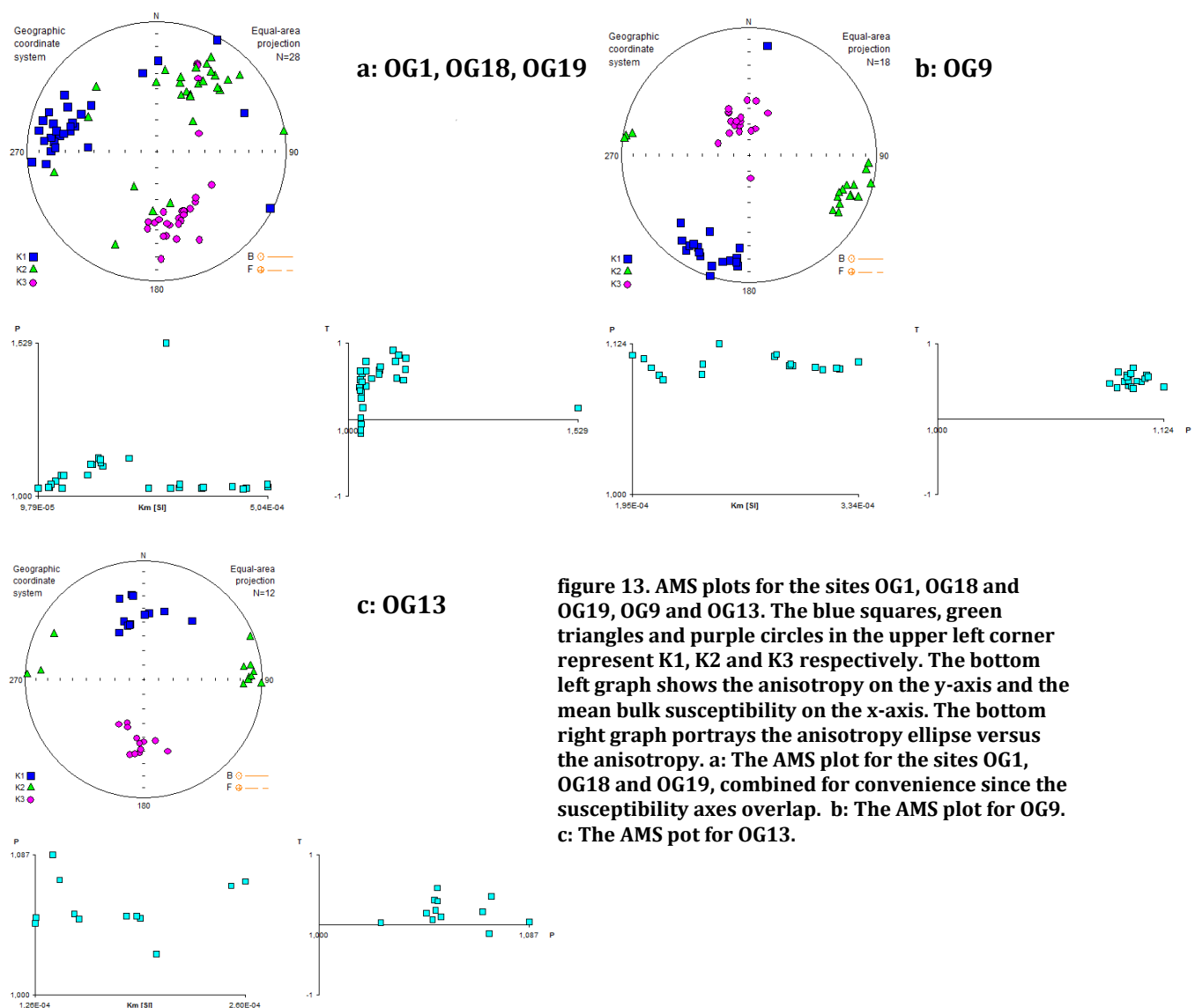


**figure 13. AMS plots for the sites OG1, OG18 and OG19, OG9 and OG13. The blue squares, green triangles and purple circles in the upper left corner represent K1, K2 and K3 respectively. The bottom left graph shows the anisotropy on the y-axis and the mean bulk susceptibility on the x-axis. The bottom right graph portrays the anisotropy ellipse versus the anisotropy. a: The AMS plot for the sites OG1, OG18 and OG19, combined for convenience since the susceptibility axes overlap. b: The AMS plot for OG9. c: The AMS plot for OG13.**



and minimum magnetic susceptibility direction respectively. OG1 and OG18 have anisotropy percentages of 5, whereas the anisotropy in OG19 can increase to 12%, similar to OG9 (**figure 13b**). The anisotropy for OG13 is equally low when compared to the sites lacking clustering susceptibility directions (**figure 13c**).

#### 4.4 hysteresis loops

Several representative results from the Micromag are portrayed in figure 15. In these plots the magnetization (normalized) is plotted against the applied field. The shape in figure 15a is a good example of a pseudo-single domain in which the loop is quite tight in the midsection of the graph, with lower values for the  $M_r/M_s$  ratio than for true single-domains. In pseudo-single domain the particles are allowed to divert slightly from the parallel spinning characteristic for single domains (**Tauxe, 2005**). In addition to OG2 the same loop can be observed in the majority of the sampled sites, regardless of the magnetic carrier. The hysteresis loop for OG4 (**figure 15b**) looks similar to OG2 but the loop is closed earlier than in the previous example. This hints at superparamagnetic behavior, also observed, albeit to a lesser extent, in OG11 and OG19.

When plotting the squareness against the coercivity (**figure 14**) all sites except OG8 are clustered between a squareness of 0.085 and 0.0125, with most of the samples between 0.105 and 0.115. Squareness is defined as the ratio of saturation remanence ( $M_r$ ) and saturation remanence ( $M_s$ ). For magnetite the squareness values for pseudo-single domain lie between 0.05 and 0.5 (**Tauxe, 2005**), further strengthening the notion that pseudo-single domain is the dominant magnetic

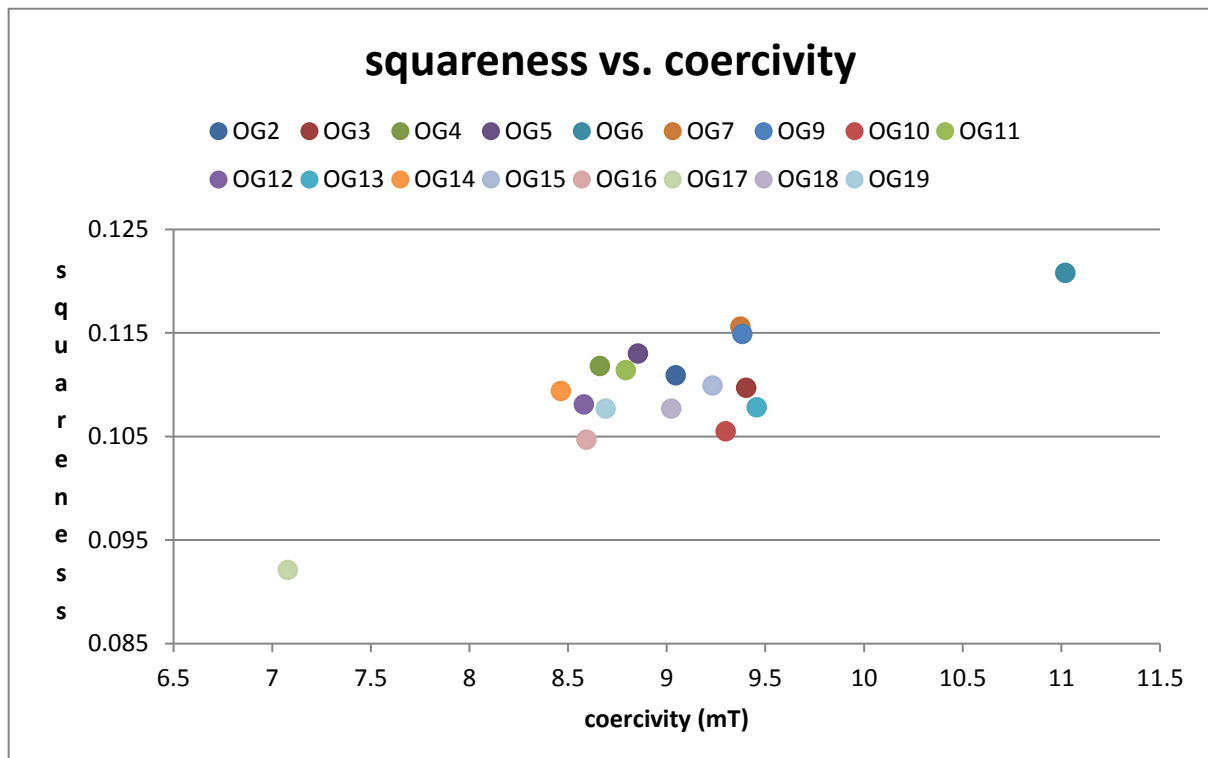


figure 14. Squareness vs. coercivity plot for the included sites. Values for the squareness between 0.05 and 0.5 indicate pseudo-single domain behavior,

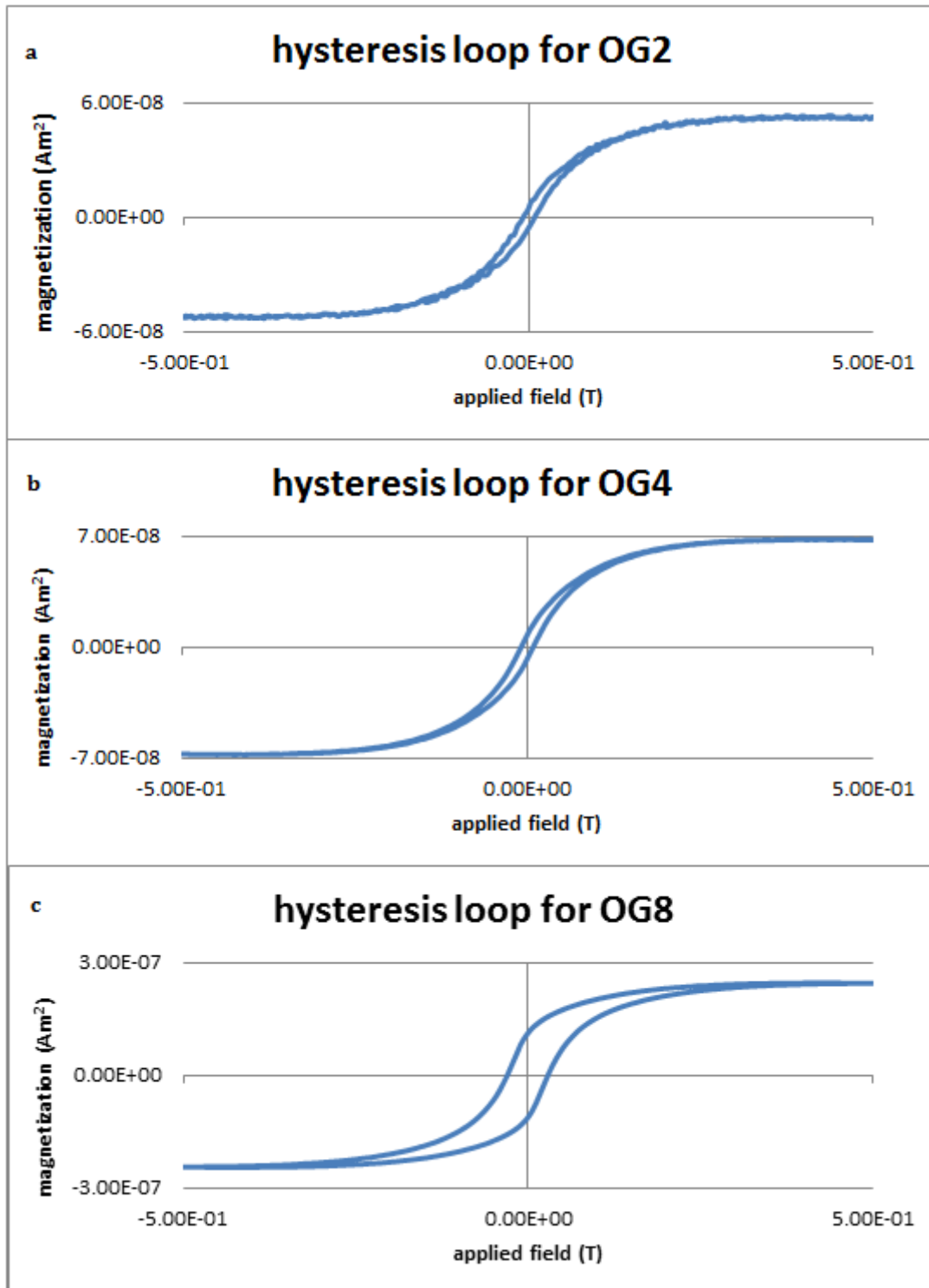


figure 15: Representative hysteresis loops of the sampled sites. 15a: A pseudo-single domain has been observed in OG2. 15b: The tight loop in OG4 might indicate superparamagnetic behavior. 16c: The loop for OG8, approaching true single domain behavior.

state in the samples. OG8 (figure 14) is an exception, having a squareness value of 0.45 approaching the values for single domain (>0.5) (Tauxe, 2005). Its hysteresis loop is also considerably less tight (figure 15C) than those observed for the other sites. This more open pattern is characteristic for true single domain.

## 4.5 isothermal remanent magnetization and end-member modeling

The model was run for nine end-members first as to allow for a thoughtful decision on the optimal number of end-members. In figure 16 the values of  $r^2$  are plotted against the number of end-members. There is a steep increase in the slope from 2 to 3 end-members but subsequently the slope is way shallower. This part of the graph likely represents noise (Dekkers, 2012) and for that reason the optimal number of end-members hover near 2 or 3. In similar vein in figure 17 the value for  $r^2$  has been plotted against the applied field in mT. The nine end-members in this model can be reduced to two, possibly three, end-members based on the characteristics of the curve. The first component has a steep incline below 100 mT and saturates (reaches unity for  $r^2$ ) quickly at 200 mT. End-members 1, 2, 3 and 8 are part of this. The second component has a gentler curve and steadily approaches unity at 700 mT. End-members 7 and 9 belong to this component. The third component is intermediate between the others, and can be, from an interpretational viewpoint, considered a mixture of the other two aforementioned components. End-members 4, 5 and 6 fall into this category.

Based on figure 17 nine end-members are a clear overrepresentation of the data. As a result the model has been rerun for two, three and four end-members, based on the information presented in graph 17. With four end-members the fourth end-member is clearly a combination of the first and third end-member from an interpretational viewpoint and therefore does not provide any new information. The results of the rerun for 3 and 2 end-members are portrayed in figure 18. Considering a two end-member model the first end-member saturates at 200 mT whereas the second end-member increases steadily yet never reaches saturation (figure 18a). In the three end-member model the first two end-members behave similarly to those in the two end-member solution. The third end-member quickly reaches 80% saturation, then gets overtaken by the first end-member at 100 mT and, similar to the third end-member, never reaches full saturation (figure 18b).

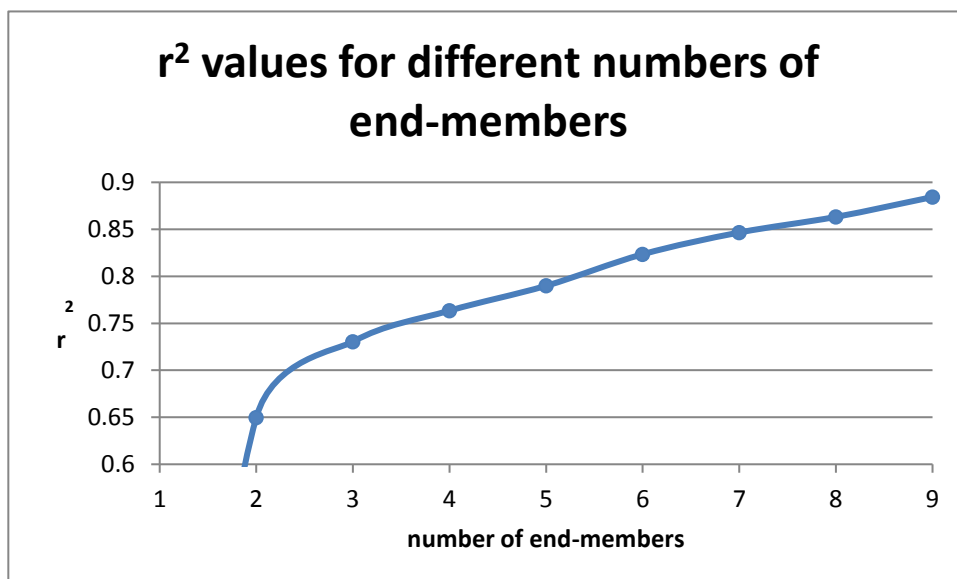


figure 16: The values for  $r^2$  plotted against the number of components. The bend in the curve details the optimal number of end-members. For these samples the ideal amount falls between 2 and 3.

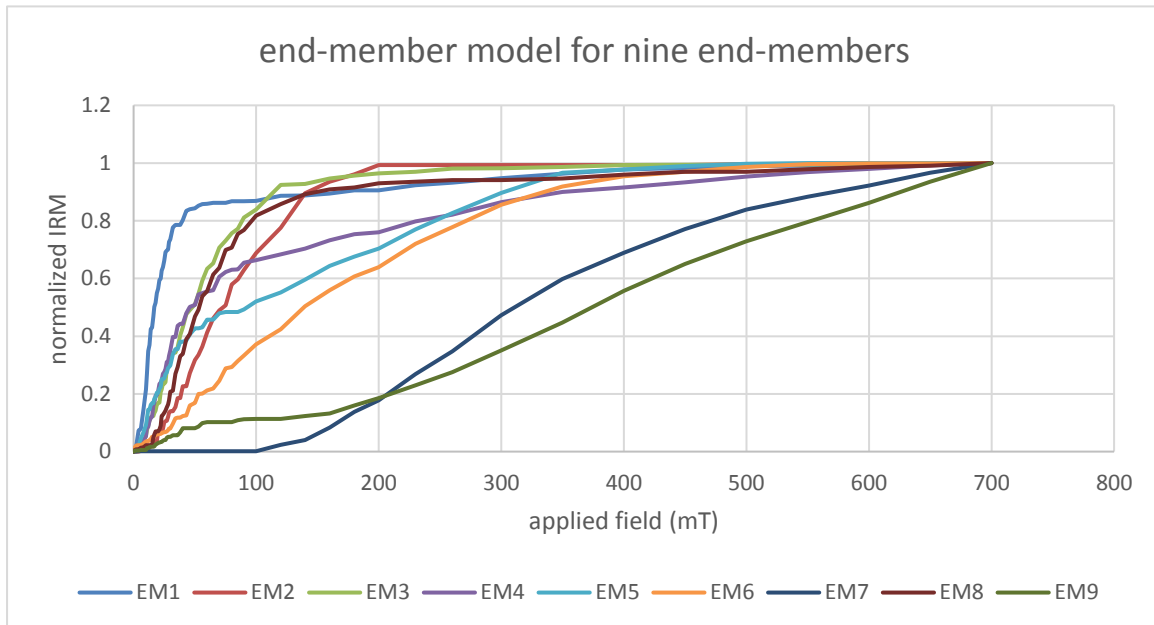


figure 17: The model for nine end-members. Two, possibly three end-members can be seen in the graph.

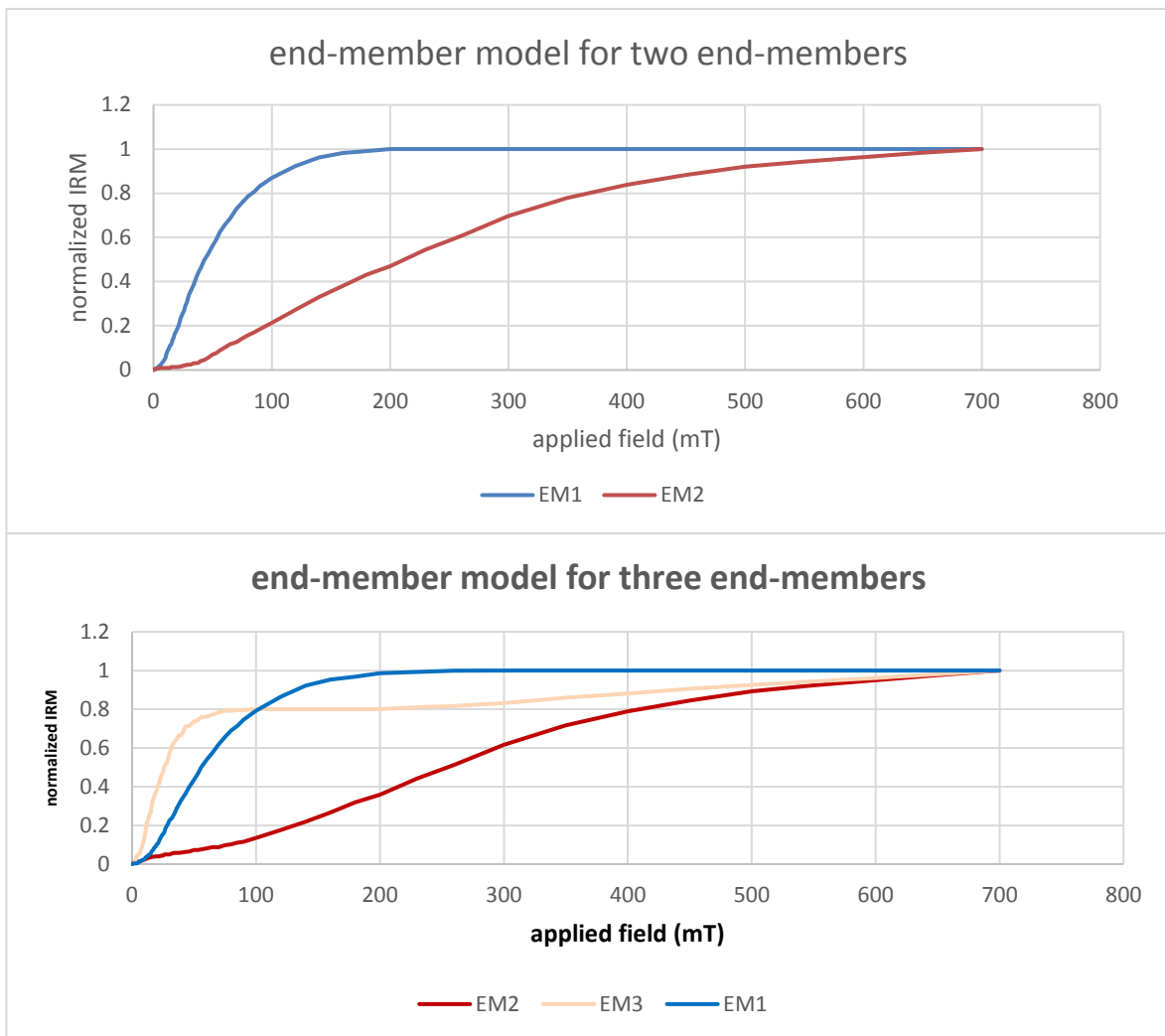
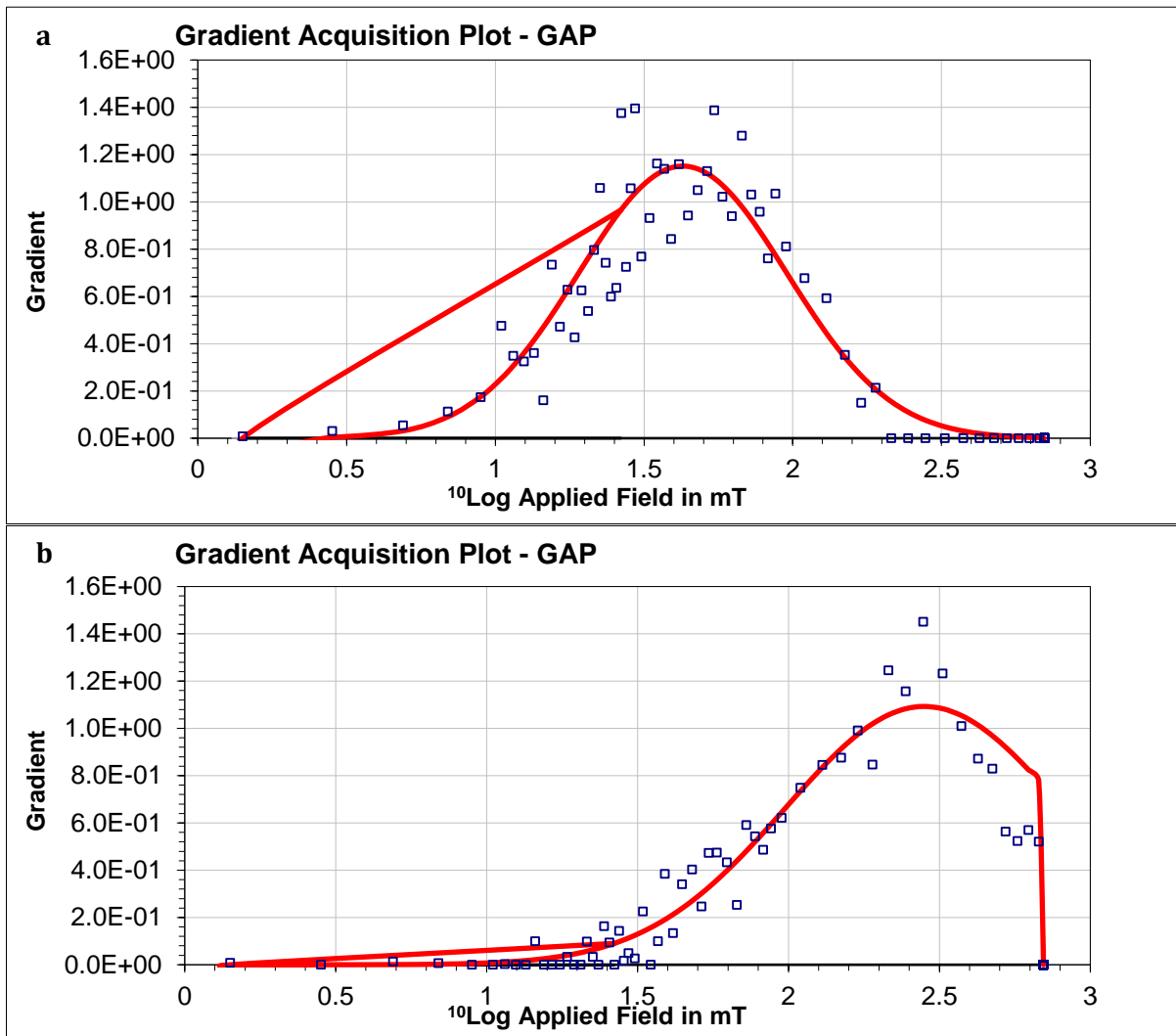


figure 18: These figures show the end-member model for two (18a) and three (18b) end-members. 19a: The first end-member saturates quickly while the second end-member never reaches saturation. 19b: The first two end-members show similar behavior and the third end-member is intermediate between the first two.

The IRM-component fitting of each end-member for the two end-member solution can be found in figure 19. This figure shows the GAP acquisition plot of the idealized end-member solutions. The first end-member contains a soft component that reaches its highest gradient around 40 mT (**figure 19a**). The second end-member has a harder component that maxes out at 250 mT (**figure 19b**). This component is not fully saturated. As can be seen in the graphs both end-members can best be represented by a single component, with  $B_{1/2}$  values of 42.7 mT and 281.1 mT for the first and second end-member, respectively.



**figure 19: Gradient acquisition plots of the two end-members. 19a: The first end-member has a peak at 1.63, corresponding to a  $B_{1/2}$  value of 42.7 mT. 19b: The second end-member has a peak at 2.45, corresponding to a  $B_{1/2}$  value of 281.1 mT.**

GAPs of the three end-member solution are presented in figure 21. The first and second end-members in the three end-member solution are quite similar to those in the two end-member solution. The first end-member has a component with its peak at 56 mT (**figure 20a**). The second end-member has a hard component around 250 mT and a smaller, barely noticeable softer component at  $10^{1.5}$  mT (**figure 20b**). The third end-member has two peaks at around 32 mT and 160 mT (**figure 20c**). The hard components in both the second and third end-member have not reached saturation. Compared to the two end-member model the components in the first and second end-member are slightly softer and harder, respectively. This is reflected in the third end-member, which, compared to the first and second end-member in the two end-

member model, has its peaks at slightly lower and higher values, respectively. From an interpretational standpoint the third end-member seems to be a combination of the first and second end-member, with a slightly lower attribution of the soft component and a slightly elevated contribution of the hard component when compared to the individual components.

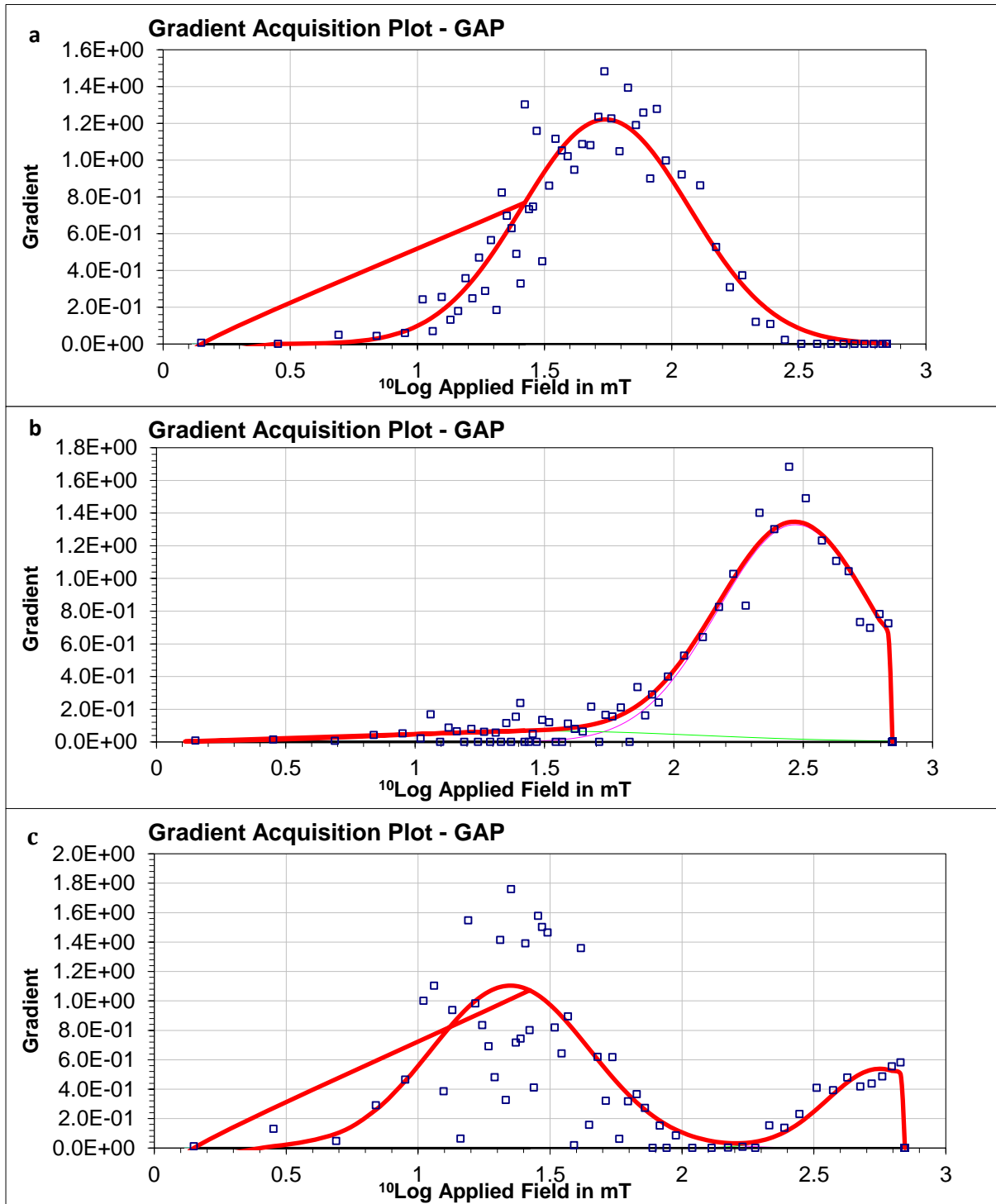
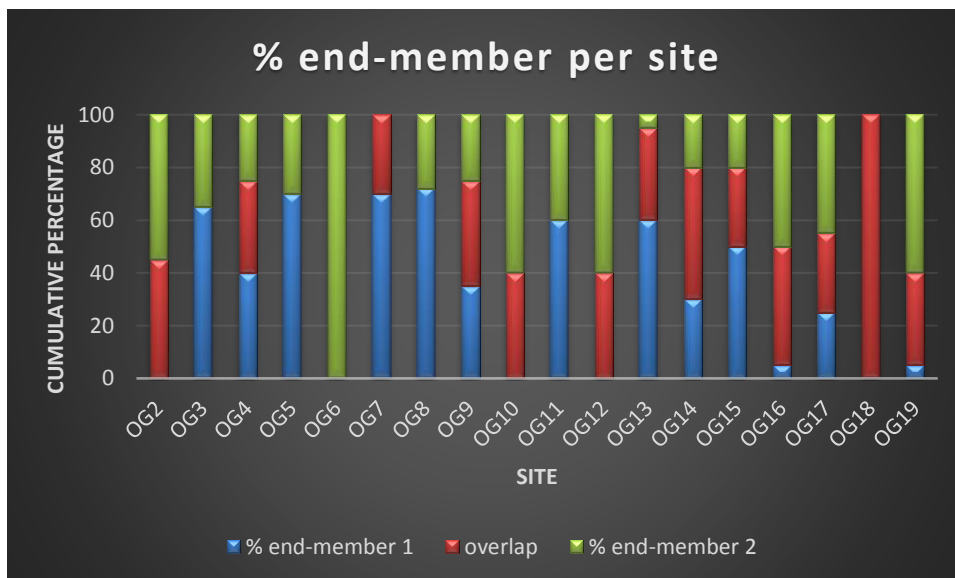


figure 20: Gradient acquisition plots of the three end-members. 20a: The first end-member has a peak at 1.74, corresponding to a  $B_{1/2}$  value of 55. 20b: The second end-member has two components with peaks at 1.50 and 2.74, corresponding to  $B_{1/2}$  values of 31.6 and 295.1. 20c: The third end-member has the highest gradients at 1.35 and 2.75. These values give a  $B_{1/2}$  of 22.4 and 562.3.

For three end-members only 16 individual specimens have a meaningful contribution (above 20%) towards the third end-member, with 39 of the 88 sites having no contribution at all. The addition of the third end-members does not allow for a more distinctive discrimination, and, when combined with the fact that the slope in figure 15 for three end-members is quite shallow, a decision has been made to continue with two end-members from this point onwards. In the following section the contributions towards each end-member per site will be detailed. The numbers represent percentages, with 1 equaling 100 per cent.

## overview

Figure 21 shows that the first end-member dominates in the sites OG4, OG7, OG13, OG14 and OG15. It is also prevalent in OG9. The second end-member is abundant in OG2, OG9, OG10, OG12, OG17 and OG18&19. Since the sites OG3, OG5, OG6, OG10 and OG11 lack quantity concerning the amount of cores these sites tell a one-sided story, and therefore it is hard to include them in the analysis.



**figure 21: Overview of the end-member contributions per site. The blue bars are percentages exclusively belonging to end-member 1 whereas the green bars list percentages for end-member 2. The red bars show the overlap between the two end-members. In OG4, for example, the first end-member makes up at least 40% but can be as high as 75%. Consequently, the second end-member contributes at least 25% but its contribution can be as high as 60%. The red bar thus represents anything between 40%-75%. Core 19.19 has been omitted due to its contribution pattern being in stark contrast to the other cores belonging to OG19.**

When comparing the information from table 4 and figure 21 there is a strong correlation between the end-members and the magnetic mineral responsible for the magnetic signal. The first end-member is ample in sites that contain magnetite whereas the second end-member occurs readily in sites with pyrrhotite. OG9 is a mixture of two end-members, and while the directional data is certainly brought about by the demagnetization of pyrrhotite, Curie balance reveals the presence of minor magnetite. The  $B_{1/2}$  value for the component present in the first end-member is near 40 mT, which is indicative of magnetite (Heslop et al., 2002). Since the first end-member is only made up of the aforementioned component the first end-member likely represents magnetite. The second end-member is prevalent in sites which reveal pyrrhotite to be the carrier of the magnetic signal. Pyrrhotite is a hard mineral magnetically, and

so a  $B_{1/2}$  value of 281.1 mT for the component in the second end-member is in good accordance with theory. The first and second end-members therefore represent magnetite and pyrrhotite, respectively. Figure 21 also shows that most sites have contributions of both minerals.

## 5. discussion

Magnetization in the sampled sites is exclusively recorded in the minerals pyrrhotite and magnetite as evidenced by demagnetization patterns, Curie balance and the results from end-member modeling. The directional results obtained from demagnetizing the aforementioned cores are very polarizing, especially when considering that the results plot in every quadrant. Some sites appear to have a common direction while others can best be described as lone souls. The presence of pyrrhotite and negative fold tests in OG13 and OG19 argue against primary Devonian magnetism. Furthermore, the absence of paleomagnetic directions from Devonian rocks coinciding with directions found in **Tait et al., 2000** also discourage ideas of an established Devonian direction.

However, the anisotropy of magnetic susceptibility reveals the presence of fabric in some sites. This fabric may have biased the directional results from demagnetization and render these directions meaningless. It is therefore important to ensure whether this has occurred before considering the ramifications of the actual directions.

### 5.1 real or 'fabricated' results

As mentioned previously the fabric in the sites revealed by AMS become problematic when the directional data from demagnetization plots on the plane between K1 and K2. Of the 19 sites

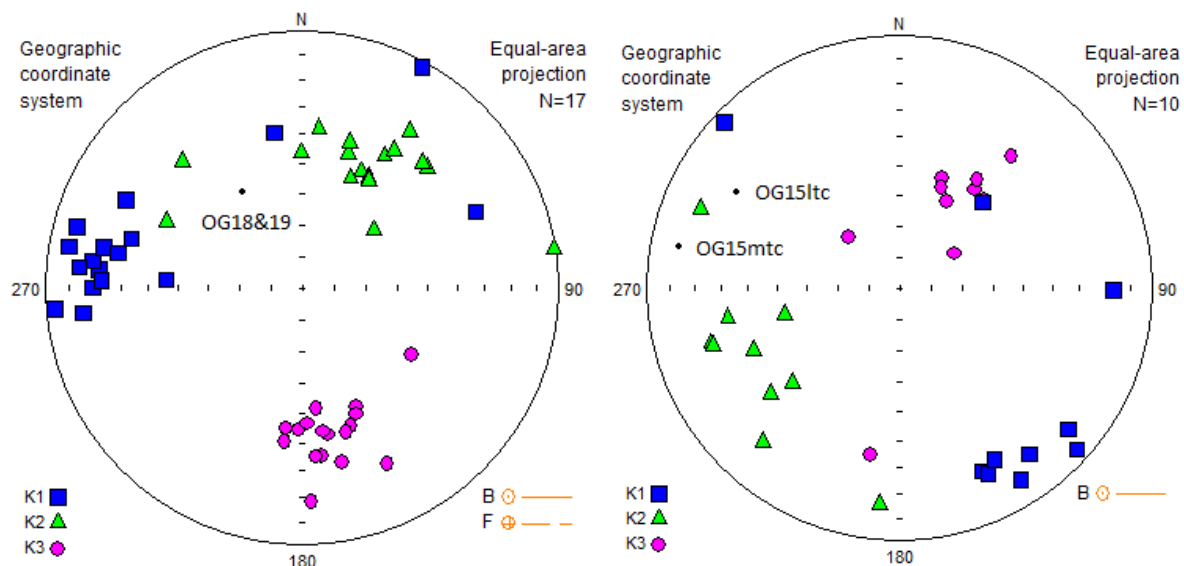
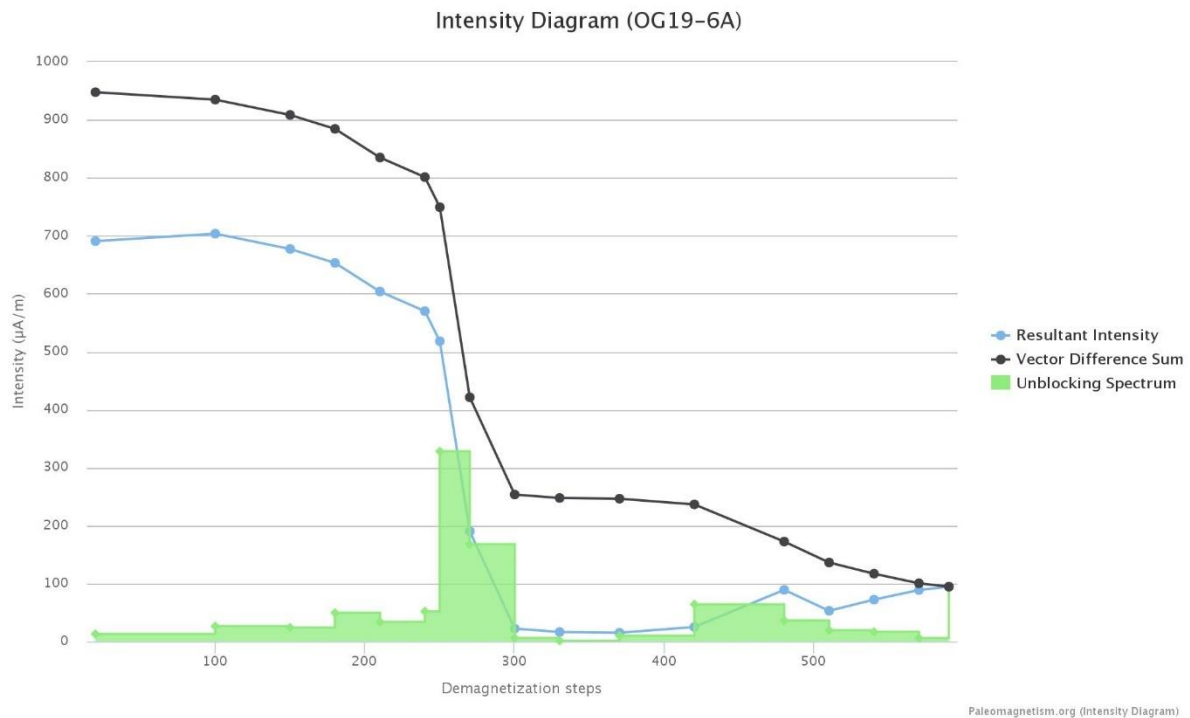


figure 22. The susceptibility axes of OG15 and OG18&19 and the relation to their magnetic direction. As can be witnessed in the graphs the results from demagnetization plot right between K1 and K2.

only 7 have discernable fabric (OG1, OG9, OG13, OG15, OG16, OG18 and OG19), the other sites are 'safe' in that regard. OG16 did not show a direction in the demagnetization runs and can thus be discarded. Of these 6 remaining sites 2 of them have magnetic directions on a plane between K1 and K2 (**figure 22**).



That means that for the above sites tampered magnetic directions are a real possibility. However, results from hysteresis loops and demagnetization patterns show that the magnetic minerals responsible for the magnetic signal belong to the (pseudo-)single domain category. Demagnetization patterns for a sample from OG19 (**figure 23**) show a sharp decline in intensity from 250 °C to 300 °C, characteristic of pyrrhotite of any grain size.



**figure 23. Intensity diagram for a sample from OG19, highlighting the drop in intensity at certain temperatures.**

The fact that single domain is the prevalent magnetic state, as well as the lack of fabric in most sites, indicate that influence of the magnetic direction is unlikely. Since the directions are not biased it is now important to discuss the findings in relation to other geological events occurring in Iberia and their possible effect and influence on the directional data.

## 5.2 vertical axis rotations

The Panticosa granite has directions (217.8°/40.5°,  $k=24.7$  and  $a_{95}=11.4$ ) concurring with those found by **Tait et al., 2000** (224°/51°,  $k=24.5$  and  $a_{95}=8.5^\circ$ ), which somewhat presents a conundrum. The Panticosa pluton is from the late Carbonifereous (**Duckering, 2013**) but does not reflect established late Carbonifereous/Early Permian directions (**Pastor-Galán et al., 2015**). Paleomagnetic data from the Viar basin and the Sotres & Cabranes formation in the Cantabrian orocline give values of 164.8°/4.5° and 146.2°/-9.2°, respectively (**Weil et al., 2010**). Similar results for Late Carboniferous/Early Permian rocks from the hypothesized Central Iberian bend give declinations between 90 and 154 degrees (**Pastor-Galán et al., 2015**). Since the direction does not coincide with the accepted directions for that time period the possibility of a vertical axis rotation (VAR) needs to be examined. The sampled location in the Panticosa granite is in close proximity to the Internal Sierras (IS), a region of the Pyrenees that has seen a significant amount of studies in the last decade regarding vertical axis rotations

**(Oliva-Urcia & Puyeo, 2007; Izquierdo-Llavall et al., 2015)**. Paleomagnetic analyses performed on samples from the Late Cretaceous belonging to the IS reveal two paleomagnetic components. The low-temperature component, dubbed the "B" component in the papers, demagnetizes between 200 °C and 400 °C and is considered to be post-folding. This component has a direction of  $192^\circ/-45^\circ$ ,  $k=22$  and  $a_{95}=9$ . Using an Eocene-Oligocene reference frame the component records a clockwise rotation of 18 to 26 degrees and is thought to be related to the stacking of basement thrust sheets, in particular the Gavarnie thrust **(Izquierdo-Llavall et al., 2015)**. Cores from the overlying Eocene flysch show the same "B" component **(Oliva-Urcia & Puyeo, 2007)**. The other component, termed the "C" component, reveals its signature at elevated temperatures up to 575 °C. This component has been acquired before basement thrusting based on conglomerate and fold tests **(Izquierdo-Llavall et al., 2015)**. For both components magnetite is the carrier of the magnetic signal. The B component is of a reversed polarity whereas the C component shows both normal and reversed directions. The directions garnered with this research for the Panticose granite, however, are of normal polarity and as such their signal cannot be explained with the VARs recorded in the IS. It is likely that this component, as well as the component found in **Tait et al., 2000**, records an as of now unknown magnetic overprint rather than revealing a primary magnetization from the Devonian. Some tectonic movement is likely to be involved too.

The same B component has been identified in several Permian and Triassic red beds in the Bielsa area **(Oliva-Urcia et al., 2012; Izquierdo-Llavall et al., 2015)**. This time the magnetic carrier consists of hematite and as a result the unblocking temperature exceeds 500 °C. An additional direction termed 'Cb' gives  $355^\circ/06^\circ$ ;  $k=18$  and  $\alpha_{95}=13$ , with its normal and reversed direction being nearly opposite revealing its primary character **(Oliva-Urcia et al., 2012)**. Several other smaller components have been found in neighboring areas, with 'Ch' and 'Cc' components from the Somport and Anayet region giving  $158^\circ/2^\circ$ ,  $k=28$  and  $\alpha_{95}=4$  and  $195^\circ/-10^\circ$ ,  $k=16$  and  $\alpha_{95}=22$ , respectively, **(Oliva-Urcia et al., 2012)**, with the 'Ch' component being recognized from an earlier study **(Cogne, 1987)**. Both these directions are considered to be primary **(Oliva-Urcia et al., 2012)**. None of the directions obtained from locations nearby with this research, namely OG9 and OG10, can be linked to the aforementioned directions in the literature. Since OG9 and OG10 contain pyrrhotite there is no doubt about the remagnetized character of these sites. OG9, with its high k-value, most likely represents a combination of two or more vectors that combine to form the observed direction.

Further to the east, in the Castejón-Laspaúles basin, late Carboniferous magmatic rocks document a component that has a direction of  $193^\circ/-05^\circ$ ,  $k=0.9$  and  $\alpha_{95}=18$  **(Izquierdo-Llavall et al., 2014)**. This component is thought to record a  $\pm 37^\circ$  clockwise rotation when taking the Stephanian stage as a reference frame ( $336^\circ/-06^\circ$  and  $\alpha_{95} = 12.5^\circ$ ) **(Van der Voo, 1969; Izquierdo-Llavall et al., 2014)**. Similar directions have been found in Triassic red beds that overlie the Carboniferous rocks **(Izquierdo-Llavall et al., 2012)**. It is therefore likely that the rotation occurred during the Alpine orogeny **(Izquierdo-Llavall et al., 2014)**. There is no reason to assume that the Devonian cores taken in this valley (OG11, OG12 and OG13) in this research have similarly recorded clockwise rotation. OG11 is too scarce and its directions ( $281.3^\circ/34.6^\circ$ ,  $k=4.3$  and  $a_{95}=42.0$ ) do not correspond with those established in the literature. There is no way to link this direction with a  $\pm 35^\circ$  clockwise rotation with an unknown Devonian reference frame. OG13 records the counterclockwise rotation of Iberia in the Aptian instead. Both of the directions recorded by OG12 ( $28.7^\circ/45.6^\circ$ ,  $k=10.7$  and  $a_{95}=19.4$  and  $125.4^\circ/21.9^\circ$ ,  $k=26.0$  and  $a_{95}=9.7$ ) cannot be explained away by a mere clockwise rotation in the Cenozoic.

### 5.3 Cretaceous overprint?

Most of the samples containing magnetite are clustered in the upper left quadrant. It concerns the sites OG4, OG7, OG13 and OG15. Other sites in that cluster include OG2, OG17 and OG18&19. These sites have pyrrhotite as the carrier of the magnetic signal. Figure 21 shows that pyrrhotite is also present in the sites in which the demagnetization is brought about by magnetite. This cluster is shown in figure 11 and has a combined declination and inclination of  $323.7^\circ/35.9^\circ$ , respectively (**figure 24**). The presence of pyrrhotite as well as the negative fold tests obtained in OG13 and OG19 is a clear indicator of a magnetic overprint. These sites are taken from all over the Pyrenees, with OG4 and OG18 being 150 km apart. This vast distance between these sites point towards a regional-scale event responsible for the clustering directions, rather than local phenomena determining said directions. This is especially evident when considering that several sites have garnered a positive common true mean direction (CTMD) (**figure 25**). This figure shows that for every site combination classified with a C a common direction has been obtained i.e. their directions are so similar that a common mechanism might be behind their result. That means that the components in OG4 and OG17 have similar histories, as well as OG13ltc & OG18&19 and OG15 & OG7.

### alleged Cretaceous directions

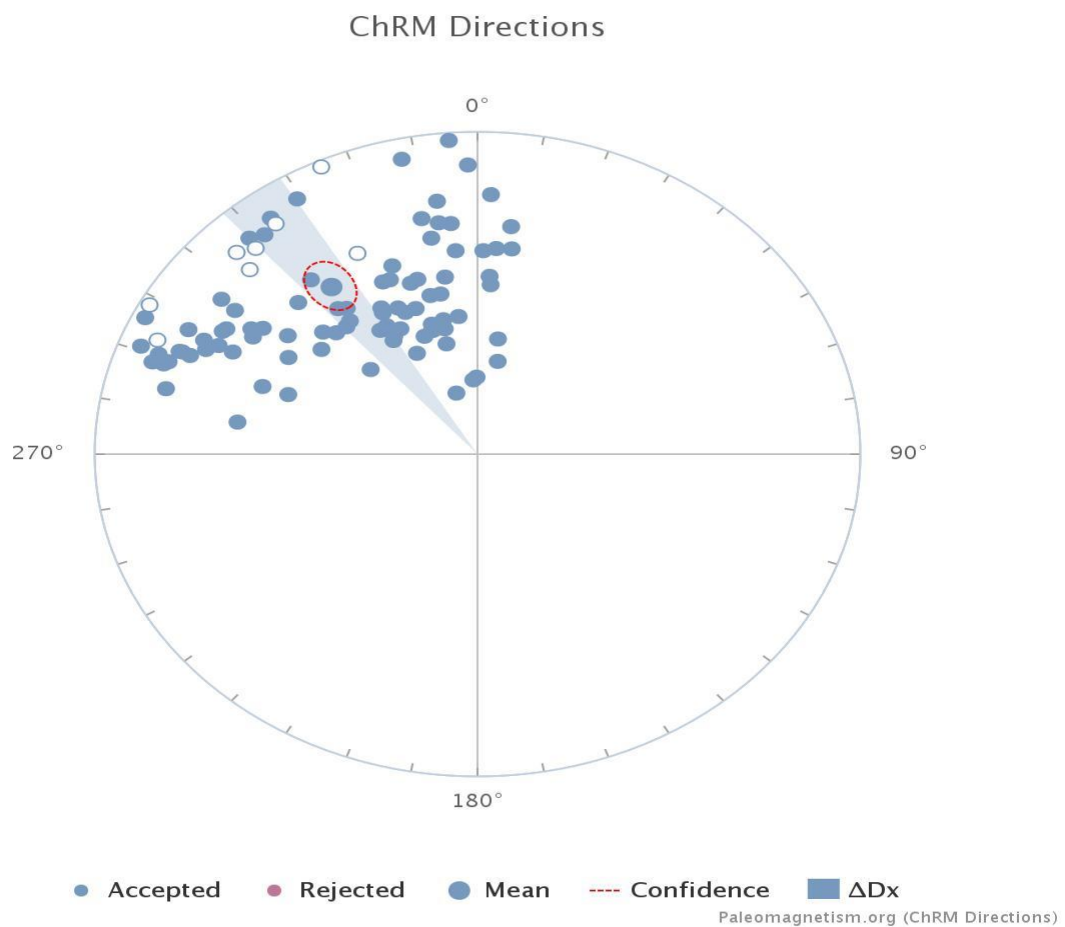


**figure 24:** This figure shows the mean directions of the sites OG2, OG4ltc&mtc, OG7, OG13ltc, OG15ltc&mtc, OG17 and OG18&19. The combined direction is  $323.7^\circ/35.9^\circ$ .

The direction obtained by OG13mtc falls outside the scope of rotation for Iberia in the Aptian with direction of 257.9°/25.2°. However, it is likely to be a relic of the other component found in OG13 and as such can be categorized with the low temperature component found in OG13.

## Common True Mean Directions

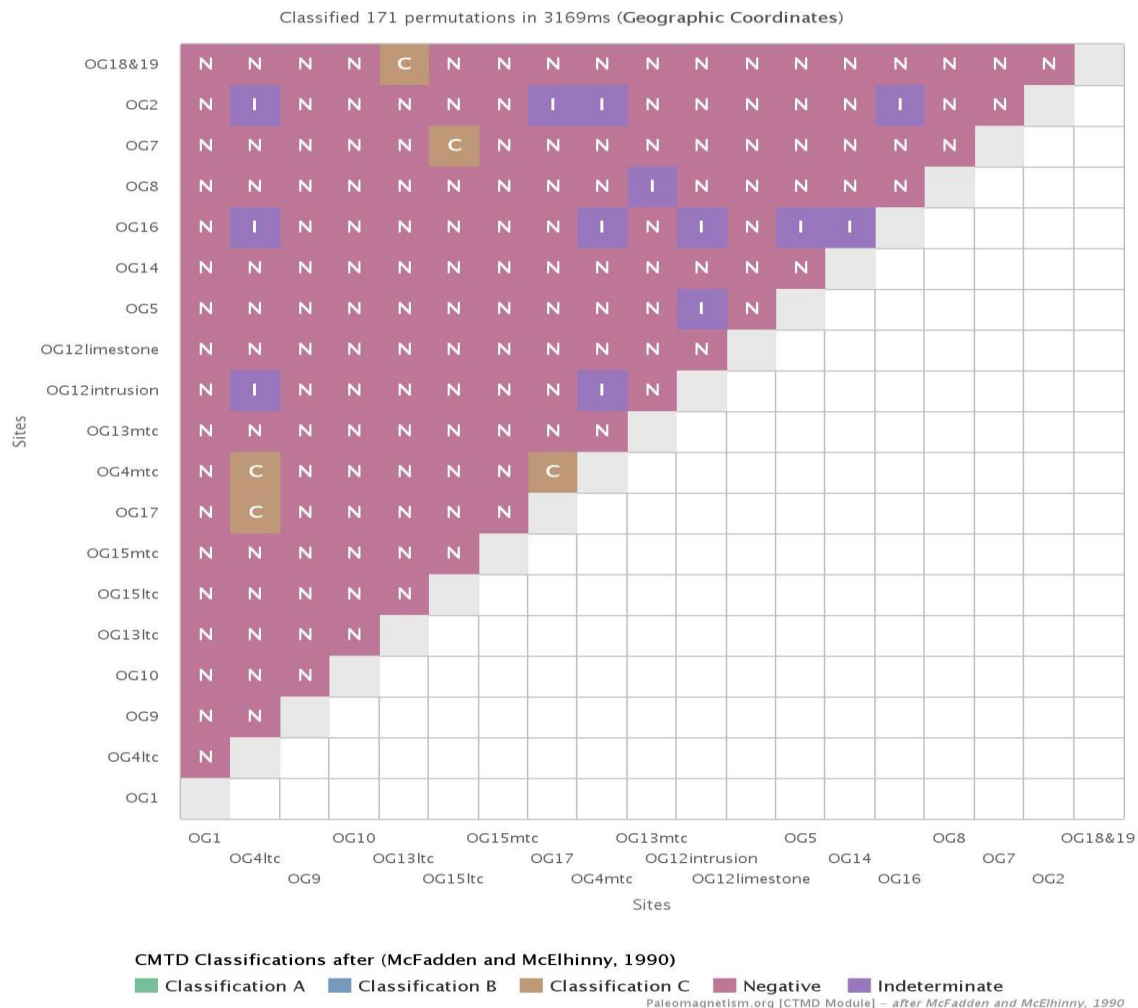


**figure 25: This figure shows the common true mean directions of the plotted sites. A Classification of C entails that their directions are compatible, i.e. the same event is responsible for the magnetization. This figure uses geographical coordinates.**

The obtained direction is strikingly similar to the 35° counterclockwise rotation of Iberia in the Cretaceous (**Van der Voo, 1969; Gong et al., 2008; 2009c**) related to the opening of the Bay of Biscay. To see whether the direction in figure 20 is compatible with this rotation its location, inclination and declination can be compared with that of Iberia in the Cretaceous. Latest research confines the rotation to the Aptian stage (125-113 Ma) (**Gong et al., 2009c**). Taking a modern-day latitude of around 42° and using **Torsvik et al., 2012's** apparent polar wander path (APWP) for Iberia during said timeline in Koymans et al., 2016 [www.paleomagnetism.org](http://www.paleomagnetism.org) program this can be investigated. The results are shown in figure 26. Figure 26a shows that for the declination the alleged Cretaceous directions are in good accordance with the polar wander path for Iberia during the Aptian. The data point falls well within Torsvik's reference model in blue. A declination of -36.5° has been obtained. For the inclination (**figure 26b**) the values are

too shallow even when considering its error bars. According to **Torsvik et al., 2012** the inclination should hover around 48° for the Aptian leading to a paleolatitude of about 30°. The inclination in this research amounts to 36° with a paleolatitude of 19°. The mismatch in the inclination, as well as the lack of geomagnetic reversals in the Aptian necessary to account for the reverse polarities in OG4mtc and OG18&19 argue against an Aptian remagnetization. However, the presence of pyrrhotite, negative fault tests, the communality of directions and the similarity in the declination to **Torsvik et al., 2012** leaves little doubt that these sites have experienced remagnetization, most likely during the Cretaceous.

One of the possible reconstructions is shown in figure 27 using the age data provided in table 14. While not a perfect fit it is clear that the sites plot around the established values for declination and inclination for Iberia during the Cretaceous. When taken the error bars into

site	age in Ma (age range)
OG2	105 (95-115)
OG7	135 (125-145)
OG13ltc	140 (130-150)
OG15ltc	140 (130-150)
OG15mtc	140 (125-50)
OG17	116 (106-125)
OG18&19	124 (113-135)

account there is considerable overlap between these sites and the declination with only OG15mtc being an outlier. The inclination is considerably more difficult to reconcile with Torsvik's directions for the Cretaceous, being about 15° too shallow for most sites. Some of these sites (OG2, OG7 and OG15ltc&mtc) fit better when considering a Triassic (252.17 to 201.3 Ma) remagnetization though the fit for declination worsens.

**table 5: The sites and age data for figure 22.**

Furthermore, there is no known large-scale remagnetization event in the Triassic that might explain these directions. The opening of the Bay of Biscay in the Cretaceous, on the other hand, is well documented and an obvious candidate, and, based on figure 23, the more likely scenario.

Apart from the sites that record the counterclockwise rotation in the Cretaceous the directions obtained in this research do not correspond with any known direction for Iberia. The presence of a Carboniferous granite with similar directions to the component found in **Tait et al., 2000** might indicate a similar remagnetization event for both components, rather than a primary signal from the Devonian. Efforts to link this direction with vertical axis rotations in the nearby Internal Sierras have proven futile. The lack of directions coinciding with a possible primary Devonian magnetization found by **Tait et al., 2000** does not support the hypothesis of a drifting Iberia, either as part of Armorica or as a separate entity. Combined with data from paleontology (**Robardet, 2003**), geochronology (**Díez-Fernández et al., 2010**) and geochemistry (**Pastor-Galán et al., 2013**), which all argue against the rifting of Iberia, it is more likely that Iberia remained part of Gondwana till the Variscan orogeny.

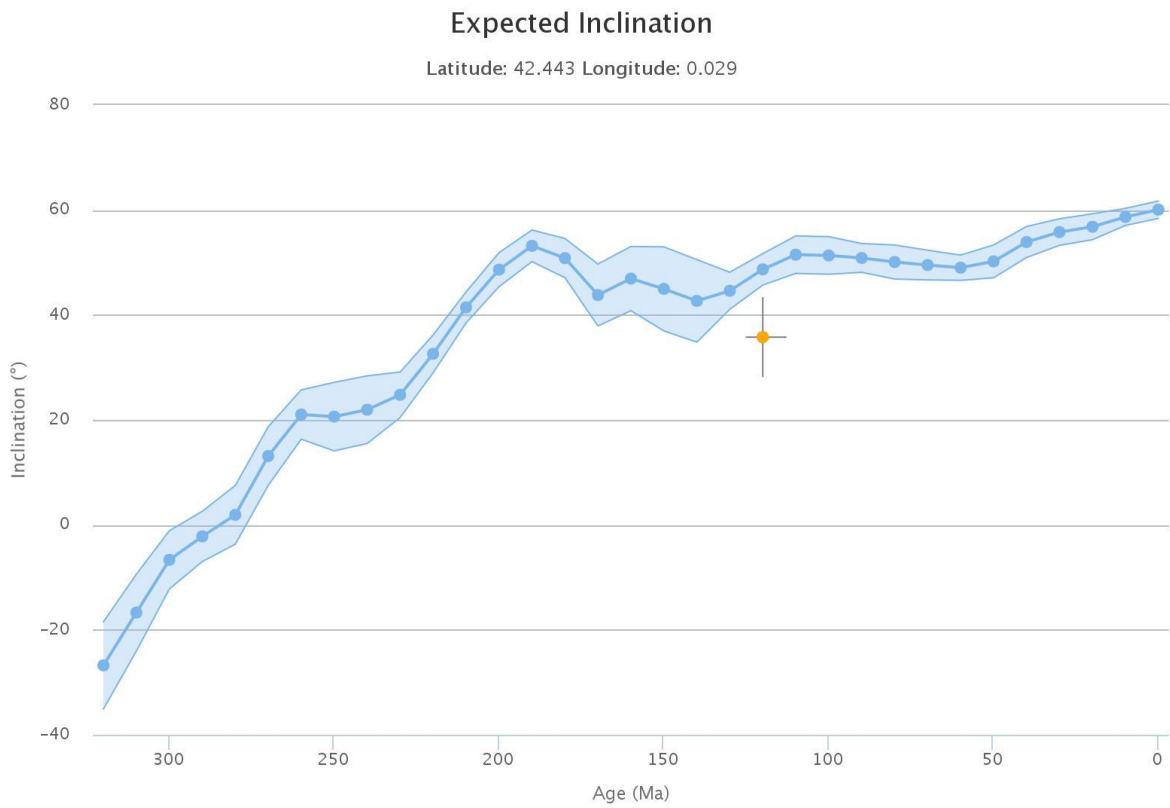
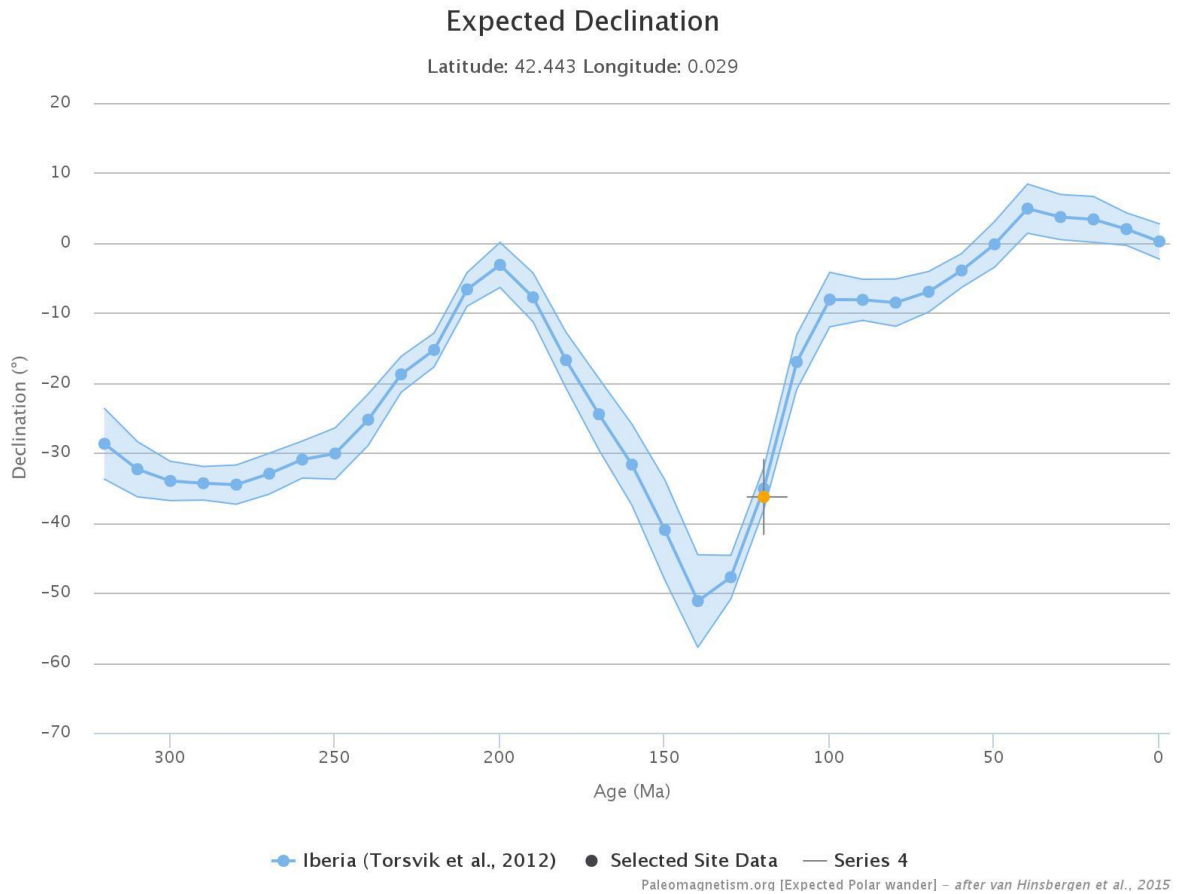


**figure 26. Apparent polar wander path for Iberia in the Mesozoic and Cenozoic according to Torsvik et al., 2012. 26a: Expected declination for Iberia. The data point represents the combined direction of OG2, OG4, OG7, OG13, OG15, OG17 and OG18&19. 26b: Expected inclination for Iberia. The data point represents the combined direction of OG2, OG4, OG7, OG13, OG15, OG17 and OG18&19.**

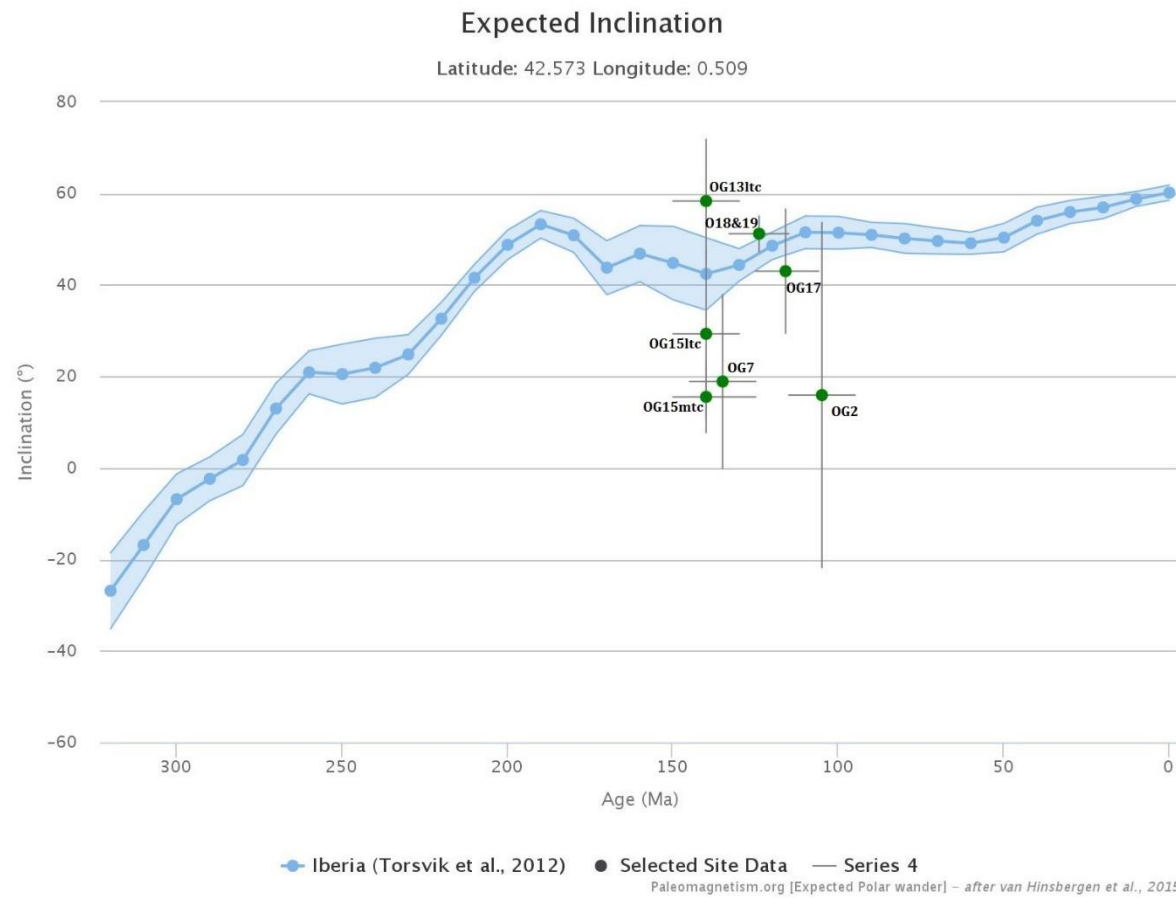
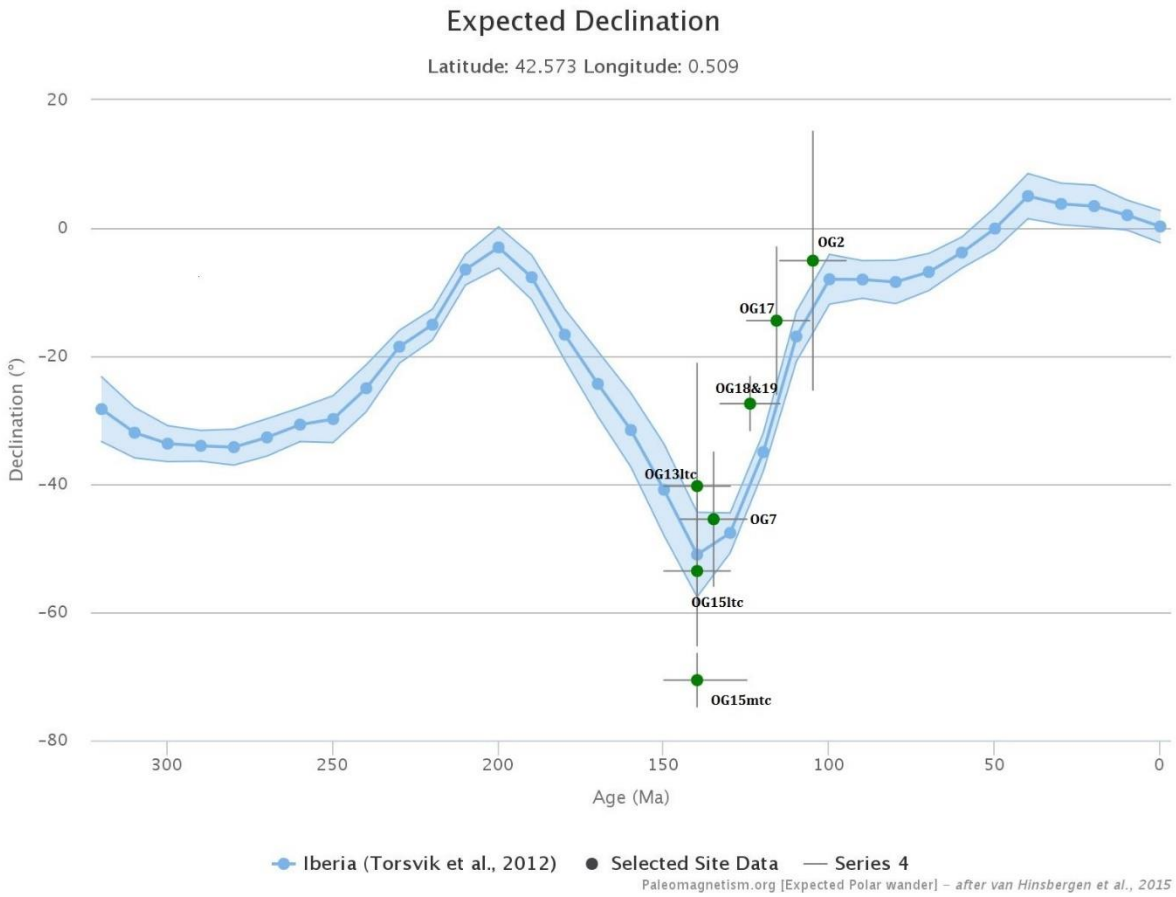


**figure 27. Declination and inclination for the listed sites, compared to Torsvik et al., 2012 magnetic directions.**

## 6. conclusion

Paleomagnetic analyses of 18 Devonian limestones and 1 Permian granite from the Pyrenees reveal both secondary magnetite and secondary pyrrhotite as the carrier of the magnetic signal. 7 out of 19 sampled sites record the counterclockwise rotation of Iberia during the Cretaceous, with a combined direction of  $326.9^\circ/38.1^\circ$ ,  $k=7.7$  and  $a_{95}=5.5^\circ$ . Negative fault tests (OG13 and OG19) and the fact that pyrrhotite is dominant in the results counter the idea of a primary Devonian direction ( $224^\circ/51^\circ$ ,  $k=24.5$  and  $a_{95}=8.5^\circ$ ) found in (Tait et al., 2000). Furthermore, a similar component ( $217.8^\circ/40.5^\circ$ ,  $k=24.7$  and  $a_{95}=11.4$ ) from the Permian granite essentially indicates a similar remagnetization event for both components. Attempts to link these results, as well as other obtained directions, to vertical axis rotations in the Pyrenees have proven futile. Based on these results it is unlikely that a Devonian direction has ever been recorded in the Pyrenees, and as a result the foundation for a drifting Iberia crumbles. When taking into account criticism from the fields of paleontology, geochronology and geochemistry it is far more likely for Iberia to have remained attached to Gondwana rather than becoming a drifting microcontinent in the Middle Paleozoic.

## 7. references

- Aben, F. M., M. J. Dekkers, R. R. Bakker, D. J. J. van Hinsbergen, W. J. Zachariasse, G. W. Tate, N. McQuarrie, R. Harris, and B. Duffy. 2014. Untangling inconsistent magnetic polarity records through an integrated rock magnetic analysis: A case study on Neogene sections in East Timor, *Geochem. Geophys. Geosyst.*, 15, 2531–2554, doi:10.1002/2014GC005294
- Arenas, R., Martínez Catalán, J.R., Sánchez Martínez, S., Fernández-Suárez, J., Andonaegui, P., Pearce, J.A., Corfu, F., 2007. The Vila de Cruces ophiolite: a remnant of the Early Rheic Ocean in the Variscan Suture of Galicia (Northwest Iberian Massif). *Journal of Geology* 115, 129–148.
- Bea, F., Montero, P., Talavera, C., Zinger, T., 2006. A revised Ordovician age for the oldest magmatism of Central Iberia U-Pb ionmicroprobe and LA-ICPMS dating of the Miranda do Douro orthogneiss. *Geology Acta* 4, 395–401.
- Cogné, J.P., 1987. Paleomagnetic direction obtained by strain removal of Pyrenean Permian redbeds at the “Col du Somport” (France). *Earth and Planetary Science Letters* 85, 162–172.
- Dallmeyer, R.D., Martínez Catalán, J.R., Arenas, R., Gil Ibarra, J.I., Gutiérrez-Alonso, G., Dubey, A.K., 2014. *Understanding an Orogenic Belt*, chapter 2.
- Dekkers, M. J., 2012, End-member modelling as an aid to diagnose remagnetization: A brief review, *Geol. Soc. Spec. Publ.*, 371, 253–269.
- Farias, P., Bastida, F., Aller, J., 1997. Diachronous Variscan tectonothermal activity in the NW Iberian Massif: evidence from  $40\text{Ar}/39\text{Ar}$  dating of regional fabrics. *Tectonophysics* 277, 307–337.
- de Jong, K., 1990. Alpine tectonics and rotation pole evolution of Iberia. *Tectonophysics* 184, 279 – 296.
- Decarlis, A., Dallagiovanna, G., Lualdi, A., Maino, M., Seno, S., 2013. Stratigraphic evolution in the Ligurian Alps between Variscan heritages and the Alpine Tethys opening: a review. *Earth Sci. Rev.* 125, 43–68.
- Díez -Fernández, R., Catalán, J.R.M., Gerdes, A., Abati, J., Arenas, R., Fernández-Suárez, J., 2010. U–Pb ages of detrital zircons from the Basal allochthonous units of NW Iberia: provenance and paleoposition on the northern margin of Gondwana during the Neoproterozoic and Paleozoic. *Gondwana Research* 18, 385–399.



- Díez Fernández, R., Castiñeiras, P., Gómez Barreiro, J., 2012.** Age constraints on Lower Paleozoic convection system: magmatic events in the NW Iberian Gondwana margin. *Gondwana Research* 21, 1066–1079.
- Druguet, E., Castro, A., Chichorro, M., Pereira, M.F., Fernández, C., 2014.** Zircon geochronology of intrusive rocks from Cap de Creus, Eastern Pyrenees. *Geol. Mag.* 151, 1095–1114
- J. Duckering, 2013.** Orogeny, Plutonism and Metamorphism of the Panticosa Area, Spanish Pyrenees; Structure and Evolution. *Earth & Environment* 9, pp 160-212
- Gong, Z., Langereis, C.G., Mullender, T.A.T., 2008.** The rotation of Iberia during the Aptian and the opening of the Bay of Biscay. *Earth and Planetary Science Letters* 273, 80–93
- Gong, Z., van Hinsbergen, D.J.J., Vissers, R.L.M., Dekkers, M.J., 2009a.** Early Cretaceous synrotational extension in the Organyà basin—New constraints on the palinspastic position of Iberia during its rotation. *Tectonophysics* 473, 312–323
- Gong, Z., Dekkers, M. J., Heslop, D. & Mullender, T. A. T. 2009b.** End-member modelling of isothermal remanent magnetization (IRM) acquisition curves: a novel approach to diagnose remagnetization. *Geophysical Journal International*, 178, 693– 701
- Gong, Z., Van Hinsbergen, D.J.J., Dekkers, M.J., 2009c.** Diachronous pervasive remagnetization in northern Iberian basins during Cretaceous rotation and extension, *Earth Planet. Sci. Lett.*, 284, 292-301
- Gretter, N., Ronchi, A., López-Gómez, J., Arche, A., De la Horra R., Barrenechea, J.F., Lago, M., 2015.** The Late Palaeozoic-Early Mesozoic from the Catalan Pyrenees (Spain): 60 Myr of environmental evolution in the frame of the western peri-Tethyan palaeogeography. *Earth-Sci. Rew.* 150, 679–708.
- Gutiérrez-Alonso, G., Fernández-Suárez, J., Gutiérrez-Marco, J.C., Corfu, F., Murphy, J.B., Suárez, M., 2007.** U–Pb depositional age for the upper Barrios Formation (Armorican Quartzite facies) in the Cantabrian zone of Iberia: implications for stratigraphic correlation and paleogeography. *The Evolution of the Rheic Ocean: From Avalonian–Cadomian Active Margin to Alleghenian–Variscan Collision*. In: Linnemann, U., Nance, R.D., Kraft, P., Zulauf, G. (Eds.), *Geological Society of America Special Paper*, vol. 423, pp. 287–296.
- Heslop, D. & Dillon, M., 2007.** Unmixing magnetic remanence curves without a priori knowledge. *Geophysical Journal International*, 170(2), pp.556–566.
- Heslop, D., Dekkers, M.J., Kruiver, P.P. and Van Oorschot, I.H.M. 2002.** Analysis of isothermal remanent magnetisation acquisition curves using the expectation-maximisation algorithm. *Geophys. J. Int.*, 148, 58-64.
- Heslop, D., McIntosh, G. & Dekkers, M.J., 2004.** Using time- and temperature-dependent Preisach models to investigate the limitations of modelling isothermal remanent magnetization acquisition curves with cumulative log Gaussian functions, *Geophys. J. Int.*, 157, 55–63.
- Hrouda, F. & Jelinek, V., 1990.** Resolution of ferrimagnetic and paramagnetic anisotropies in rocks, using combined low-field and high-field measurements. *Geophysical Journal International*, 103(1), pp.75–84.
- Izquierdo-Llavall, E., Casas, A. M., Oliva-Urcia, B. & Scholger, R. 2012.** Are there vertical axis rotations associated with folded thrusts? Insights from a paleomagnetic study in the Noguera Zone (Central Pyrenees). *Contributions to Geophysics and Geodesy* 42, Special Issue, 76–7.
- Izquierdo-Llavall, E., Sainz, A. C., Oliva-Urcia, B., Burmester, R., Pueyo, E. L., & Housen, B. 2015.** Multi-episodic remagnetization related to deformation in the Pyrenean Internal Sierras. *Geophysical Journal International*, 201(2), 891-914.
- Jammes, S., Lavier, L., and Manatschal, G., 2010.** Extreme crustal thinning in the Bay of Biscay and the Western Pyrenees: From observations to modelling: *Geochemistry Geophysics Geosystems*, v. 11, Q10016, doi:10.1029/2010GC003218.
- Kirschvink, J. L. 1980.** The least-squares line and plane and the analysis of paleomagnetic data. *Geophys. J. Roy. Astron. Soc.*, 62, 699–718.

- Koymans, M.R., Langereis, C.G., Pastor-Galan, D., and van Hinsbergen, D.J.J., 2016** Paleomagnetism.org: An online multi-platform open source environment for paleomagnetic data analysis, *Computers and Geosciences*, Volume 93, Pages 127–137
- Kruiver, P.P., Dekkers, M.J. & Heslop, D., 2001.** Quantification of magnetic coercivity components by the analysis of acquisition curves of isothermal remanent magnetisation. *Earth and Planetary Science Letters*, 189(3-4), pp.269–276.
- Linnemann, U., McNaughton, N.J., Romer, R.L., Gehmlich, M., Drost, K., Tonk, C., 2004.** West African provenance for Saxo-Thuringia (Bohemian Massif): did Armorica ever leave pre-Pangean Gondwana? U/Pb-SHRIMP zircon evidence and the Nd-isotopic record. *International Journal of Earth Sciences* 93, 683–705.
- Linnemann, U., Gerdes, A., Drost, K., Buschmann, B., 2007.** The continuum between Cadomian orogenesis and opening of the Rheic Ocean: constraints from LA-ICP-MS U–Pb zircon dating and analysis of plate-tectonic setting (Saxo-Thuringian zone, northeastern Bohemian Massif, Germany). *Geological Society of America Special Papers* 423, 61–96.
- Martínez-Peña, M.B. & Casas-Sainz, A.M., 2003.** Cretaceous-Tertiary tectonic inversion of the Cotiella Basin (southern Pyrenees, Spain), *Int. J. Earth Sci.*, **92**, 99–113.
- Martínez Catalán, J.R., Arenas, R., Abati, J., Sánchez Martínez, Sonia, Díaz García, Florentino, Fernández Suárez, Javier, González Cuadra, Pablo, Castiñeiras, Pedro, Gómez Barreiro, Juan, Díez Montes, Alejandro, González Clavijo, Emilio, Rubio, Francisco J., Andonaegui Pascual, Pilar, Jeffries, Teresa E., Alcock, James E., Díez Fernández, Rubén, López Carmona, A., 2009.** A rootless suture and the loss of the roots of a mountain chain: the Variscan belt of NW Iberia. *Comptes Rendus Geosciences* 341, 114–126.
- Martínez Catalán, J.R., 2012.** The Central Iberian arc, an orocline centered in the Iberian Massif and some implications for the Variscan belt. *International Journal of Earth Sciences* 1–16.
- Morzadec, P., Paris, F., Plusquellec, Y., Racheboeuf, P., Weyant, M., 1988.** Devonian stratigraphy and palaeogeography of the Armorican Massif (NW France). In: McMillan, N.J., Embry, A.F., Gass, D.J. (Eds.), *Devonian of the World*. Can. Soc. Petrol. Geol. Mem. 14, pp. 401–420.
- T.A.T. Mullender, T. Frederichs, C. Hilgenfeldt, K. Fabian, M.J. Dekkers. 2005:** Fully automated demagnetization and measurement of NRM, ARM and IRM on '2G' SQUID magnetometer
- Mullender, T. a. T., van Velzen, a. J. & Dekkers, M.J., 1993.** Continuous drift correction and separate identification of ferrimagnetic and paramagnetic contributions in thermomagnetic runs. *Geophysical Journal International*, 114, pp.663–672.
- Murphy, J.B., Gutierrez-Alonso, G., Nance, R.D., Fernandez-Suarez, J., Keppie, J.D., Quesada, C., Strachan, R.A., Dostal, J., 2006.** Origin of the Rheic Ocean: rifting along a Neoproterozoic suture? *Geology* 34, 325–328.
- Murphy, J.B., Gutiérrez-Alonso, G., Fernández-Suárez, J., Braid, J.A., 2008.** Probing crustal and mantle lithosphere origin through Ordovician volcanic rocks along the Iberian passive margin of Gondwana. *Tectonophysics* 461 (1–4), 166–180.
- Nance, R.D., Gutiérrez-Alonso, G., Keppie, J.D., Linnemann, U., Murphy, J.B., Quesada, C., Strachan, R.A., Woodcock, N.H., 2010.** Evolution of the Rheic Ocean. *Gondwana Research* 17, 194–222.
- Oliva-Urcia, B. & Pueyo, E.L., 2007.** Rotational basement kinematics deduced from remagnetized cover rocks (Internal Sierras, southwestern Pyrenees), *Tectonics*, 26, TC4014, doi:10.1029/2006TC001955.
- Oliva-Urcia, B., Pueyo, E.L., Larrasoña, J.C., Casas, A.M., Román-Berdiel, T., Van der Voo, R. & Scholger, R., 2012** New and revisited paleomagnetic data from Permian-Triassic red beds: two kinematic domains in the west central Pyrenees, *Tectonophysics*, 522–523, 158–175.

- Pastor-Galán, D., Gutiérrez-Alonso, G., and Weil, A.B., 2011.** Orocline timing through joint analysis: Insights from the Ibero-Armorican Arc: *Tectonophysics*, v. 507, p. 31–46, doi:10.1016/j.tecto.2011.05.005.
- Pastor-Galán, D., Gutiérrez-Alonso, G., Fernández Suárez, J., Murphy, J.B., and Nieto, F., 2013,** Tectonic evolution of NW Iberia during the Paleozoic inferred from the geochemical record of detrital rocks in the Cantabrian Zone: *Lithos*, v. 182–183, p. 211–228, doi:10.1016/j.lithos.2013.09.007.
- Pastor-Galán, D., Groenewegen, T., Brouwer, D., Krijgsman, W., Dekkers, M.J., 2015.** One or two oroclinal in the Variscan orogen of Iberia? Implications for Pangea amalgamation. *Geology* 43, 527–530. <http://dx.doi.org/10.1130/G36701.1>.
- Pereira, M.F., Linnemann, U., Hofmann, M., Chichorro, M., Solá, A.R., Medina, J., Silva, J.B., 2012.** The provenance of Late Ediacaran and Early Ordovician siliciclastic rocks in the Southwest Central Iberian Zone: constraints from detrital zircon data on northern Gondwana margin evolution during the late Neoproterozoic. *Precambrian Research* 192–195, 166–189.
- Rey, P., Vanderhaeghe, O., Teyssier, C., 2001.** Gravitational collapse of the continental crust: regimes and modes. *Tectonophysics* 342, 435–449.
- Robardet, M., Paris, F., Racheboeuf, P.R., 1990.** Palaeogeographic evolution of southwestern Europe during Early Palaeozoic times. In: Mc Kerrow, W.S., Scotese, C.R. (Eds.), *Palaeozoic Palaeogeography and Biogeography*. Geol. Soc. London Mem. 12, 411–419.
- Robardet, M., 2002.** Alternative approach to the Variscan Belt in southwestern Europe: preorogenic paleobiogeographical constraints. In: Martínez Catalán, J. R., Hatcher, R. D. Jr., Arenas, R. & Díaz García, F. (eds) *Variscan–Appalachian Dynamics: The Building of the Late Paleozoic Basement*. Geological Society of America Special Papers, 364, 1–15.
- Robardet, M., 2003.** The Armorica ‘microplate’: factor fiction? Critical review of the concept and contradictory palaeobiogeographical data. *Palaeogeography, Palaeoclimatology, Palaeoecology* 195, 125–148 (24).
- Robertson, D.J. & France, D.E., 1994.** Discrimination of remanence-carrying minerals in mixtures, using isothermal remanent magnetisation acquisition curves. *Physics of the Earth and Planetary Interiors*, 82(3-4), pp.223–234.
- Rosenbaum, G., Lister, G.S., and Duboz, C., 2002.** Relative motions of Africa, Iberia and Europe during Alpine orogeny: *Tectonophysics*, v. 359, p. 117–129, doi:10.1016/S0040-1951(02)00442-0
- Rushlow, C. R., J. B. Barnes, T. A. Ehlers, and J. Vergés., 2013.** Exhumation of the Southern Pyrenean fold-thrust belt (Spain) from orogenic growth to decay, *Tectonics*, 32, 1–18, doi:10.1002/tect.20030
- Sagnotti L., Faccenna C., Funicello R., Mattei, M., 1994.** Magnetic fabric and structural setting of Plio-Pleistocene clayey units in an extensional regime: the Tyrrhenian margin of central Italy. *J Struct Geol* 16:1243–1257
- Santana, V., Vegas, N., Pinotti, L. & Tubia, J. M., 2006.** Fábrica magnética de diques doleríticos del Plutón de Panticosa (Zona Axial, Pirineos).. *Geogaceta*, Issue 39, pp. 19-22.
- Schönlaub, H.P., 1997.** Guidebook. IGCP Project 421, North Gondwanan Mid-Palaeozoic Biodynamics Vienna 1997. *Berichte der Geologischen Bundesanstalt, Wien*, 40, 134 pp.
- Sibuet, J.C., Srivastava, S.P., Spakman, W., 2004.** Pyrenean orogeny and plate kinematics. *Journal of Geophysical Research* 109 (B8104), B08104. doi:10.1029/2003JB002514.
- Sinclair, H. D., M. Gibson, M. Naylor, and R. G. Morris., 2005.** Asymmetric growth of the Pyrenees revealed through measurement and modeling of orogenic fluxes, *Am. J. Sci.*, 305, 369–406.
- Soula, J.C., Lamouroux, C., Viallard, P., Bessiere, G., Debat, P., Ferret, B., 1986.** The mylonite zones in the Pyrenees and their place in the Alpine tectonic evolution. *Tectonophysics* 129, 115 – 147.
- Stampfli, G.M., Borel, G.D., 2002.** A plate tectonic model for the Paleozoic and Mesozoic constrained by dynamic plate boundaries and restored synthetic oceanic isochrons. *Earth and Planetary Science Letters* 196, 17–33.
- Stampfli, G.M., von Raumer, J., Wilhem, C., 2011.** The distribution of Gondwana derived

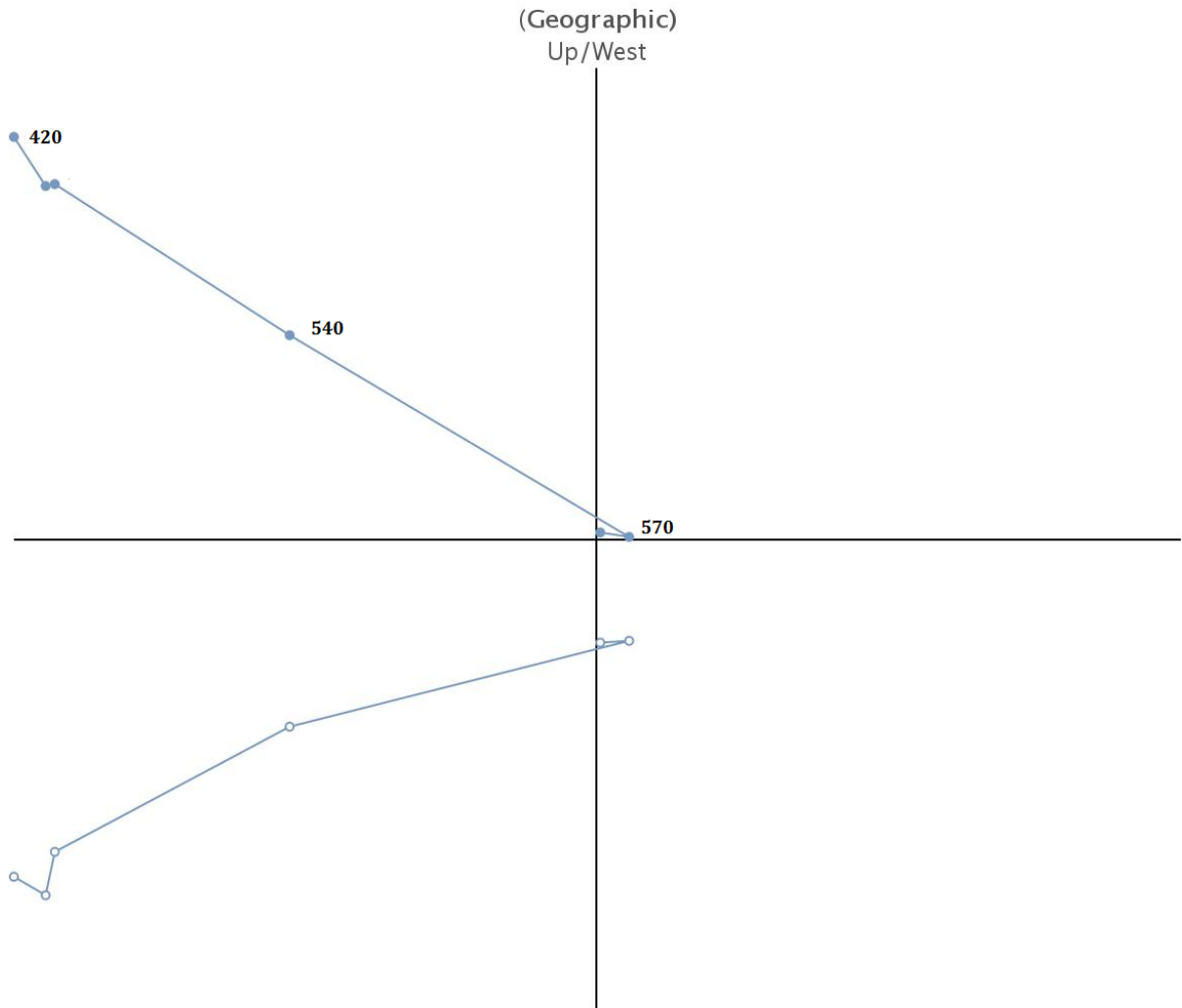
- terrane in the early Paleozoic. In: Gutiérrez-Marco, J.C., Rábano, I., García-Bellido, D. (Eds.), *The Ordovician of the World: Cuadernos del Museo Geominero*, vol. 14. Instituto Geológico y Minero de España, Madrid, pp. 567–574.
- Stampfli, G.M., Hochard, C., Verard, C., Wilhem, C. & Von Raumer, J. 2013.** The formation of Pangea. *Tectonophysics*, 593, 1–19.
- Tait, J., Bachtadse, V., Soffel, H., 1994.** Silurian paleogeography of Armorica: New paleomagnetic data from central Bohemia. *J. Geoph. Res.* 99, 2897–2907.
- Tait, J.A., 1999.** New Early Devonian paleomagnetic data from NW France: paleogeography and implications for the Armorican microplate hypothesis. *Journal of Geophysical Research* 104, 2831–2839.
- Tait, J.A., Bachtadse, V., Dinarés-Turell, 2000.** Paleomagnetism of Siluro-Devonian sequences, NE Spain: *Journal of Geophysical Research*, v. 105, p. 23,595–23,603, doi: 10.1029/2000JB900111
- Tauxe, L., 2005.** *Essentials of Paleomagnetism*
- Torsvik, T.H., Cocks, L.R.M., 2002.** Earth geography from 500 to 400 million years ago: a faunal and palaeomagnetic review. *Journal of the Geological Society, London*, 159, 631–644.
- Torsvik, T.H., Cocks, L.R.M., 2004.** Earth geography from 400 to 250 Ma: A palaeomagnetic, faunal and facies review. *Journal of the Geological Society* 161: 555–572.
- Torsvik, T.H., Cocks, L.R.M., 2011.** The Palaeozoic palaeogeography of central Gondwana. In: Van Hinsbergen, D.J.J., Buiter, S.J.H., Torsvik, T.H., Gaina, C., Webb, S.J. (Eds.), *The Formation and Evolution of Africa: A Synopsis of 3.8 Ga of Earth History: Geological Society, London, Special Publications*, 357, pp. 137–166.
- Torsvik, T.H., Van der Voo, R., Preeden, U., Mac Niocaill, C., Steinberger, B., Doubrovine, P.V., van Hinsbergen, D.J.J., Domeier, M., Gaina, C., Tohver, E., Meert, J.G., McCausland, P.J.A., Cocks, L.R.M., 2012.** Phanerozoic polar wander, palaeogeography and dynamics. *Earth Science Reviews* 114, 325–368.
- Van der Voo, R., 1969.** Paleomagnetic evidence for the rotation of the Iberian Peninsula. *Tectonophysics* 7, 5–56.
- Van Velzen, A.J., Zijdeveld, J.D.A., 1995.** Effects of weathering on single domain magnetite in early Pliocene marls. *Geophys. J. Int.* 121, 267–278.
- Vergés, J., M. Fernández, and A. Martínez, 2002.** The Pyrenean orogen: pre-, syn-, and post-collisional evolution, *J. Virtual Explor.*, 8, 55–74.
- Vissers, R.L.M., and P.T. Meijer, 2012,** Mesozoic rotation of Iberia: Subduction in the Pyrenees?, *Earth Sci. Rev.*, 110, 93–110.
- von Raumer, J., and Stampfli, G.M., 2008.** The birth of the Rheic Ocean – Early Palaeozoic subsidence patterns and tectonic plate scenarios. *Tectonophysics*, 461, 9–20
- Weil, A.B., Gutiérrez-Alonso, G., and Conan, J., 2010.** New time constraints on lithospheric-scale oroclinal bending of the Ibero-Armorican Arc: A paleomagnetic study of earliest Permian rocks from Iberia: *Journal of the Geological Society*, v. 167, p. 127–143, doi: 10.1144 /0016 - 76492009 -002.
- Weltje, G.J., 1997.** End-member modelling of compositional data: numerical–statistical algorithms for solving the explicit mixing problem. *Journal of Mathematical Geology*, 29, 503–549.
- Young, G.C., 1987.** Devonian palaeontological data and the Armorica problem. *Palaeogeogr. Palaeoclimatol. Palaeoecol.* 60, 283–304.
- Young, G.C., 1990.** Devonian vertebrate distribution patterns and cladistic analysis of palaeogeographic hypotheses. In: McKerrow, W.S., Scotese, C.R. (Eds.), *Palaeozoic Palaeogeography and Biogeography*. *Geol. Soc. London Mem.* 12, pp. 243–255.
- Zijdeveld, J.D.A., 1967.** A.C. demagnetization of rocks: analysis of results, *Methods in Paleomagnetism* (254–286)

# 8. appendices

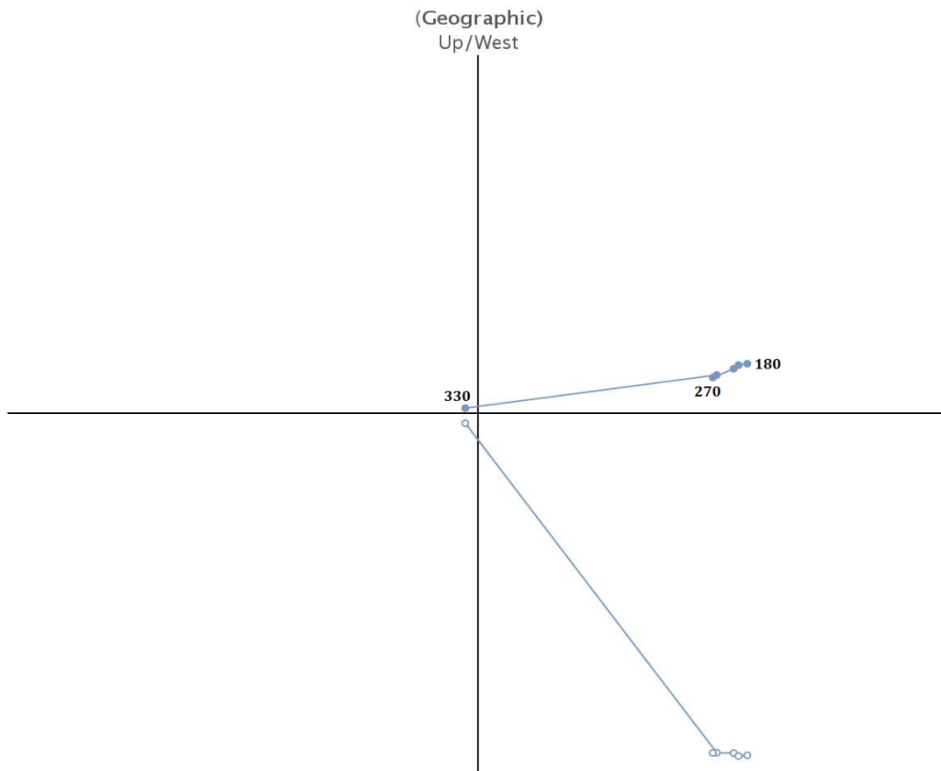
## 8.1 Zijderveld diagrams

This section shows a representative Zijderveld diagram for every site. The numbers concern temperature in °C (100 or above) or steps in alternating field demagnetization (below 100). Zijderveld diagrams that lack temperature notifications do not have a relevant discernable component.

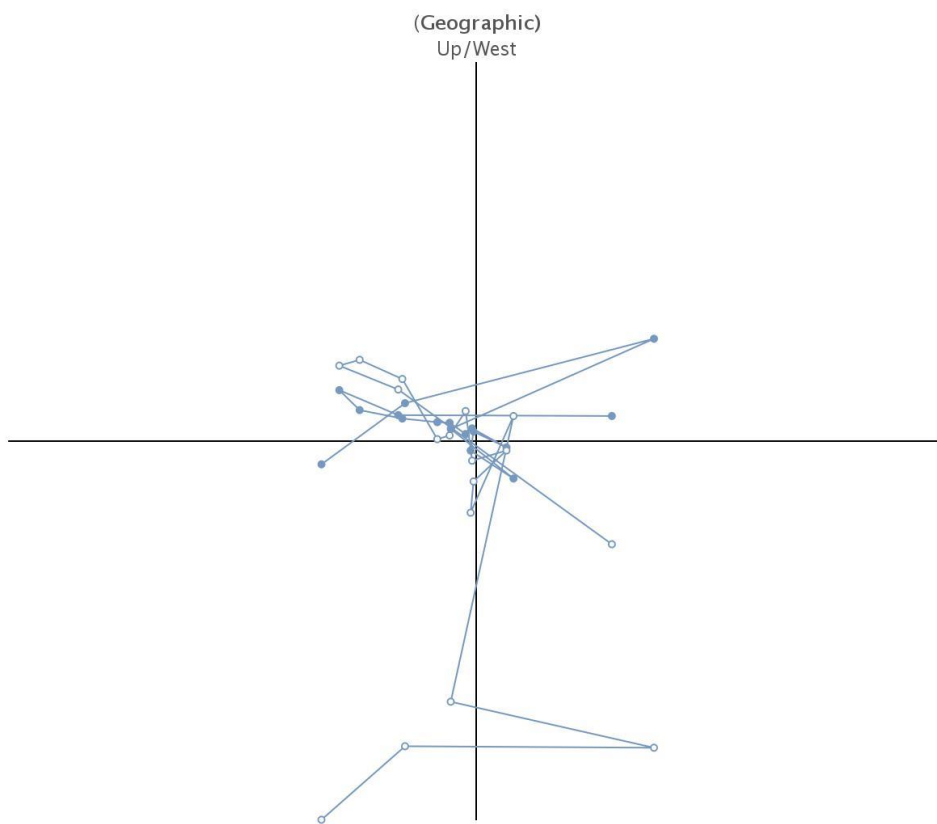
Zijderveld Diagram (OG1-3A)



### Zijderveld Diagram (OG2-3A)

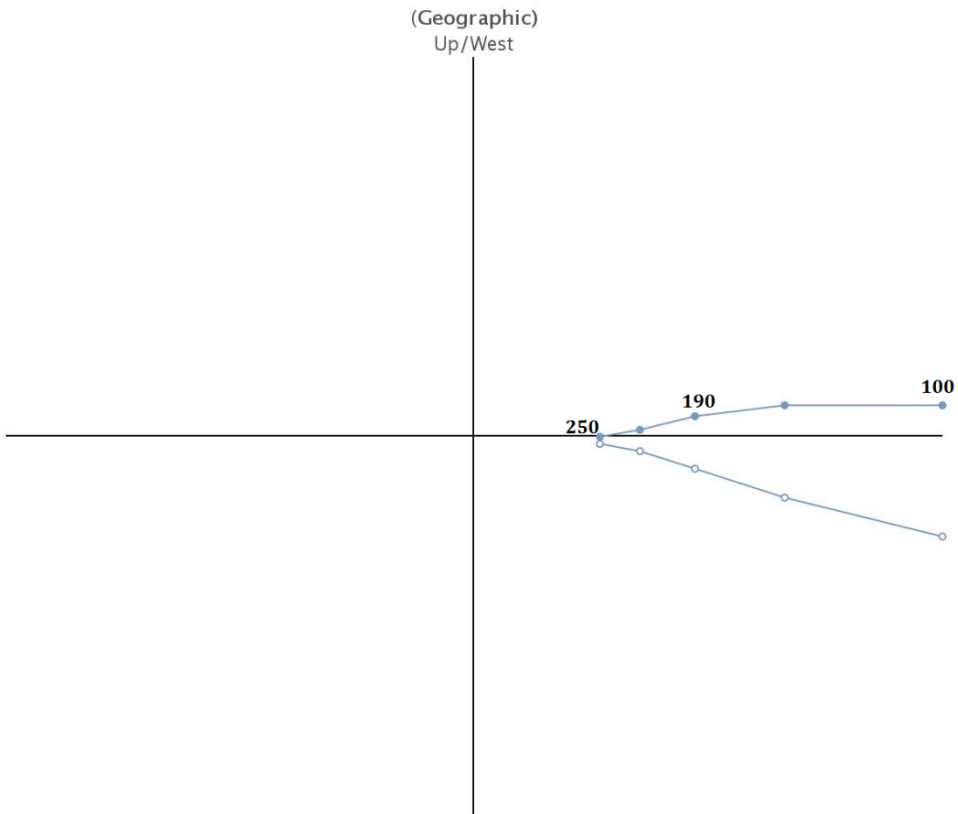


### Zijderveld Diagram (OG3-7A)

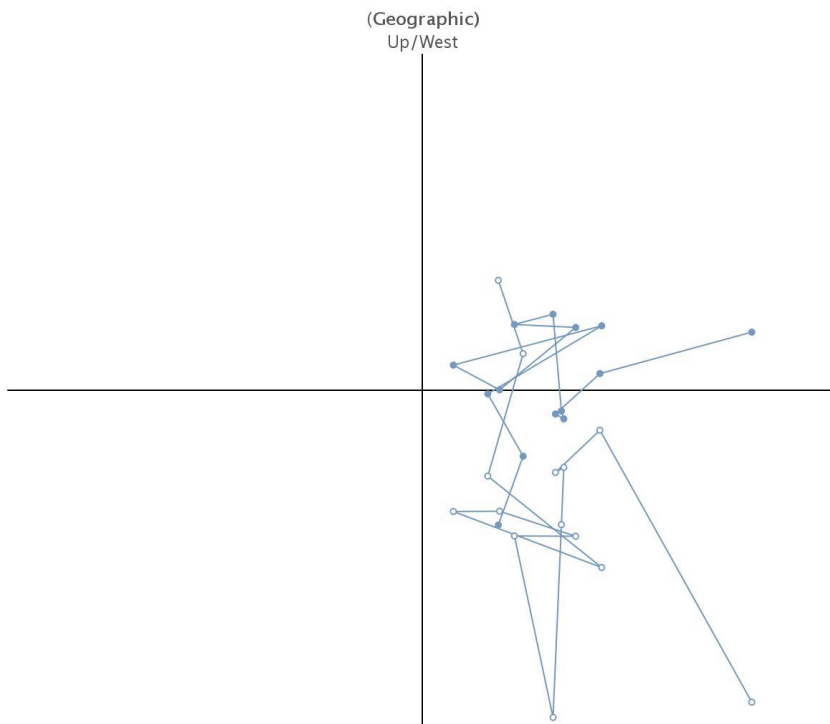


Paleomagnetism.org (Zijderveld Diagram)

### Zijderveld Diagram (OG4-23A)



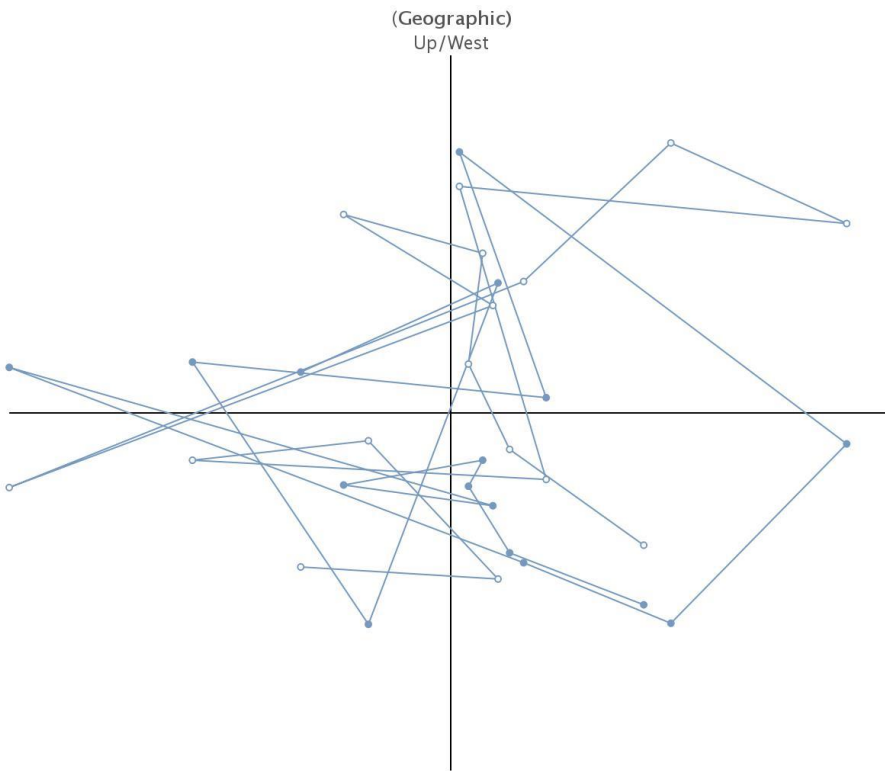
### Zijderveld Diagram (OG5-8A)



- Horizontal Projection
- Vertical Projection

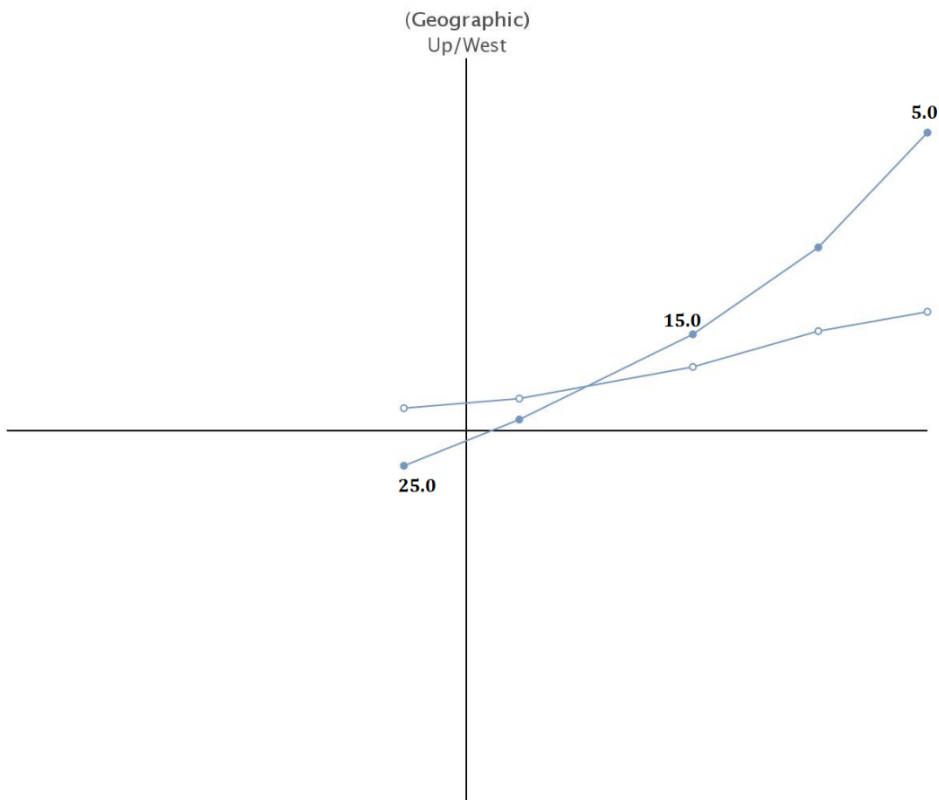
Paleomagnetism.org (Zijderveld Diagram)

### Zijderveld Diagram (OG6-2B)



• Horizontal Projection    ○ Vertical Projection  
Paleomagnetism.org (Zijderveld Diagram)

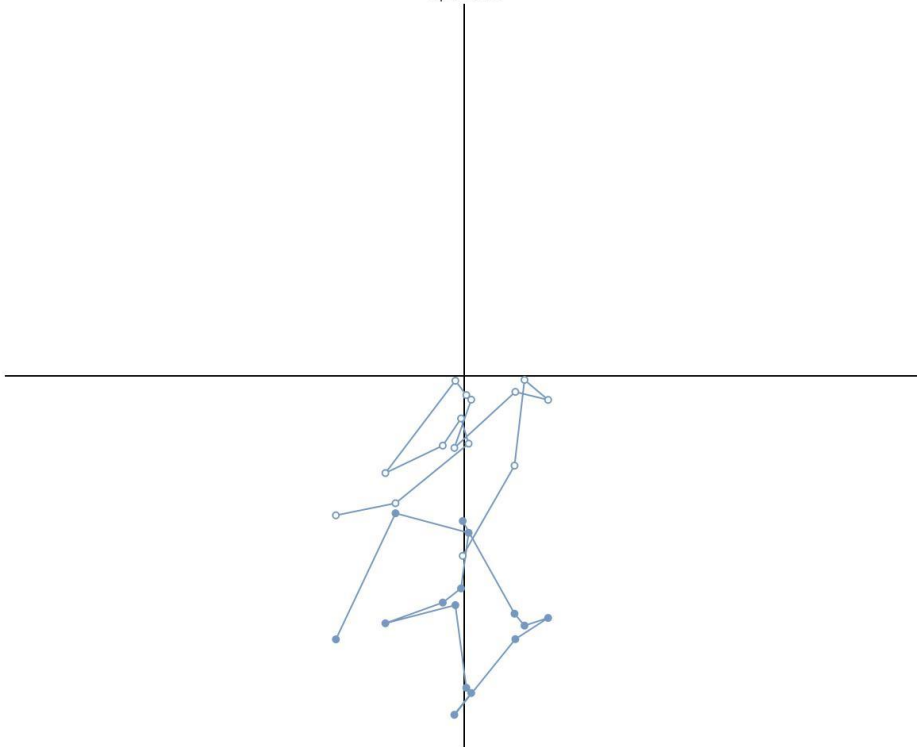
### Zijderveld Diagram (OG7.2A2)





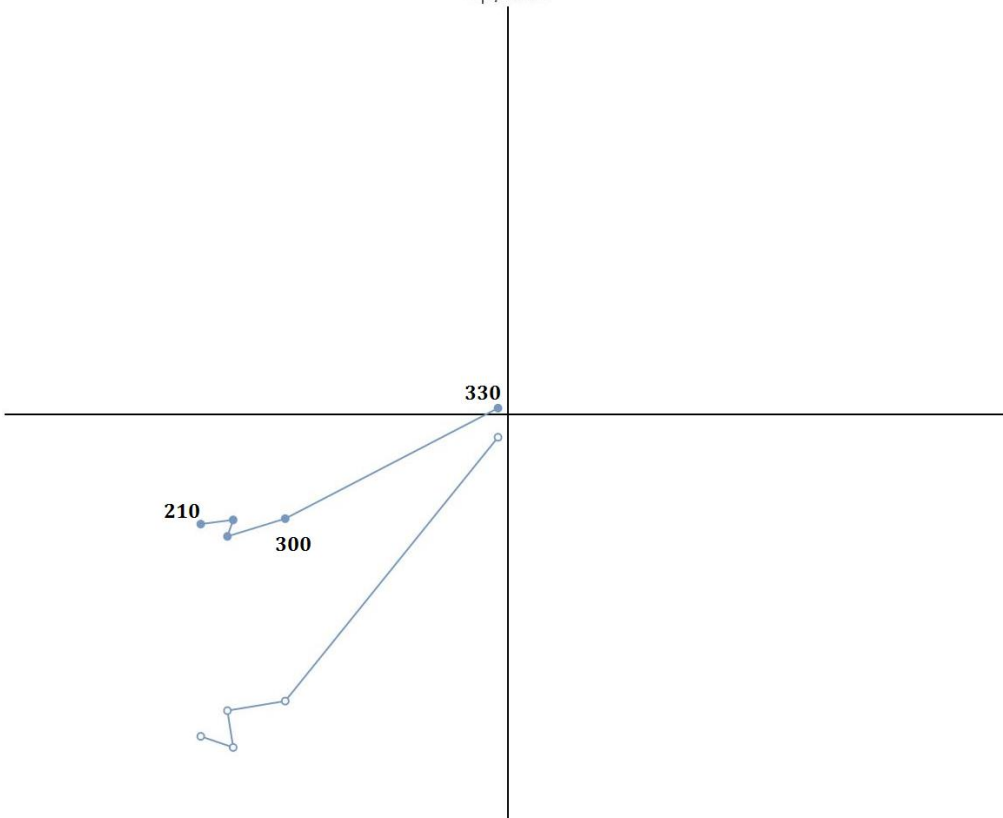
### Zijderveld Diagram (OG8.2)

(Geographic)  
Up/West

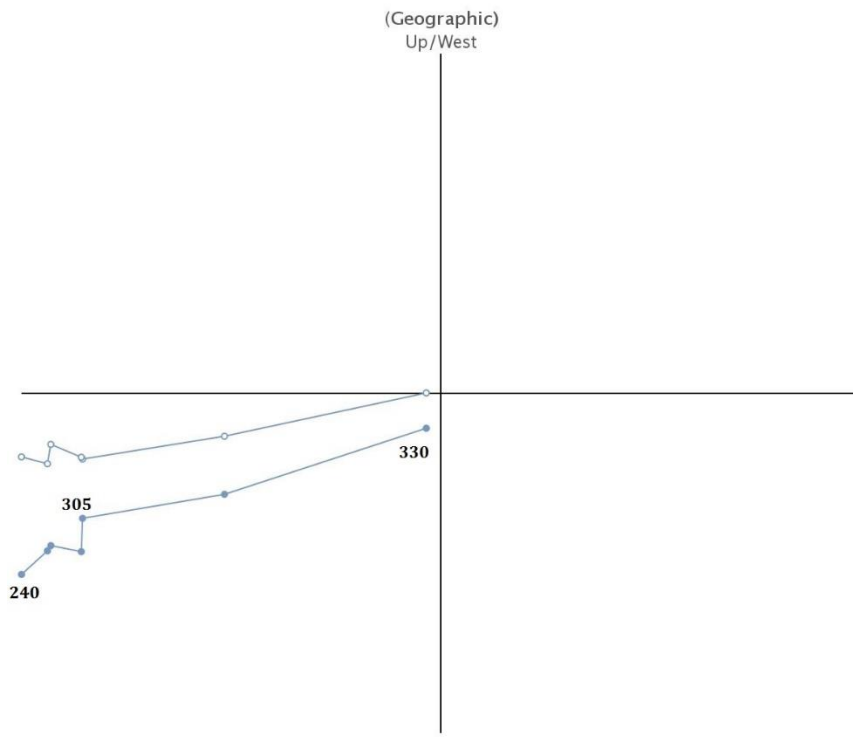


### Zijderveld Diagram (OG9-4A)

(Geographic)  
Up/West



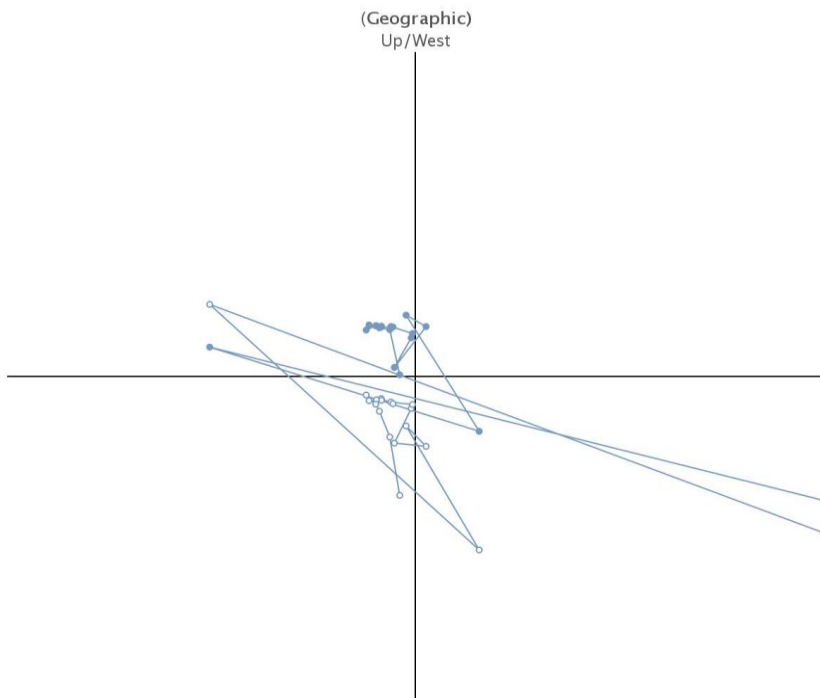
### Zijderveld Diagram (OG10-7B)



● Horizontal Projection ○ Vertical Projection

[Paleomagnetism.org](http://Paleomagnetism.org) (Zijderveld Diagram)

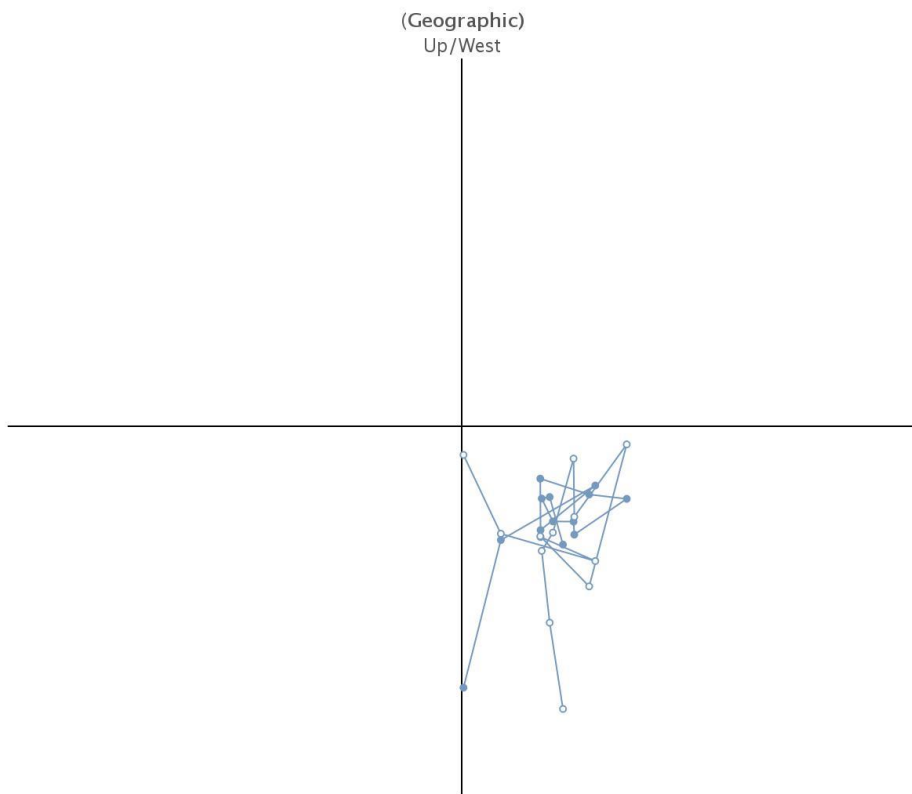
### Zijderveld Diagram (OG11-12A)



● Horizontal Projection ○ Vertical Projection

[Paleomagnetism.org](http://Paleomagnetism.org) (Zijderveld Diagram)

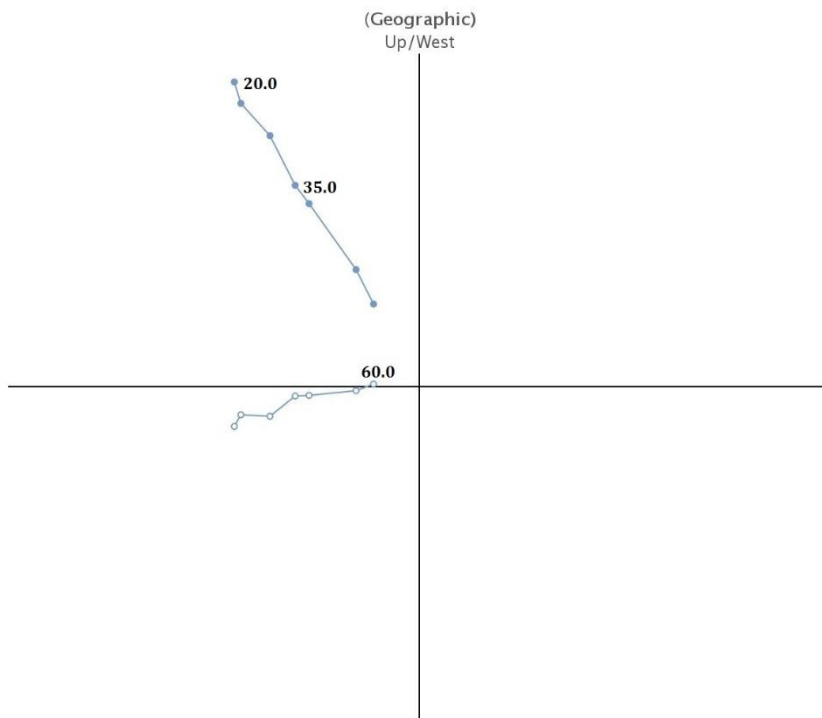
### Zijderveld Diagram (OG12-9C)



- Horizontal Projection
- Vertical Projection

Paleomagnetism.org (Zijderveld Diagram)

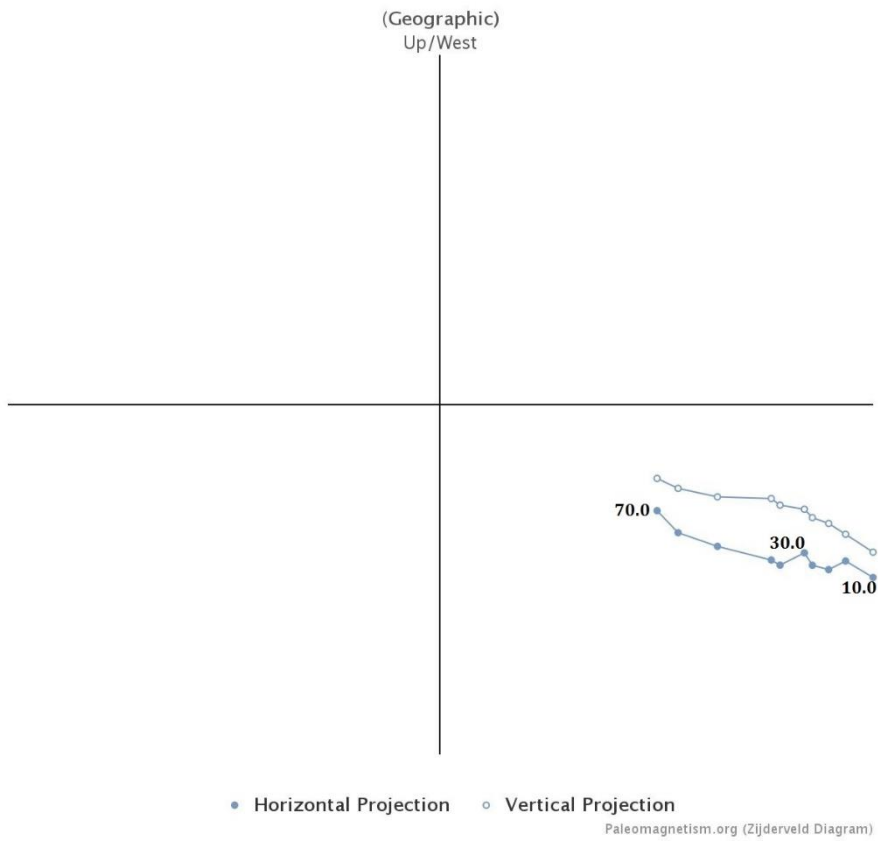
### Zijderveld Diagram (OG13-4)



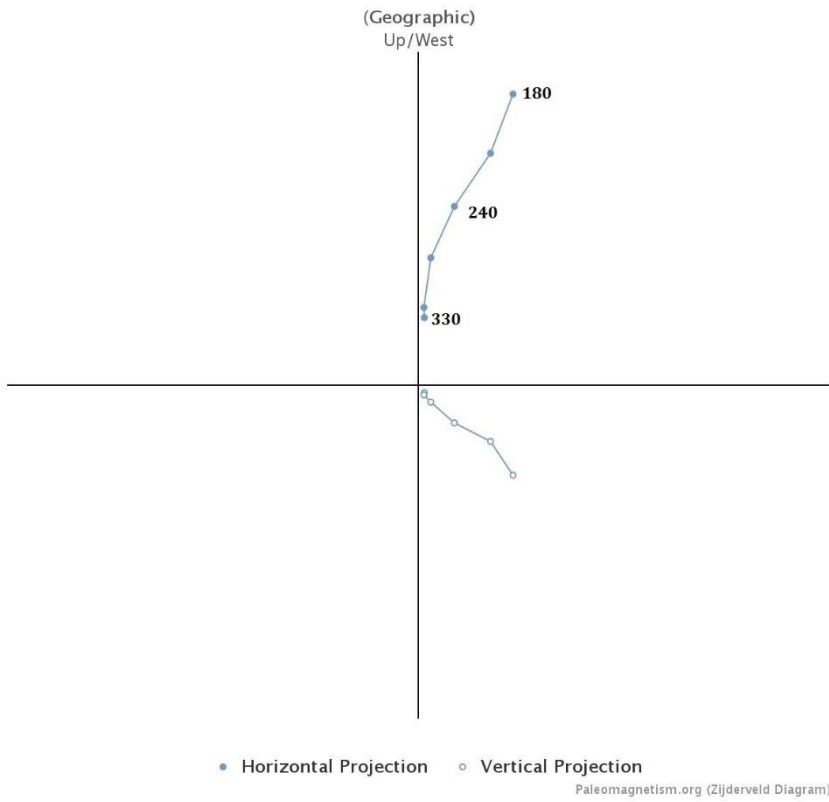
- Horizontal Projection
- Vertical Projection

Paleomagnetism.org (Zijderveld Diagram)

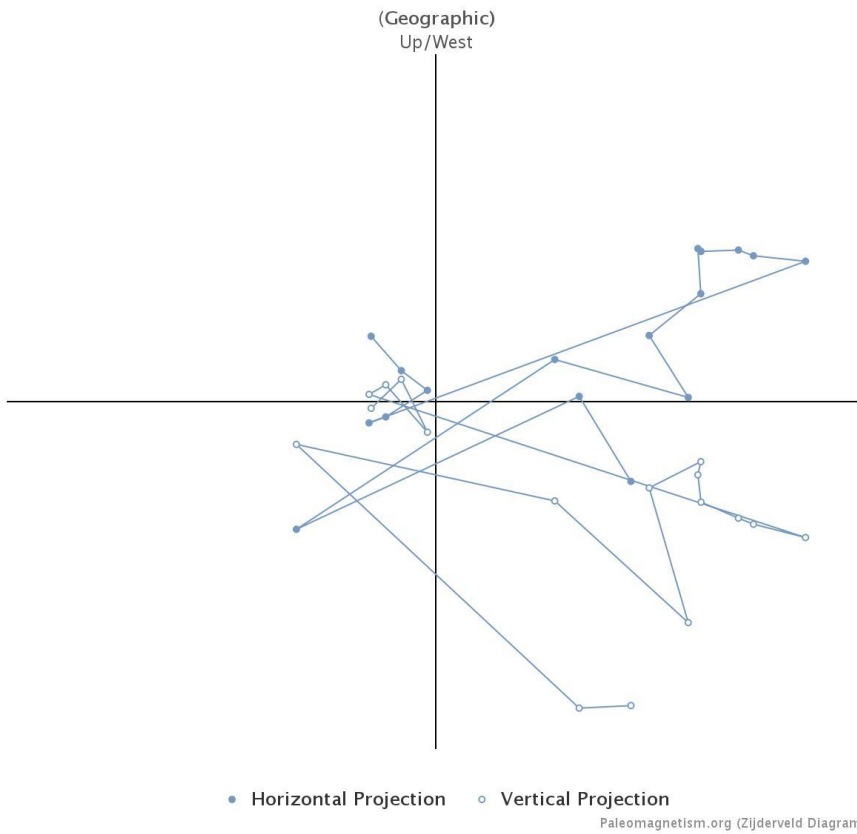
### Zijderveld Diagram (OG14-13)



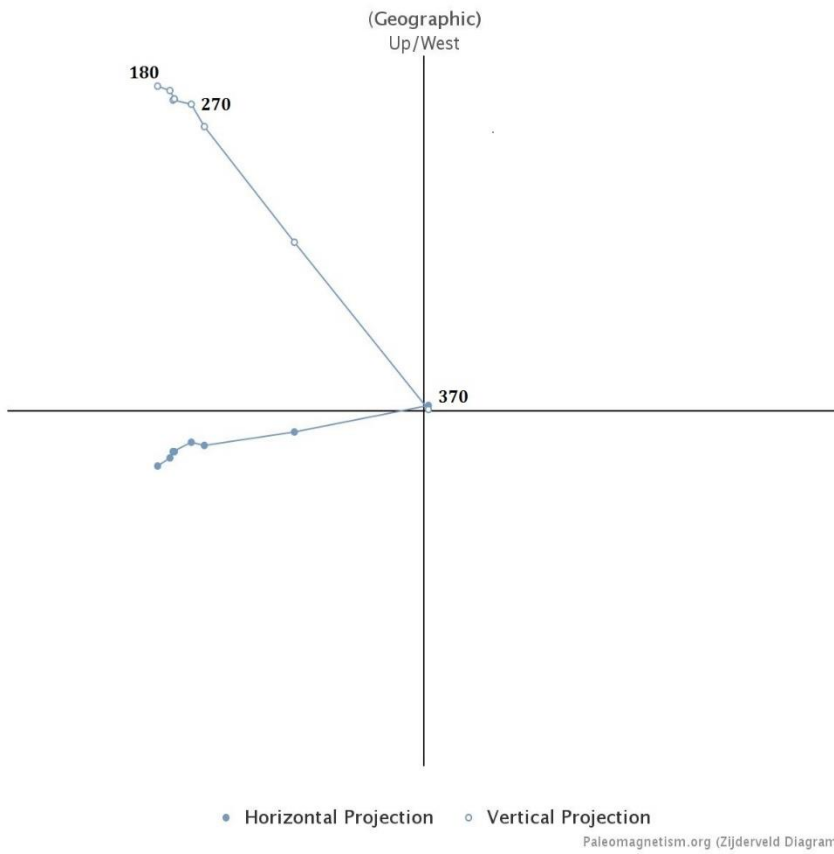
### Zijderveld Diagram (OG15-8B)



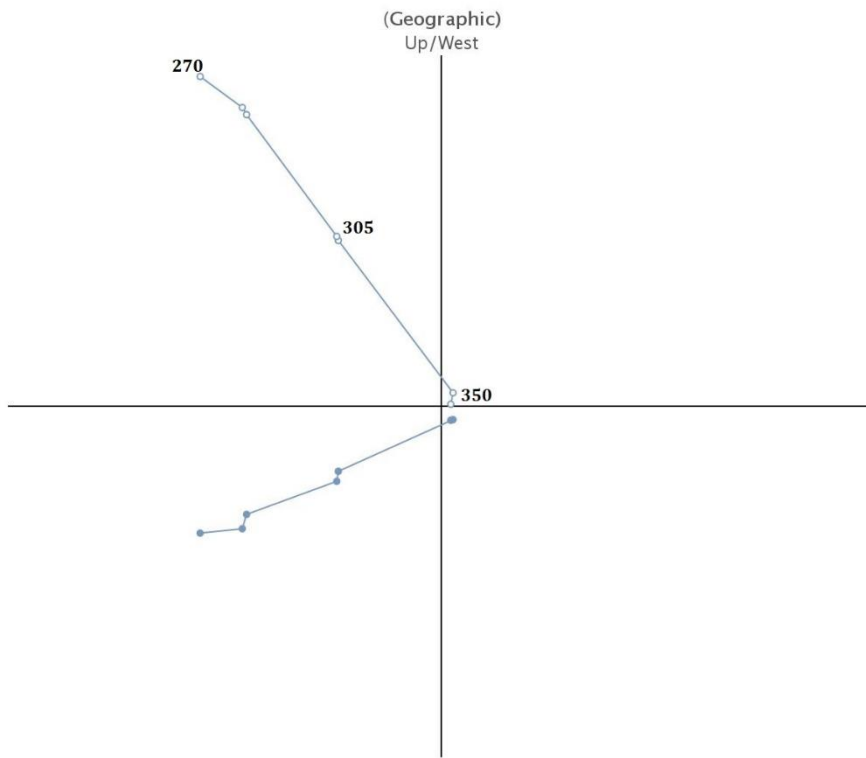
### Zijderveld Diagram (OG16-9A)



### Zijderveld Diagram (OG17-9A)



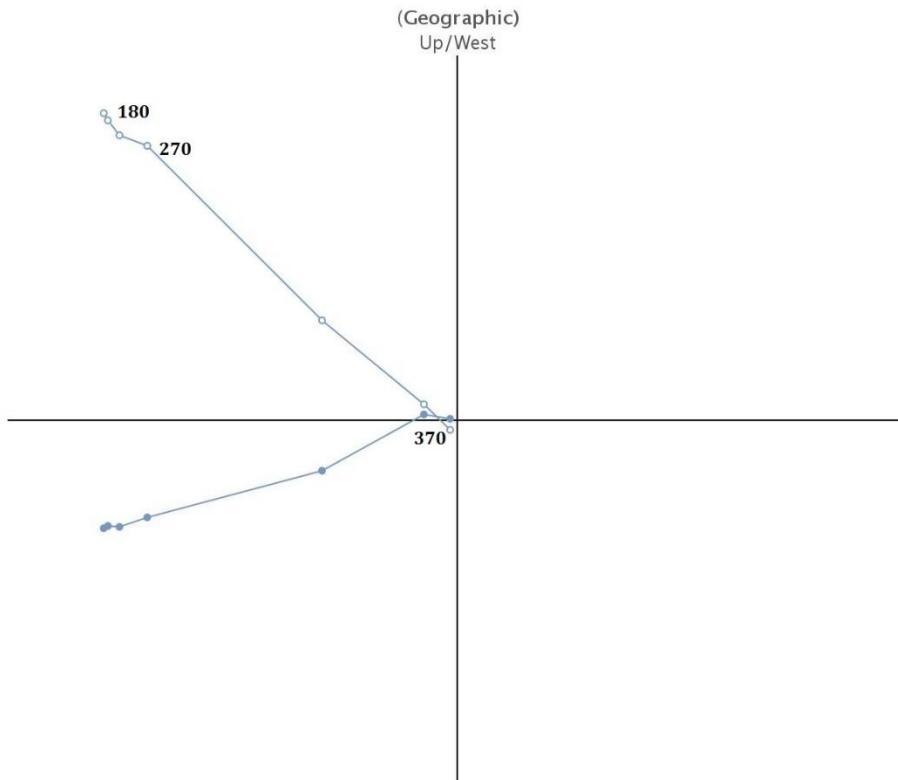
### Zijderveld Diagram (OG18-5)



• Horizontal Projection    ◦ Vertical Projection

Paleomagnetism.org (Zijderveld Diagram)

### Zijderveld Diagram (OG19-5B)



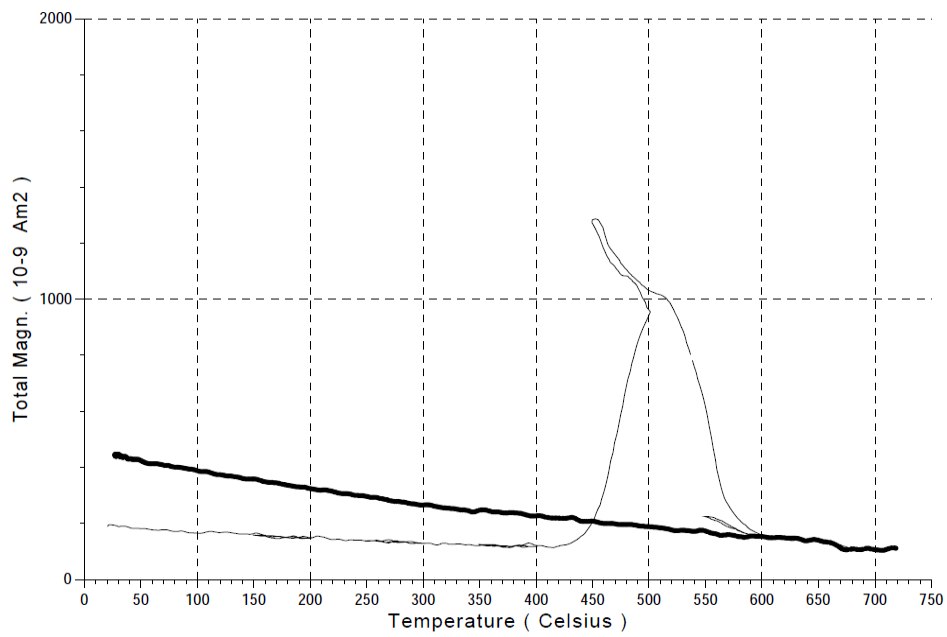
• Horizontal Projection    ◦ Vertical Projection

Paleomagnetism.org (Zijderveld Diagram)

## 8.2 Curie balance plots

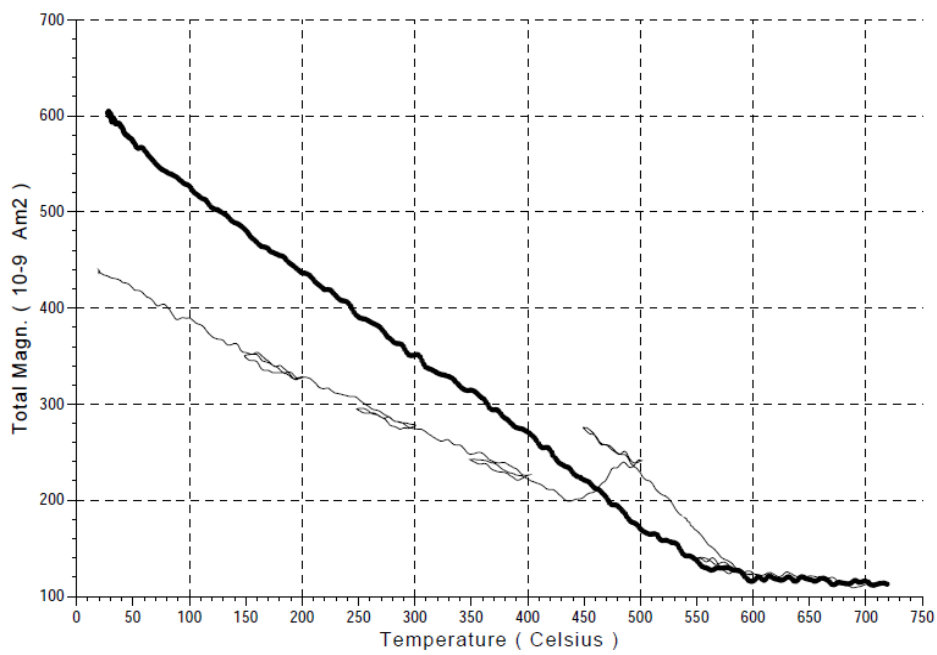
OG2----TOTAL

Field: 100 - 300 mT. 10/ 10 T/min. Weight: .06682. Max. temp.: 200



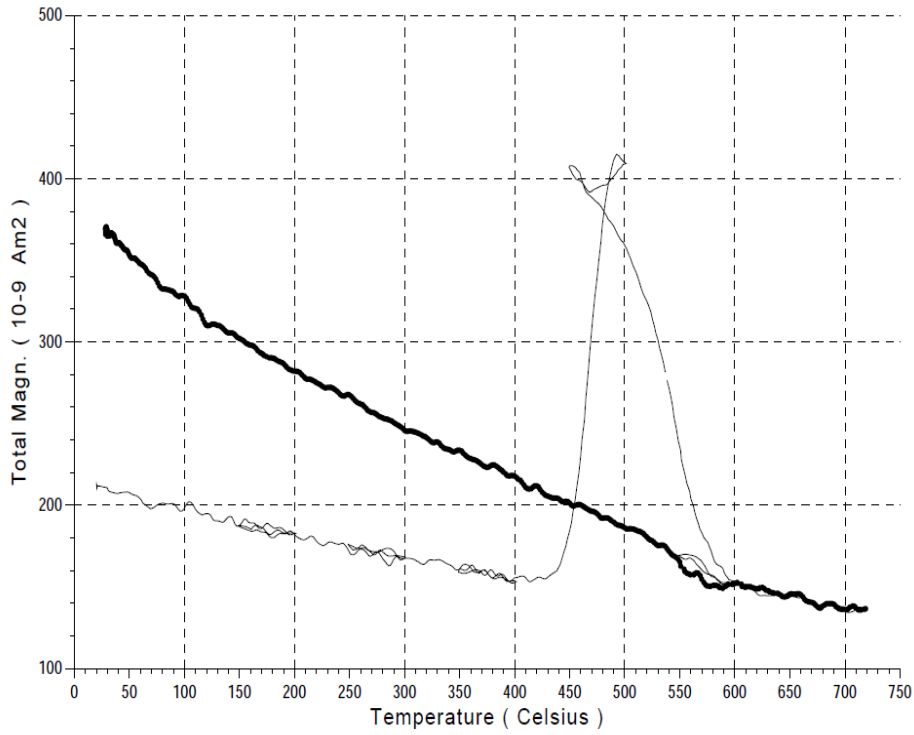
OG4----TOTAL

Field: 100 - 300 mT. 10/ 10 T/min. Weight: .06625. Max. temp.: 200



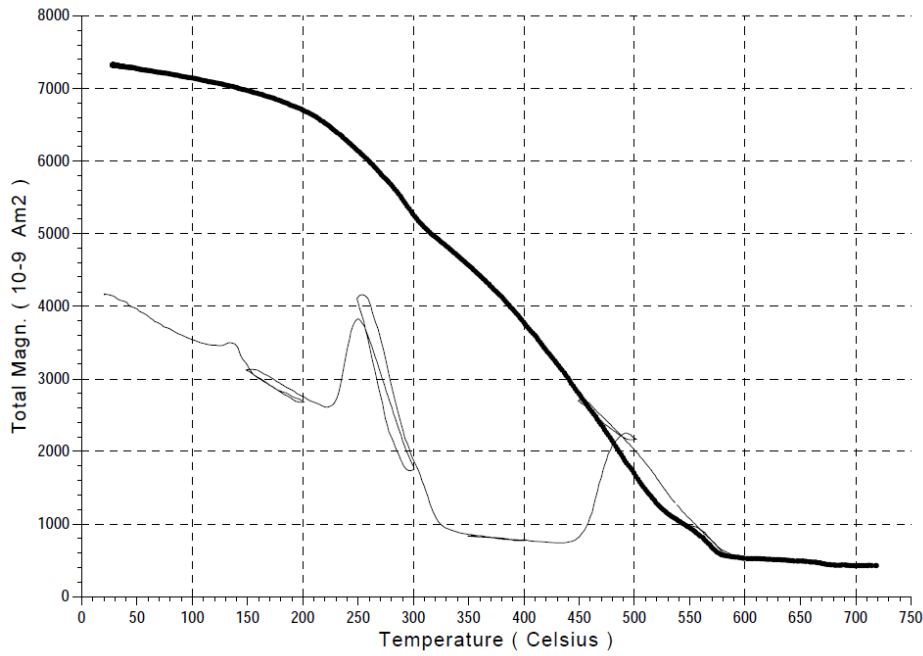
OG5----TOTAL

Field: 100 - 300 mT. 10/ 10 T/min. Weight: .0882. Max. temp.: 200



OG6----TOTAL

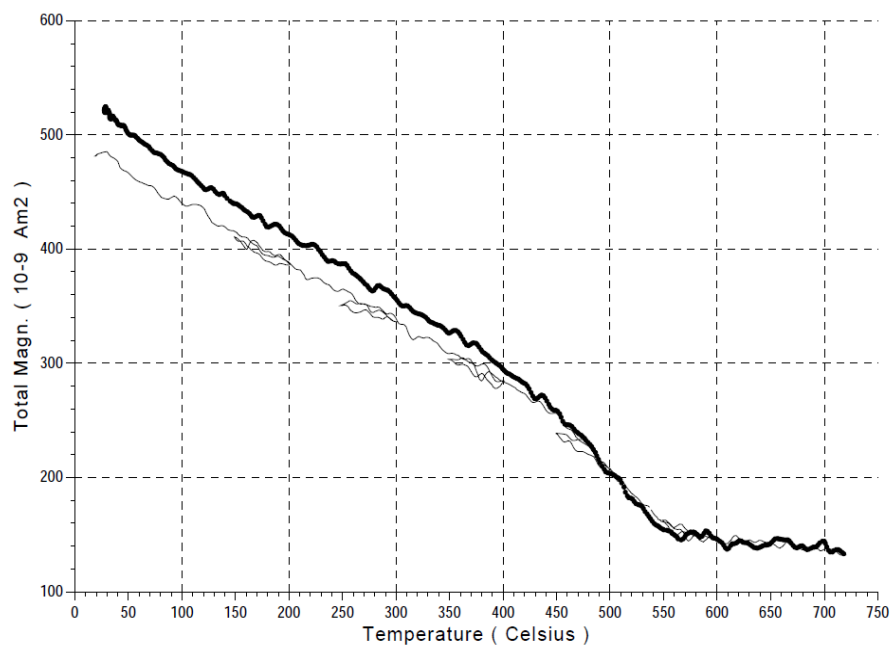
Field: 100 - 300 mT. 10/ 10 T/min. Weight: .09919. Max. temp.: 200





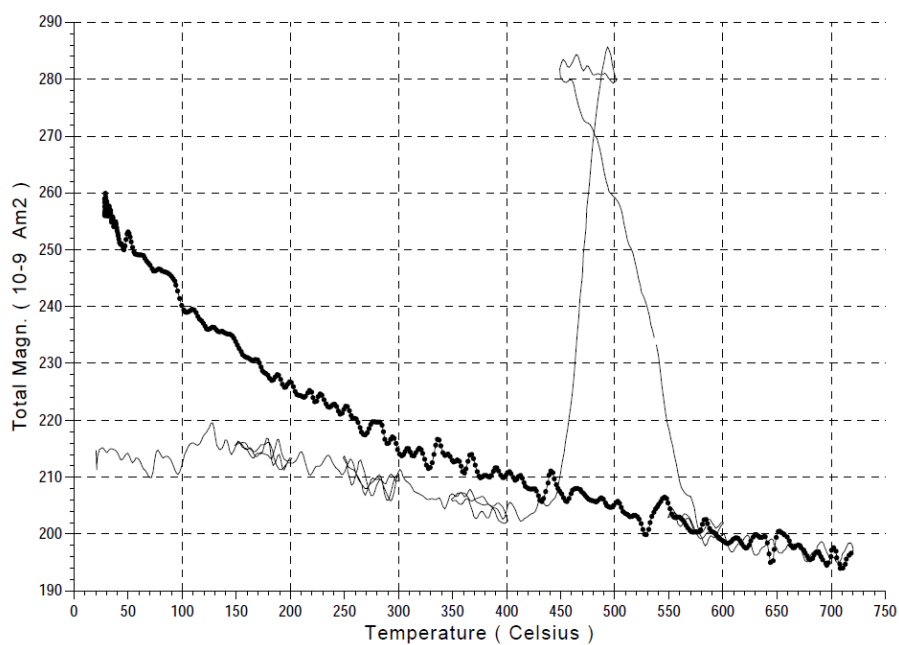
### OG15----TOTAL

Field: 100 - 300 mT. 10/ 10 T/min. Weight: .03646. Max. temp.: 200



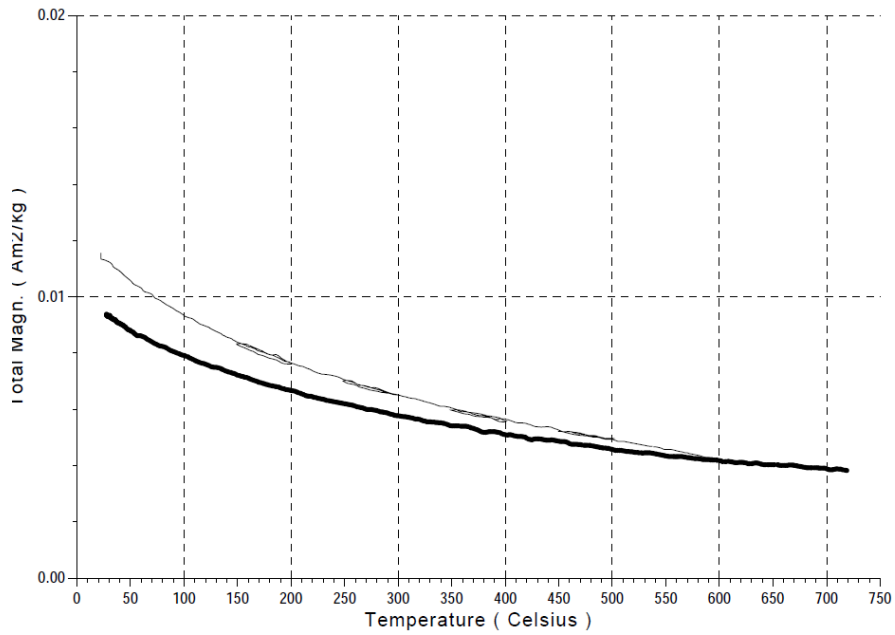
### OG17----TOTAL

Field: 100 - 300 mT. 10/ 10 T/min. Weight: .02144. Max. temp.: 200

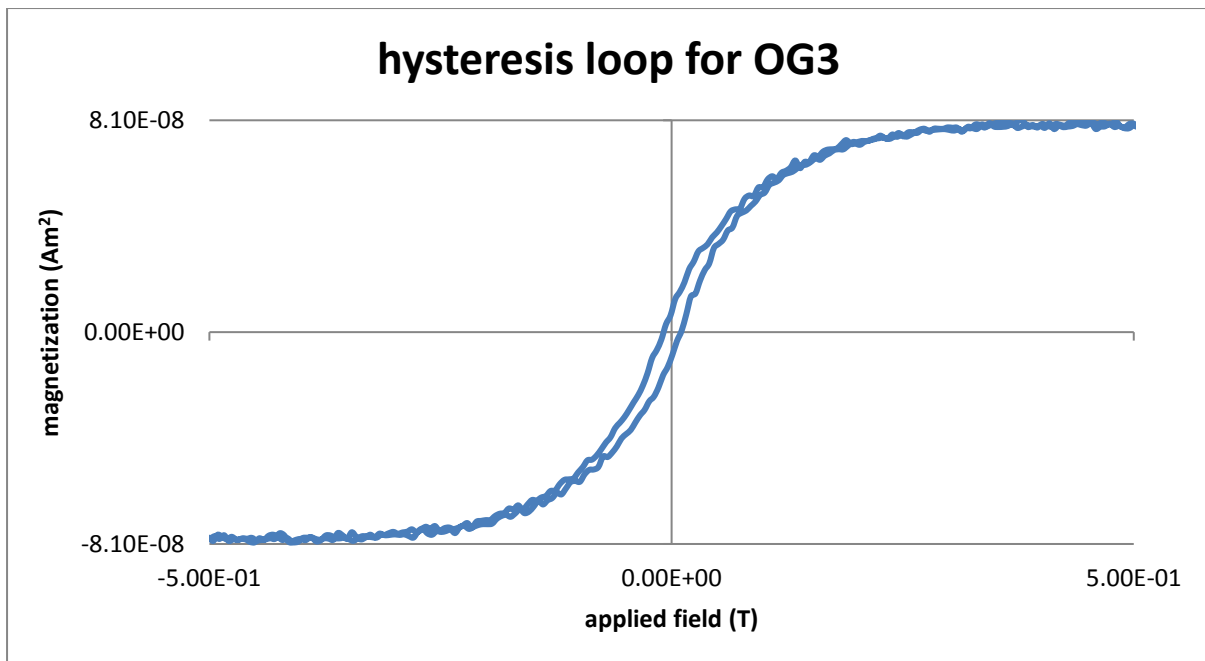


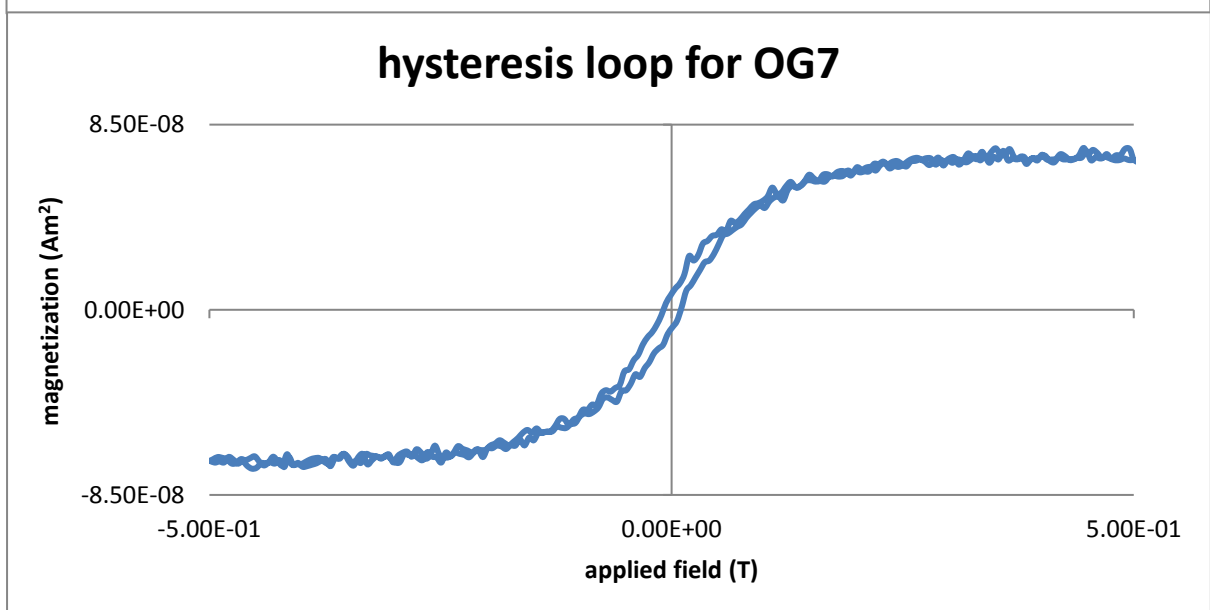
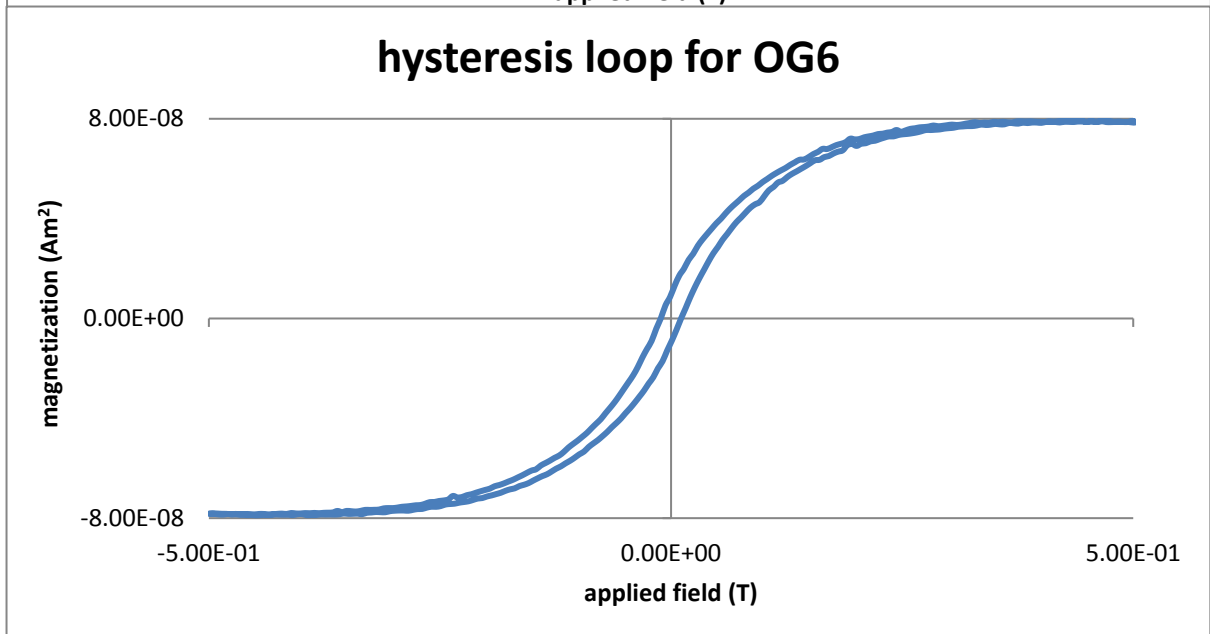
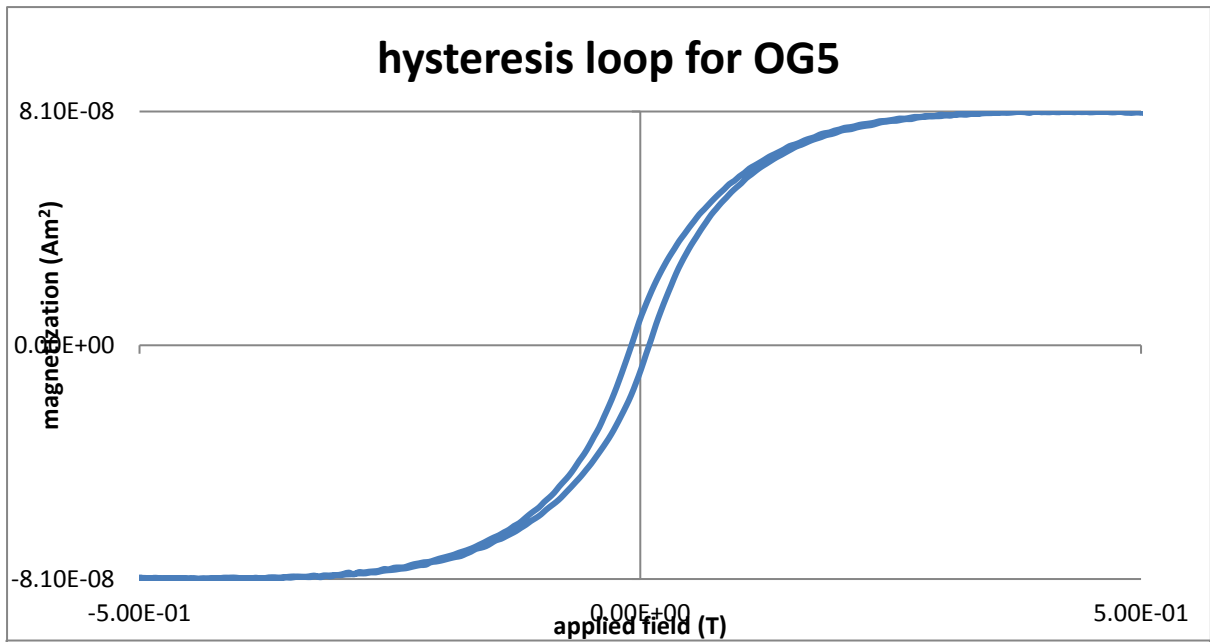
### OG19---please work-TOTAL

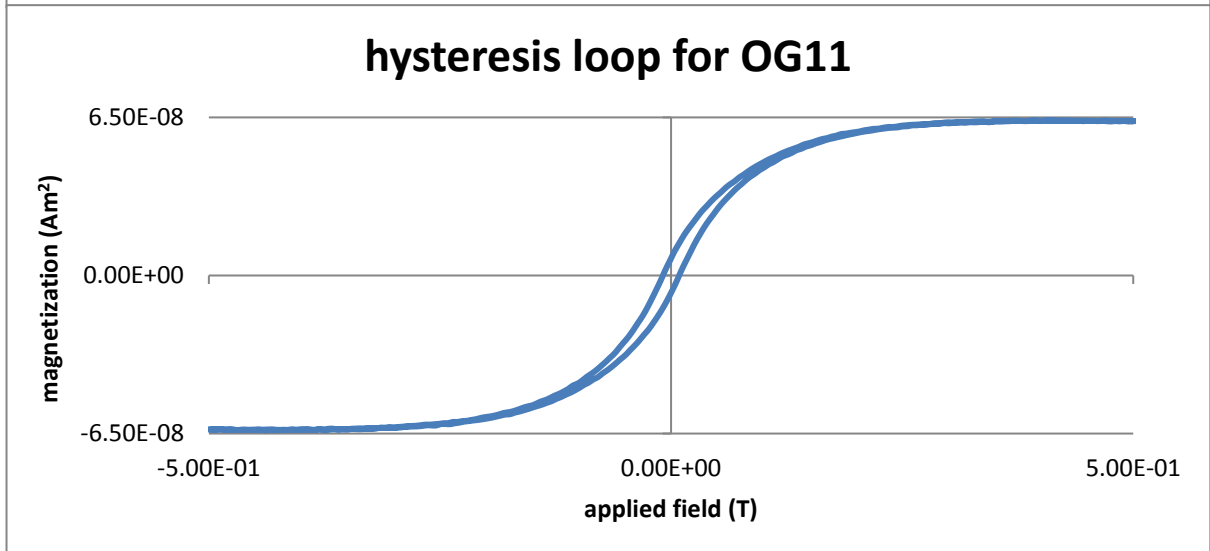
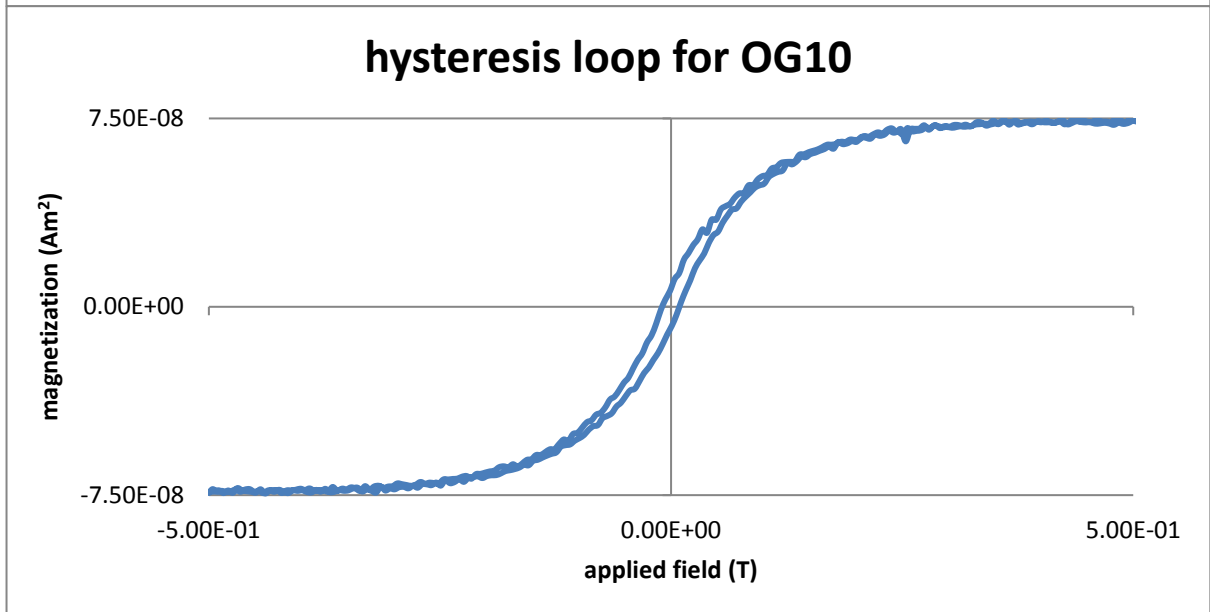
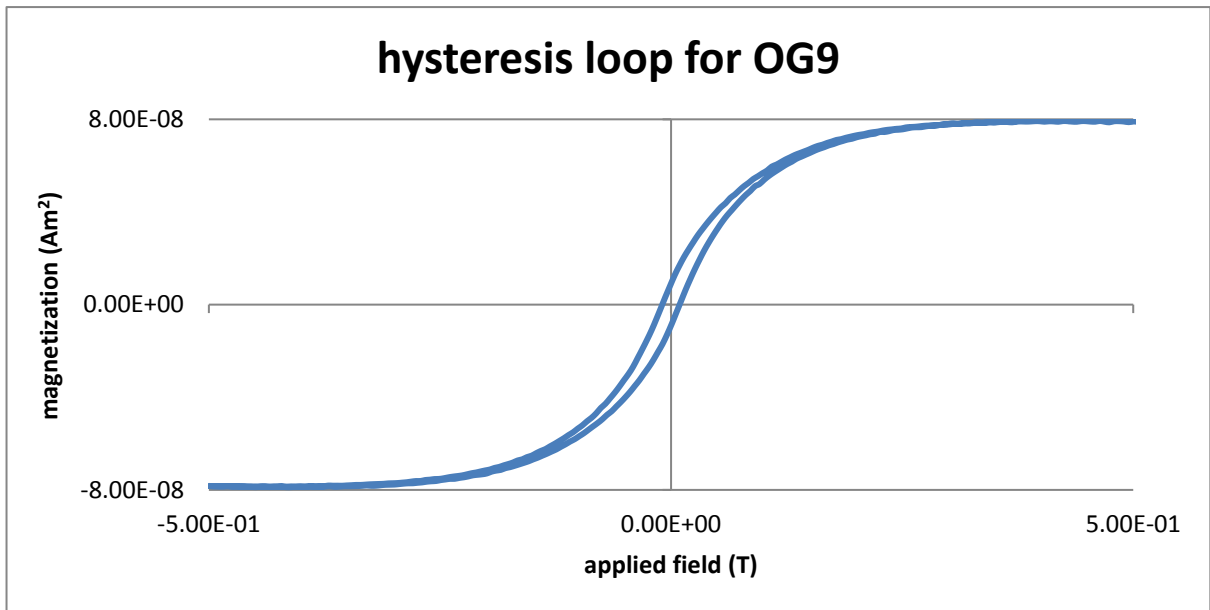
Field: 100 - 300 mT. 10/ 10 T/min. Weight: .06479. Max. temp.: 200

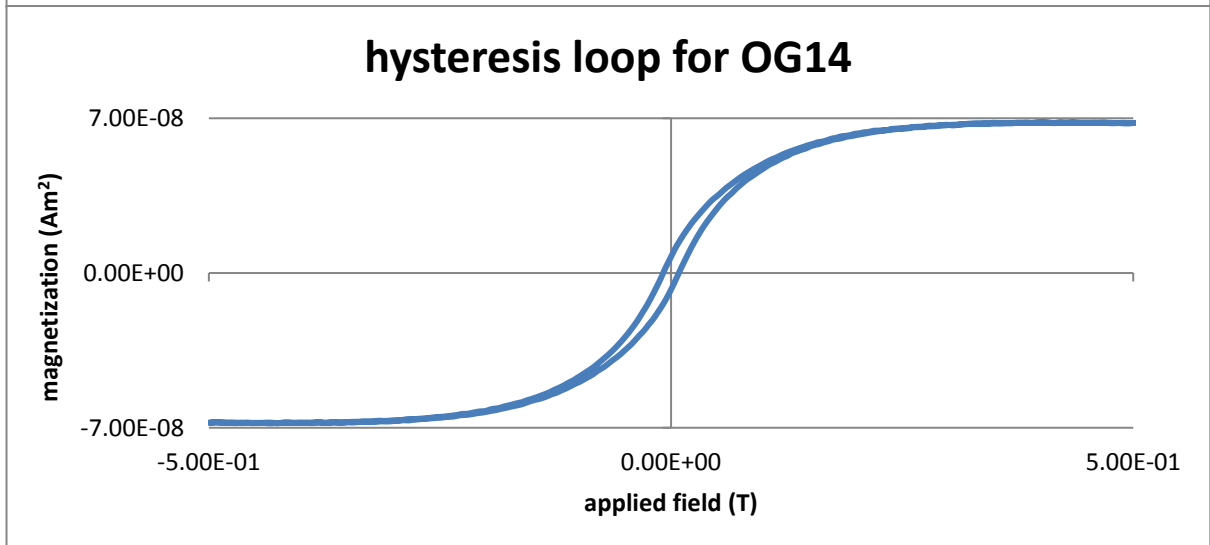
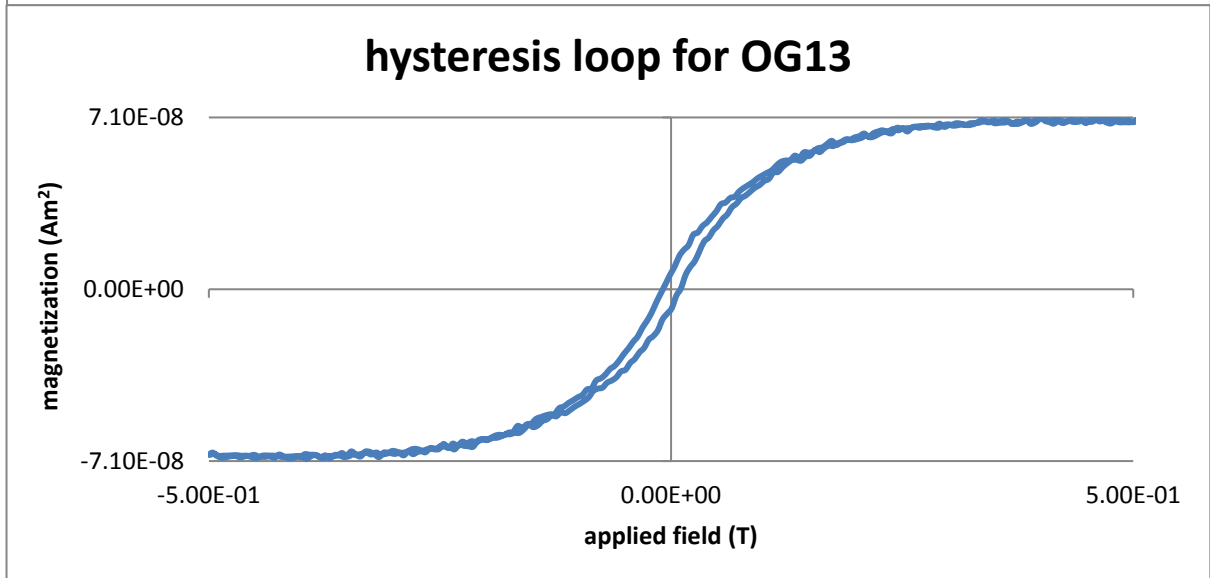
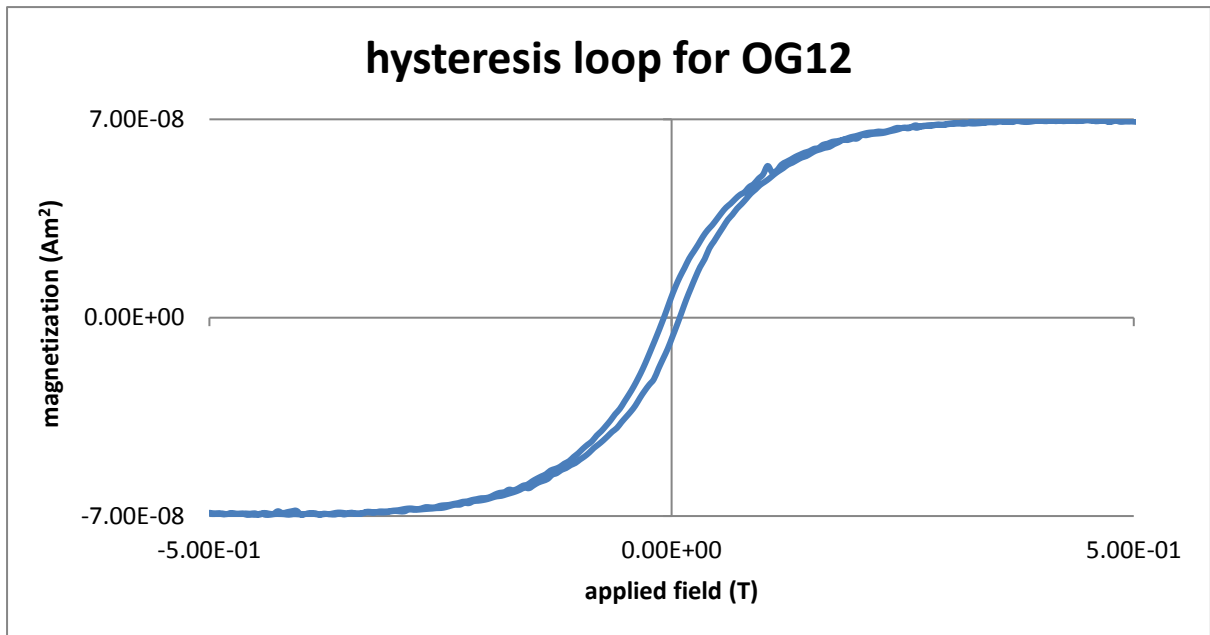


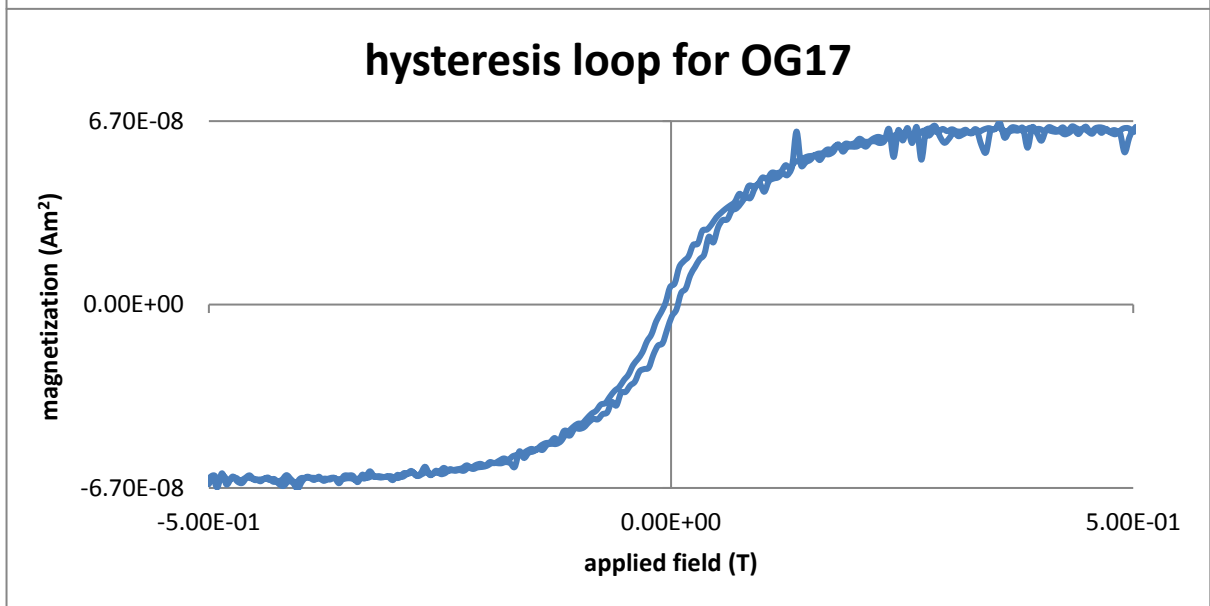
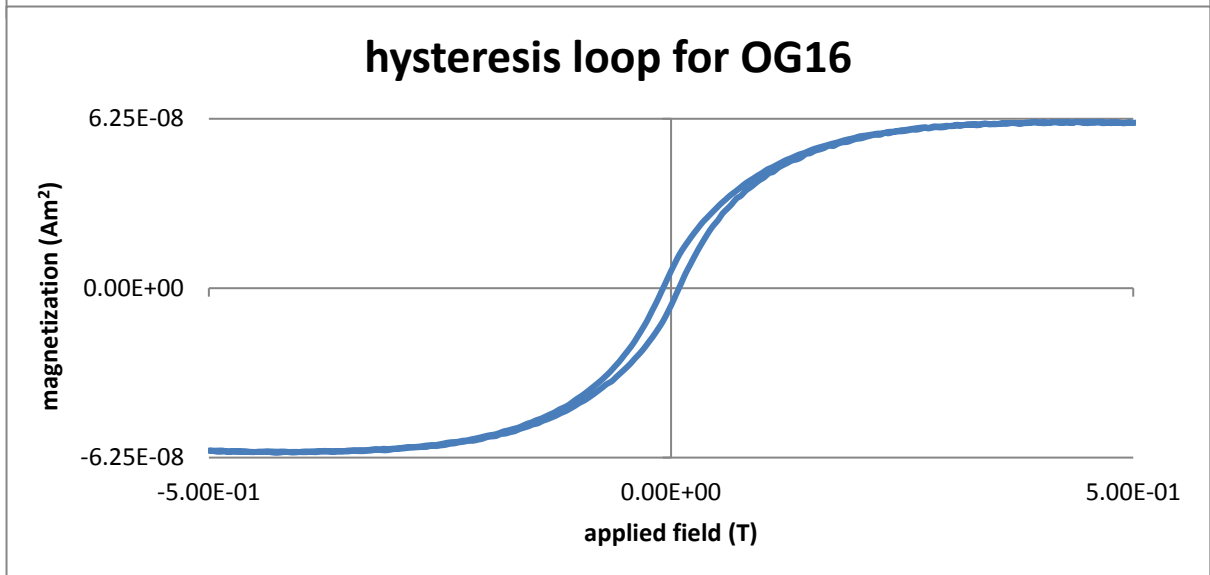
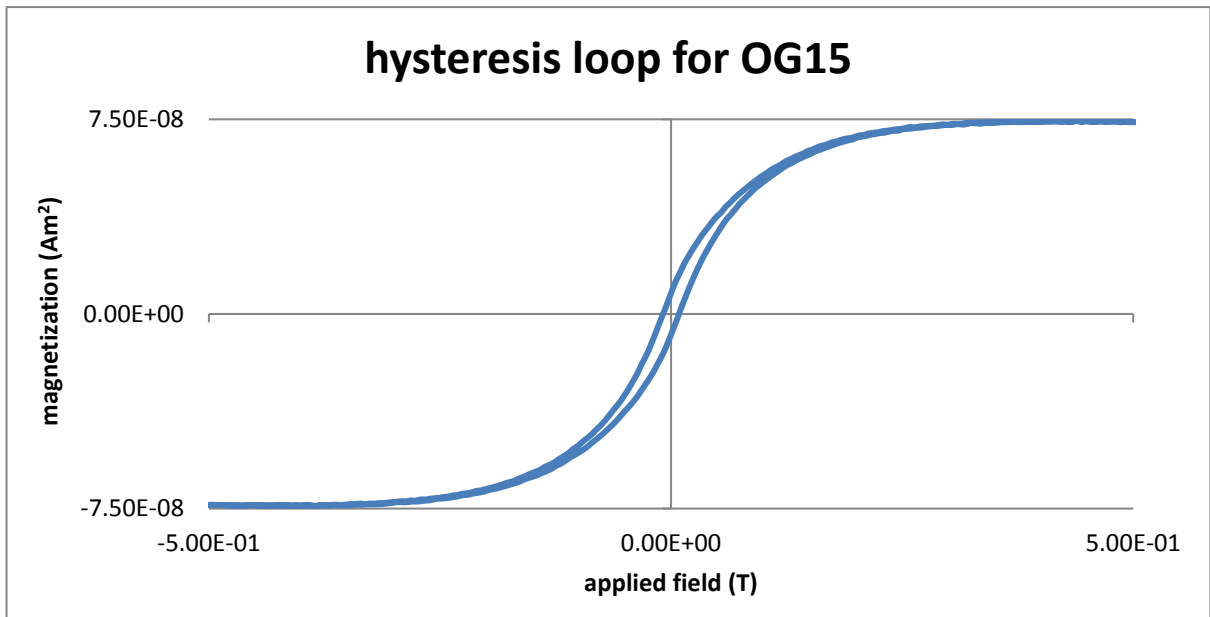
### 8.3 hysteresis loops

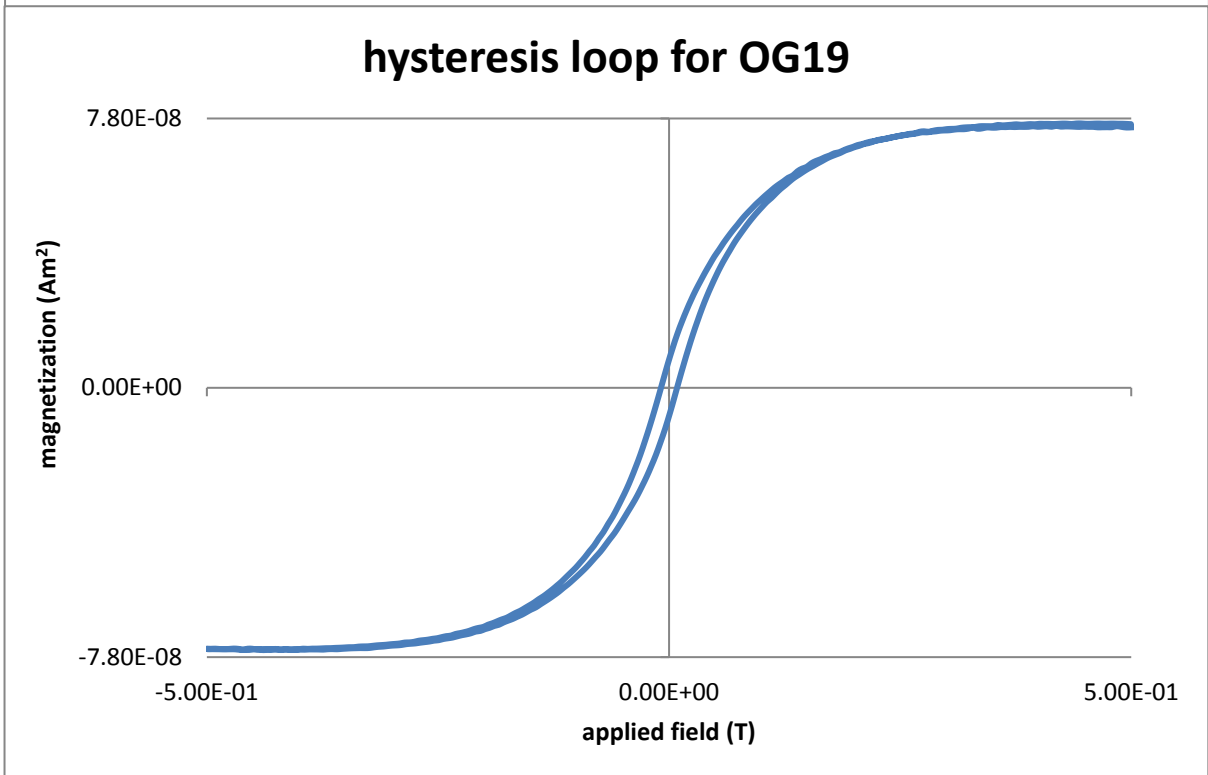
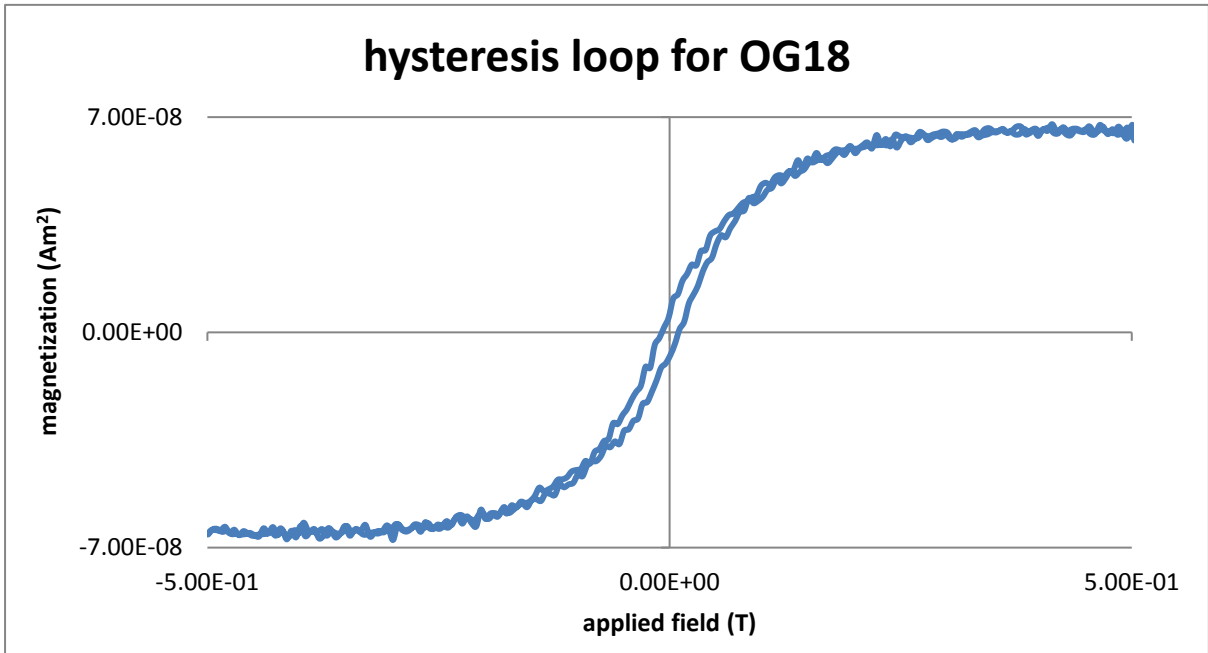






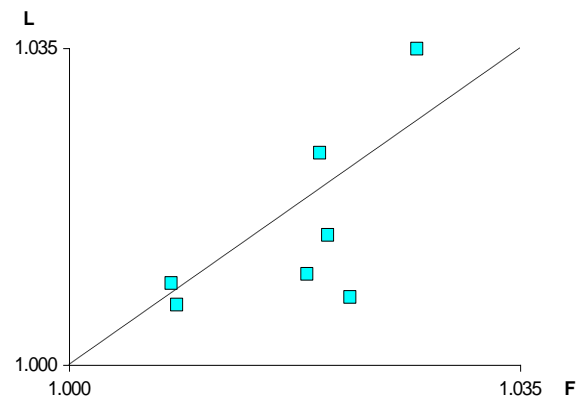
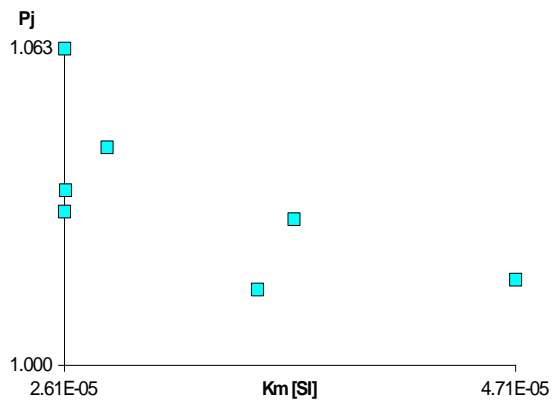
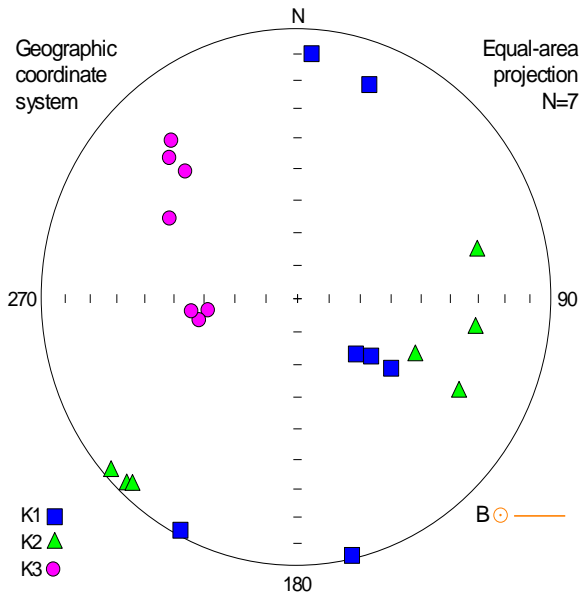




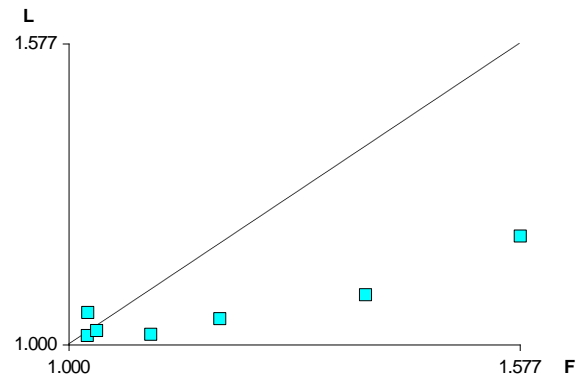
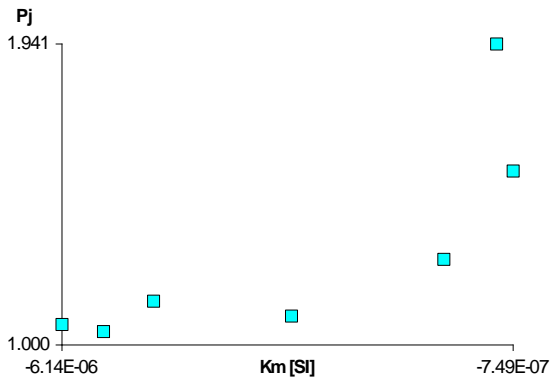
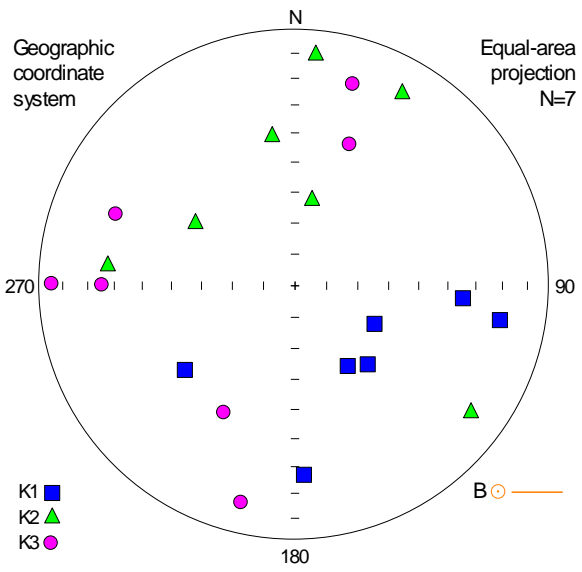


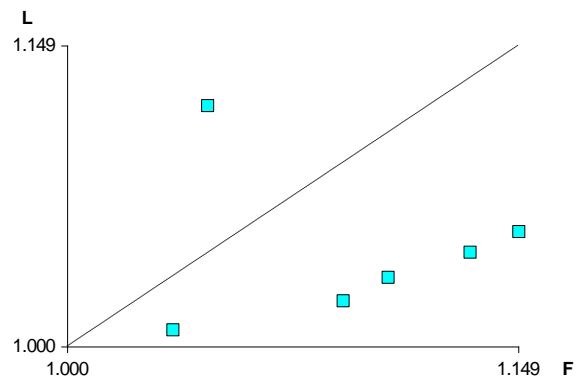
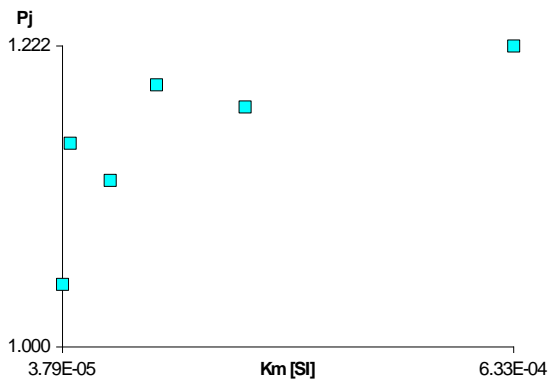
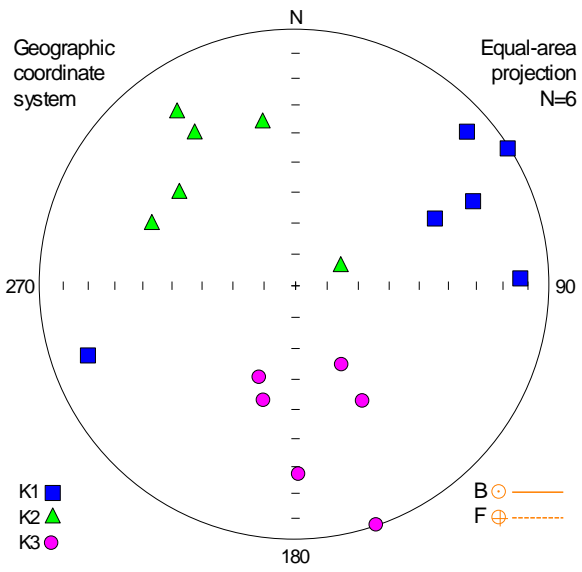
## 8.4 anisotropy of magnetic susceptibility

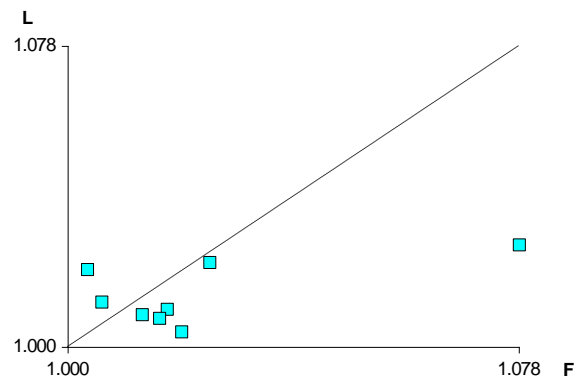
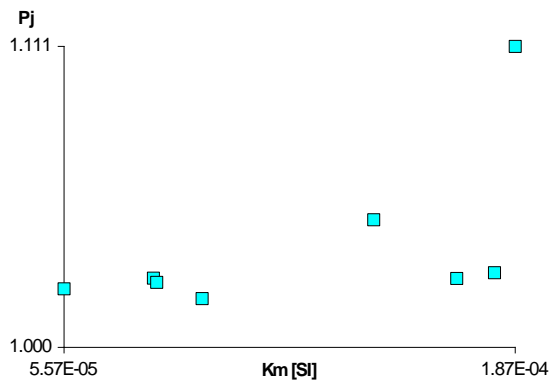
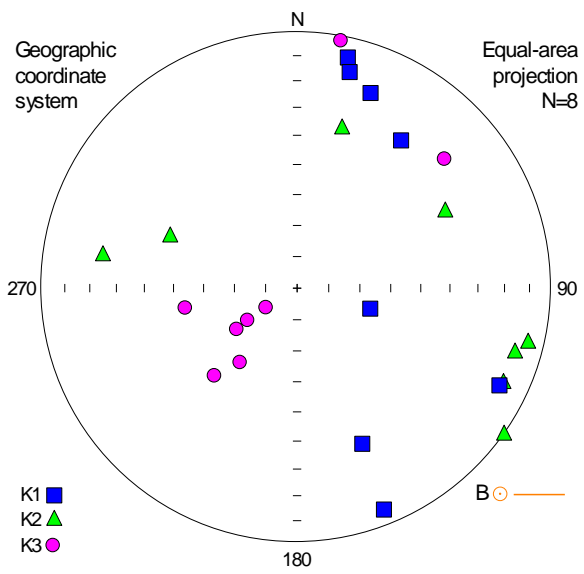
The figures are for the sites OG3, OG5, OG6, OG10, OG11, OG12, OG14, OG15, OG16 and OG17, in that order.

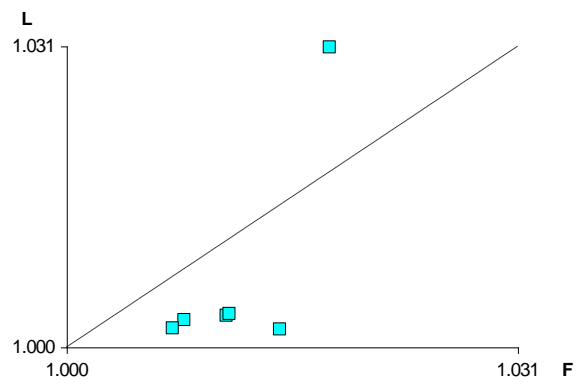
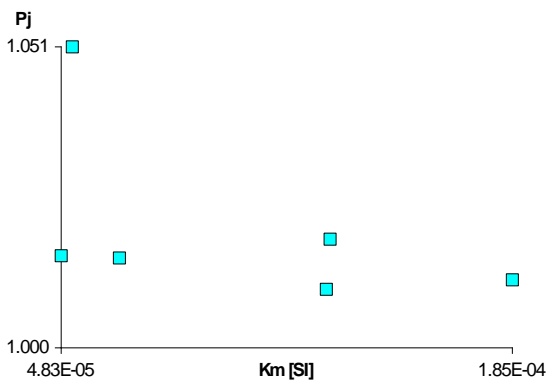
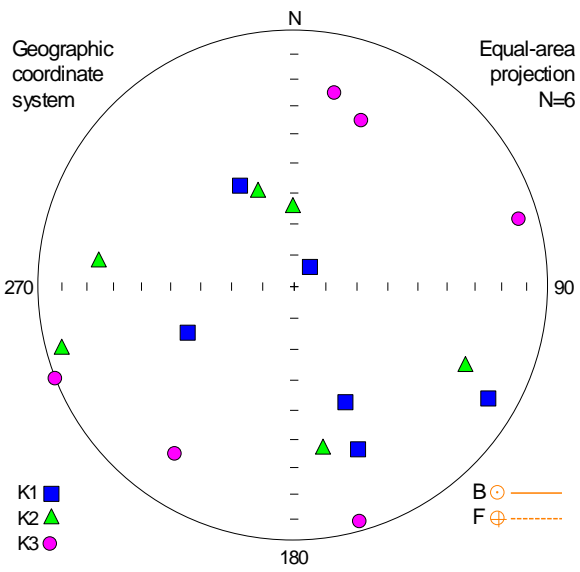


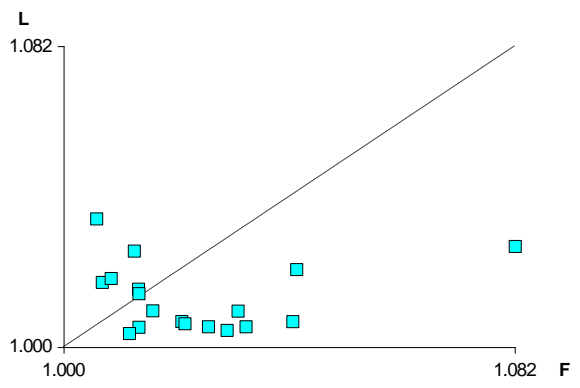
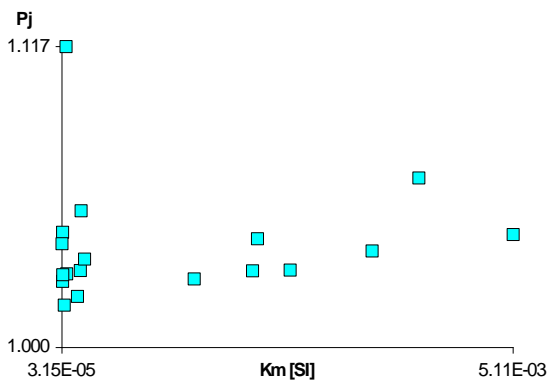
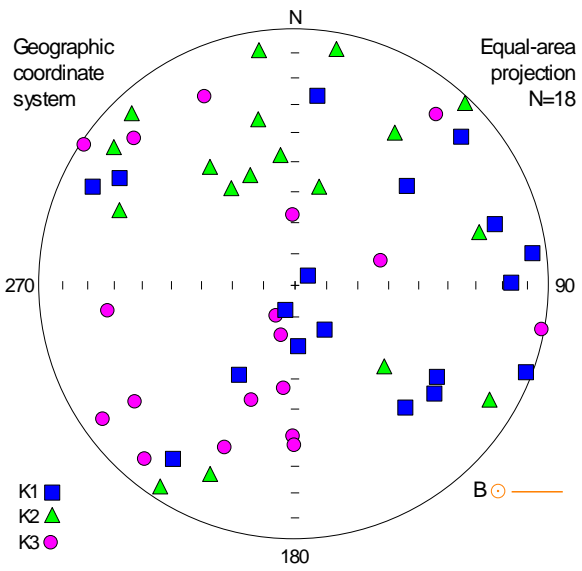


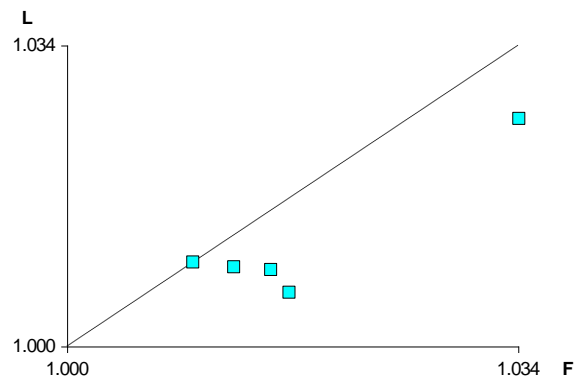
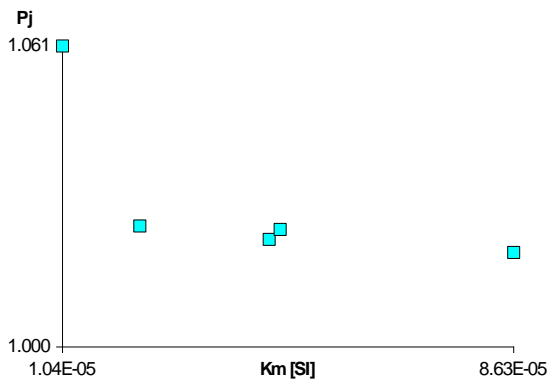
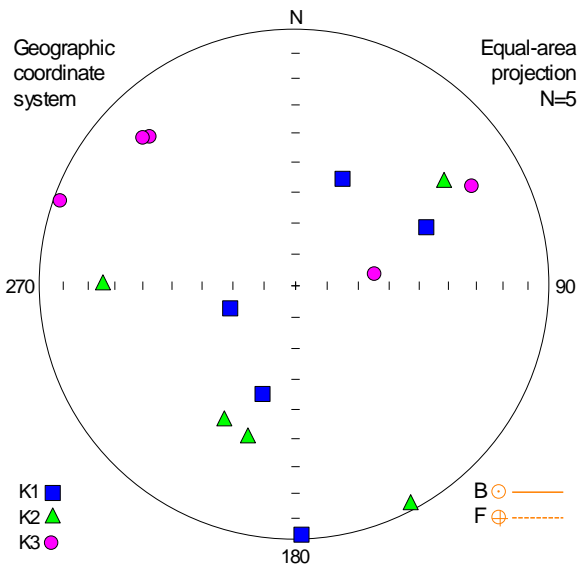


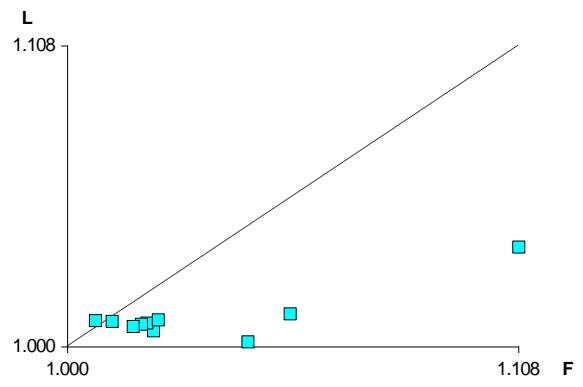
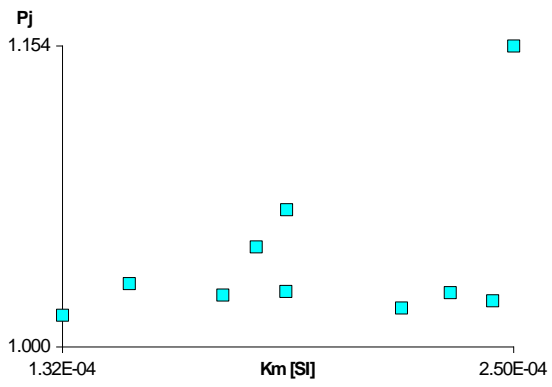
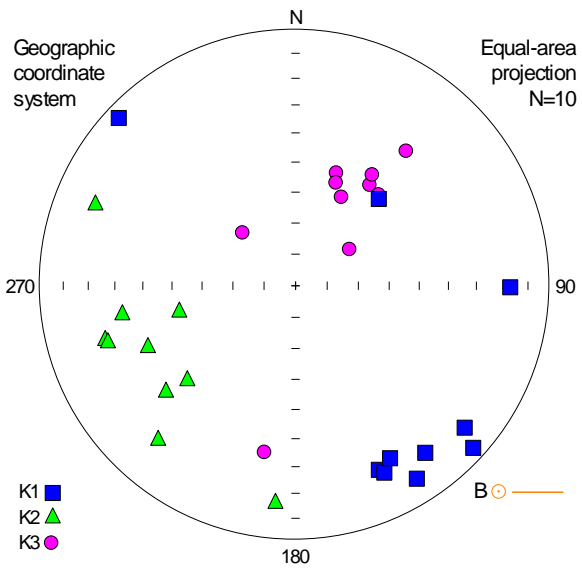


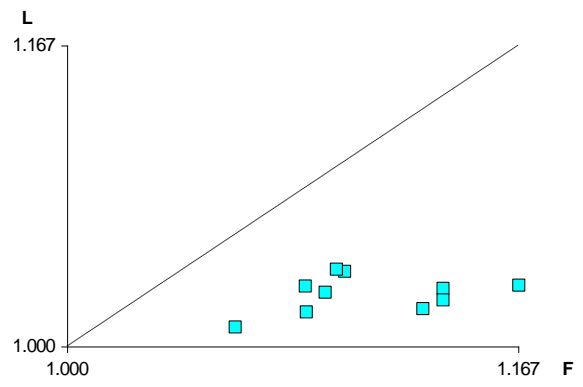
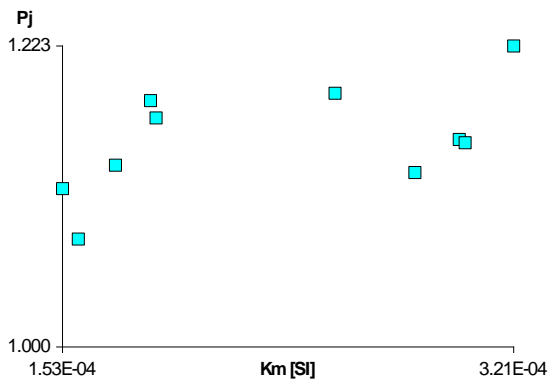
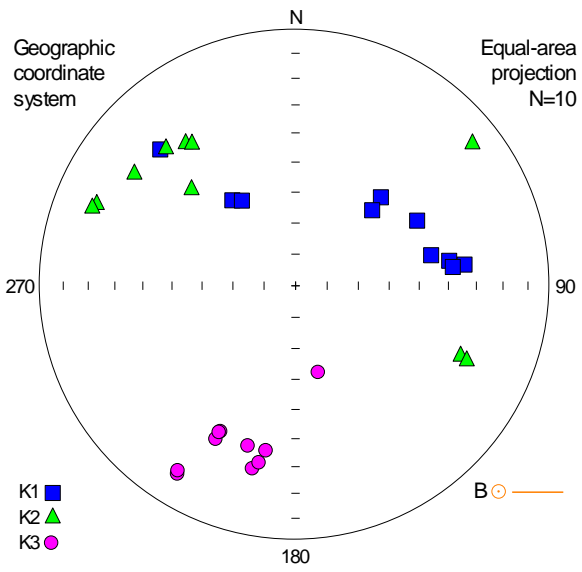




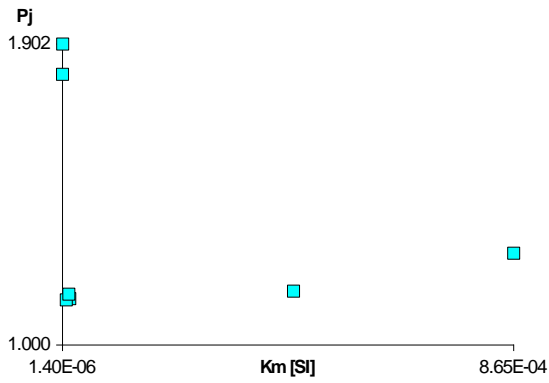
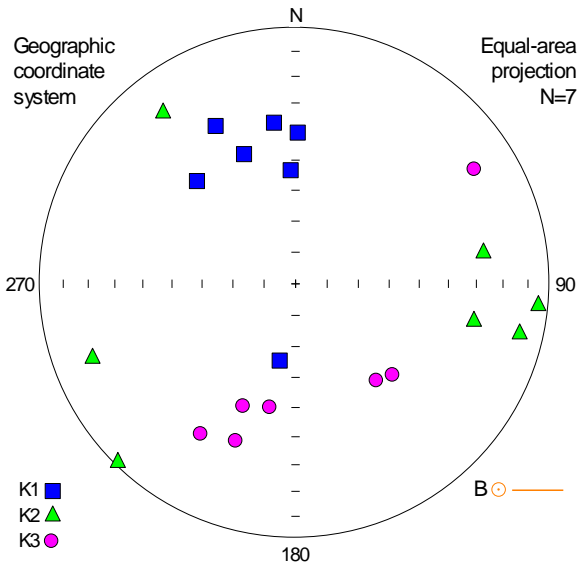












## 8.5 IRM

### OG2 & OG3

core	end-member 1	end-member 2
OG2.1	0	1
OG2.6	0.135921062	0.864078938
OG2.10	0.183092498	0.816907502
OG2.11	0.177046421	0.822953579
OG2.14	0.148804283	0.851195717
OG2.18	0.451921031	0.548078969
OG2.22	0.45079673	0.54920327
OG3.5	0.636458357	0.363541643
OG3.7	0.628870085	0.371129915

table 6: End-member contributions for OG2 & OG3.

Contributions of OG2 are predominantly towards the second end-member. The last cores of OG2 and OG3 contribute more towards the first end-member.

## OG4

core	end-member 1	end-member 2
OG4.1	0.655722814	0.344277186
OG4.2	0.63923499	0.36076501
OG4.5	0.736892786	0.263107214
OG4.6	0.725281963	0.274718037
OG4.7	0.688801374	0.311198626
OG4.8	0.729171814	0.270828186
OG4.9	0.669422572	0.330577428
OG4.10	0.58751003	0.41248997
OG4.13	0.652303007	0.347696993
OG4.14	0.647000857	0.352999143
OG4.15	0.640797075	0.359202925
OG4.17	0.599568161	0.400431839
OG4.18	0.457004229	0.542995771
OG4.19	0.569596126	0.430403874
OG4.20	0.424232221	0.575767779
OG4.21	0.55076111	0.44923889
OG4.23	0.574550296	0.425449704
OG4.24	0.642887339	0.357112661

table 7: End-member contributions for OG4.

OG4 has a greater contribution towards the first end-member contributes; 40%-75% towards the first end-member but significant contribution towards the second end-member is present in all cores. The cores that have been drilled first have a slightly higher contribution towards the first end-member than the later cores but the difference is inconsequential.

## OG5, OG6, OG7 & OG8

core	end-member 1	end-member 2
OG5.4	0.712703939	0.287296061
OG6.2	0	1
OG6.4	0	1
OG7.1J2	1	0
OG7.2A2	0.973793674	0.026206326
OG7.3A5	1	0
OG7.3B2	0.702818088	0.297181912
OG8.2	0.724235029	0.275764971

table 8: End-member contributions for OG5, OG6, OG7 and OG8.

Only one core of OG5 and OG8 has been analyzed but they both show major contributions towards the first end-member and smaller yet not necessarily insignificant contributions towards the other end-member. OG6, on the other hand, is exclusively made up of the second end-member. OG7, like OG5 and OG8, predominantly contributes towards the first end-member, with cores OG7.1J2 and OG7.3A5 exclusively so.

## OG9, OG10 & OG11

core	end-member 1	end-member 2
OG9.7	0.445310616	0.554689384
OG9.8	0.723577479	0.276422521
OG9.9	0.464444762	0.535555238
OG9.10	0.382051028	0.617948972
OG9.12	0.719193586	0.280806414
OG9.13	0.759472116	0.240527884
OG10.1	0	1
OG10.4	0.423907756	0.576092244
OG11.2	0.61561945	0.38438055

table 9: End-member contributions for OG9, OG10 and OG11.

OG9 has varying contributions towards the end-members, with OG9.7, OG9.9 and OG9.10 preferring the second end-member. OG9.8, OG12 and OG13 contribute more to the first end-member, with a greater shift from equality for these cores when compared with the other aforementioned cores. OG10.1 exclusively contributes towards the second end-member, and, to a lesser extent, so does OG10.4. OG11 only has one core and primarily contributes towards the first endmember.

### OG12 & OG13

core	end-member 1	end-member 2
OG12.16	0	1
OG12.17	0.020833257	0.979166743
OG12.18	0.405448528	0.594551472
OG12.19	0.230607503	0.769392497
OG12.21	0.140003572	0.859996428
OG13.3	0.725605712	0.274394288
OG13.4	0.721488021	0.278511979
OG13.6	0.681105387	0.318894613
OG13.7	0.9350227	0.0649773
OG13.8	0.803436509	0.196563491
OG13.9	0.852062145	0.147937855
OG13.12	0.926957484	0.073042516
OG13.14	0.860322288	0.139677712

Table 10: End-member contributions for OG12 & OG13.

All the cores from OG12 are taken from the limestones. Its primary contribution is towards the second end-member with only OG12.18 seeing a more evenly distributed contribution. The situation is reversed for OG13, with up to 95% of its contribution towards the first end-member.

### OG14 & OG15

core	end-member 1	end-member 2
OG14.2	0.827577787	0.172422213
OG14.4	0.760110282	0.239889718
OG14.8	0.479255869	0.520744131
OG14.13	0.302890883	0.697109117

<b>OG15.2</b>	0.729755202	0.270244798
<b>OG15.3</b>	0.772517214	0.227482786
<b>OG15.5</b>	0.821907989	0.178092011
<b>OG15.6</b>	0.691189098	0.308810902
<b>OG15.7</b>	0.517161022	0.482838978
<b>OG15.10</b>	0.569648305	0.430351695
<b>OG15.11</b>	0.713196634	0.286803366

**table 11: End-member contributions for OG14 & OG15.**

The contributions of OG14 are split, with OG14.2 and OG14.4 on the one hand and OG14.8 and OG14.14 on the other hand contributing more towards the first and second end-member, respectively. OG15's contributions are primarily towards the first end-member.

### **OG16 & OG17**

<b>core</b>	<b>end-member 1</b>	<b>end-member 2</b>
<b>OG16.5</b>	0.06387805	0.93612195
<b>OG16.7</b>	0.093816147	0.906183853
<b>OG16.9</b>	0.234874438	0.765125562
<b>OG16.10</b>	0.515872004	0.484127996
<b>OG17.3</b>	0.546965246	0.453034754
<b>OG17.5</b>	0.238344882	0.761655118
<b>OG17.7</b>	0.331241051	0.668758949
<b>OG17.9</b>	0.411875663	0.588124337

**table 12: End-member contributions for OG16 & OG17.**

The four cores of OG16 contribute heavily towards the second end-member with OG16.10 having a more equally distributed contribution. For OG17, OG17.5, OG17.7 and OG17.9 have a greater contribution towards the second end-member whereas OG17.3 is more evenly distributed.

### **OG18 & OG19**

<b>core</b>	<b>end-member 1</b>	<b>end-member 2</b>
<b>OG18.1</b>	1	0
<b>OG18.3</b>	0.037058799	0.962941201
<b>OG18.5</b>	0	1
<b>OG18.6</b>	0.317441512	0.682558488
<b>OG18.7</b>	0.656658962	0.343341038
<b>OG19.2</b>	0.341242708	0.658757292
<b>OG19.3</b>	0.232413983	0.767586017
<b>OG19.5</b>	0.054565175	0.945434825
<b>OG19.6</b>	0.401255042	0.598744958
<b>OG19.12</b>	0.175588258	0.824411742
<b>OG19.14</b>	0.406416498	0.593583502
<b>OG19.19</b>	1	0

**table 13: End-member contributions for OG18 & OG19.**

OG18.1 and OG18.5 are oddities because of the fact that they fully contribute towards the first and second end-member, respectively. OG18.3 also almost exclusively contributes towards the second end-member. The other cores of OG18 and OG19, apart from OG19.19, are a mixture of end-members. OG19.19, on the other hand, fully contributes towards the first end-member.

## 8.7 miscellaneous

site	# of cores	strike/dip S <sub>0</sub>	strike/dip S <sub>1</sub>	latitude	longitude
OG1	8	N/A	N/A	42°44'0.2"	0°14'41.0"
OG2	22	A = 166/29 B = 29/67 C = 103/82	N/A N/A N/A	42°44'10"	0°15'30"
OG3	8	109/66	N/A	42°43'29.7"	0°17'20.4"
OG4	24	A = 269/36 B = 282/24 C = 204/22	A = 290/66 N/A N/A	42°49'33.4"	0°16'58.8"
OG5	10	A = 320/19 B = 273/19	N/A N/A	44°42'8.4"	0°7'12.8"
OG6	10	248/62	246/78	42°42'23.0"	0°7'28.7"
OG7	N/A	306/42	N/A	42°46'37.5"	0°11'51.3"
OG8	N/A	280/36	305/55	42°46'33.2"	0°11'54.9"
OG9	13	89/13	N/A	42°34'2.34"	0°27'2.007"
OG10	10	287/31	N/A	42°34'56.6"	0°28'28.1"
OG11	17	A = 186/79 B = 243/55 C = 328/48	A,B,C = 300/38	42°31'19.8"	0°39'8.8"
OG12	24	310/39	N/A	42°31'0.1'	0°39'3.6"
OG13	14	A = 31/83 B = 212/32	A,B = 289/60	42°30'10.2"	0°39'8.2"
OG14	13	A = 178/77 B = 277/58	A,B = 293/37	42°28'30.8"	0°46'38.4"
OG15	11	144/48	N/A	42°20'68"	1°04'7.8"
OG16	12	286/51	N/A	42°32'2.1"	1°10'31.8"
OG17	9	287/50	N/A	42°30'17.4"	1°10'31.8"
OG18	10	269/51	244/67	42°34'8.0"	1°35'27.8"
OG19	15	260/60	N/A	42°34'5.4"	1°35'7.8"

table 14: Table of the bedding and foliation measurements, where applicable. The geographic coordinates are also included.